Study of light harvesting materials for next generation solar cells

次世代太陽電池の光吸収材料に関する研究

Graduate School of Life Science and System Engineering

Kyushu Institute of Technology

Dissertation for the Degree of Doctor of Philosophy

WANG ZHEN

Supervisor
Professor. Shuzi Hayase

Abstract

Lead-based optoelectronic materials including PbS and Pb-halide perovskite have been attracted tremendous attention recently. PbS Quantum dots（QDs）are promising semiconducting materials for photovoltaics due to their band gap tunability and excellent charge transport properties. Long insulating organic ligands results in weak inter-particle interaction with poor charge transfer. Therefore, we exploited sulfur-crosslinking of PbS QDs to achieve desirable mobility with higher efficiency of solar cells. In addition, lead-based perovskites have recently obtained high power conversion efficiencies of over 23%, which makes perovskite as a potential candidate for highly efficient and easily processable perovskite devices. However, the large number of traps residing in bulk perovskite and at the interface are unavoidable in polycrystalline films, resulting in nonradiative charge recombination, which will influence power conversion efficiency and intrinsic stability applied in heterojunction photovoltaic device. In this thesis, the goal is optimize the interface in device and the polycrystalline perovskite films for better crystalline of perovskite and efficient reduction of trap densities. As a result, the enhanced performance with superior stability was achieved in humid air.

In chapter 1, the background of photovoltaics and their power conversion efficiency are introduced, basic fundamentals of Pb-based light absorbing materials has been presented. In chapter 2, we present a new method for increased QDs mobility and performance of QDs solar cells. In chapter 3, a new sulfur interfacial functionalization is developed, improvement of efficiency and stability is achieved upon interface engineering. In chapter 4, we describes suqaraines passivation on Pb-halide perovskite grain boundaries, contributing to the higher efficiency and stability in humid air. In chapter 5, sulfur-doped all-inorganic perovskite devices are fabricated in ambient atmosphere, leading to superior phase stability and higher efficiency.

Finally, general conclusion and future prospects are presented for the Pb-based photovoltaic materials in solar cells application. The architecture, encapsulation of Pb-based solar cells need further study to be applied in commercialization in the future.

Contents

Chapter 1. General introduction

1.1 Solar energy

Energy is the fundamentals for human lives, fossil fuels including natural gas, petroleum and coal have great influence on human beings since the first industrial revolution, contributing to the development of human civilization and progress of science and technology. However, the environment pollution from the utilization of petroleum and coal further negatively affect our lives, large amount of CO_2, NO_x were emitted, resulting in serious climate and global warming.[1-2] Furthermore, known energy sources on earth have been consumed substantially since the first industrial revolution due to the lavish usage from humans. As a result, it is highly urgent to find new energy sources, natural gas is one of energy sources, which have better application prospects own to its advantage of non-pollution. But gas in earth is limited and not renewable.

Therefore, we need find a new energy sources to cope with changing circumstances and the escalating demand for energy. Solar energy is inexhaustible and renewable energy resources for human beings, which is much more abundant than others in earth. This highly diffused source is the great potential to satisfy the demands of development of human civilization. The solar energy intercepted by the earth has vastly exceed all stored energy on earth and anticipated energy demands from human beings (Figure 1.1).

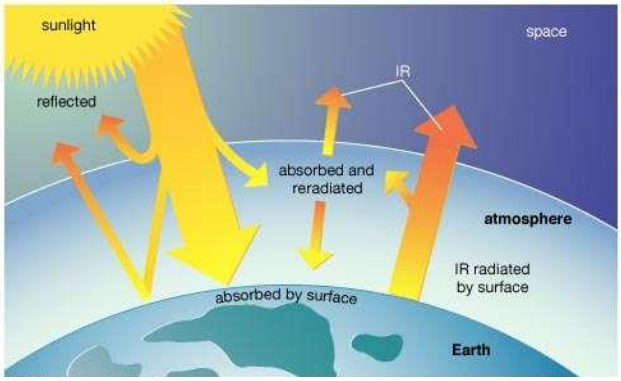

Figure 1.1. Absorption of solar energy on earth.

1.2 Photovoltaic technologies

How to convert the solar energy into purest form of energy including electricity directly and efficiently becomes a new challenge. Photovoltaic technologies have become the most effective way to harness the solar power, which can direct convert sunlight into electricity for human's daily life and factories. They have an advantage of environmental-friendly without gas emission and any heat engine to interfere. However, the limitation of low energy density from solar illumination (the standard irradiance AM1.5G=1kw/m^2) motivate us to construct more efficient photovoltaic power generation system with low cost. [3] Light absorbing materials are the core in power generation system although multiple components should be considered including electrical connections and cost of the power conversion system. [4] Figure 1.2 describes the mechanism of light absorbing materials in devices operation process. Once sunlight is illuminated on the surface of solar cells, photo energy was absorbed and the electron-hole pairs are generated inside semiconductor materials. Large area of P-N junction consists of the solar cell, a barrier for the majority carries transfer between P-type and N-type semiconductor was formed owing to the asymmetric doping, finally forming a depletion region when the electrostatic forces are exactly balanced. When electrons in p-doped region diffuse into the depletion region, the lowered potential

energy barrier at the junction is formed, resulting in the flowed current and established bias at the external terminals. Holes from the n-doped region diffuse in the opposite direction towards the p-doped side. Finally, movement of charges in absorbing semiconductors leads to the production of current. [5]

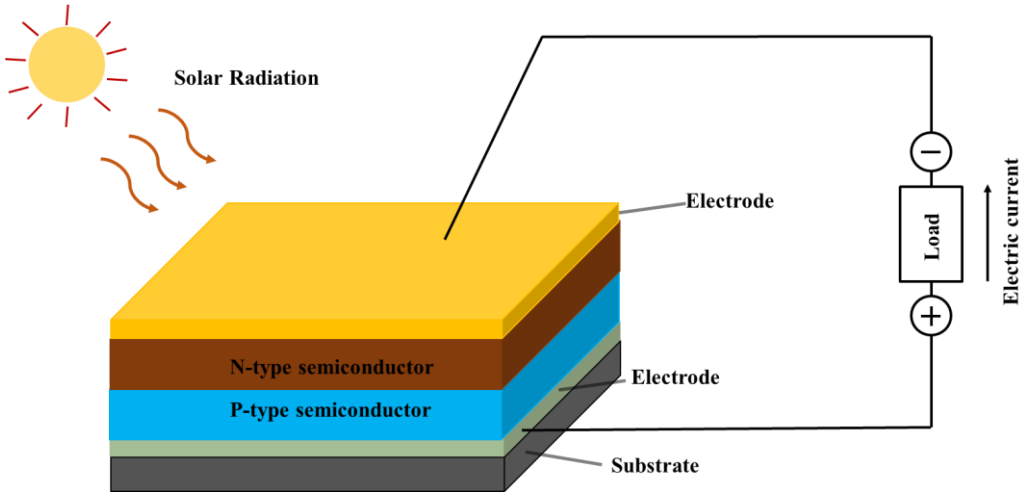

Figure 1.2. Mechanism of solar photovoltaic operation.

In 1877, Adams fabricated the first light absorber of selenium materials,[6] and 1% power conversion efficiency was obtained using the selenium semiconductor. Since them, solar photovoltaic technology is classified based on the cost, commercially availability and achieved efficiency. Silicon cells as the first generation of solar cells have achieved more than 20% efficiency, but the high price of single crystalline silicon or multi-crystalline silicon can not applied in large scale. [7-9] The second generation solar cells are the thein-film solar cells with lower cost and higher efficiency due to the low-temperature fabrication techniques. This is suitable for large-scale application in commercialization.[10] The third generation solar cells contains dye-sensitized, organic, quantum dots and perovskite solar cells, which aim at continuing to lower the production costs with high power conversion efficiency.[11-12]

1.3 Semiconductor nanocrystals

Semiconductor nanocrystals (NCs) are specifically colloidal quantum dots (QDs) are promising materials for photovoltaics and light emitting diodes due to their band gap tunability, high photo-stability, and excellent charge transport properties and low cost fabrication process.[13-14] The exploitation of these superior properties requires the knowledge of nanocrystal surface chemistry as this determines the size and morphology of the resultant NCs and hence the overall optoelectronic properties.[15] The band gap dependence on the particle size induced by quantum confinement strongly affect the QDs in various application.

The synthesized NCs have applied in light-emitting devices,[16-17] biological imaging[18] and photovoltaics[19] through changing the NCs size during the synthesis. A high temperature synthesis method is mandatory in NCs synthesis, and finally stabilize NCs using ligands on surface for the monodispersity in organic solvent. Ligands could interact with elements on surface of NCs, providing sufficient repulsive force for steric nature and preventing from the uncontrolled aggregation of the monomers, meanwhile, ligands can regulate the NCs growth thermodynamics. Furthermore, ligands act as passivator to coordinate and passivate the surface atoms for decreased trap densities. As a result, different NCs have different ligands for passivation, because a polar headgroup of ligands (for example, thiol, amine and carboxylic) can provide a strong affinity to NCs and effectively coordinate with surface atoms.[20-21]

Colloidal quantum dots (CQDs) semiconductor materials have attracted tremendous interests in academic and industry. Excellent physics and chemistry properties including higher carrier mobility and strongly suppressed recombination result in rapid development of CQDs in solar cell application.[22] The approaches for CQD solar cells fabrication in labs are solid-state ligand exchange process by spin-coating process currently, but it suffers from low efficiency of CQDs

materials usage, as a result, CQDs inks were developed for the deposition of QDs film aiming at the desired thickness of light absorber layer.[23] The efficiency of PbS QDs solar cells has boosted up to 10% through ligands optimization. Researchers will continue to develop and optimize electrical properties of QDs and reduce trap recombination, leading to the increased performance of QDs solar cells (Figure 1.3).

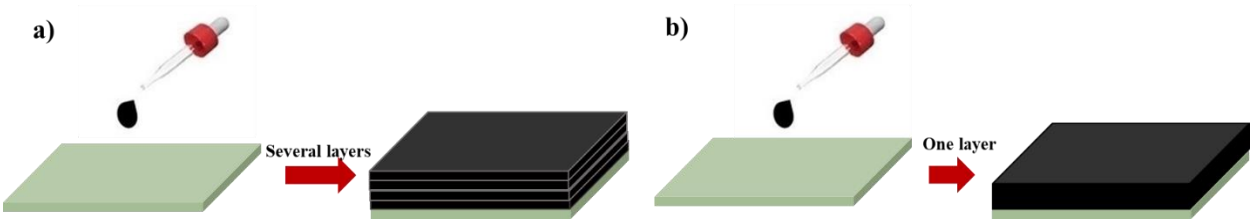

Figure 1.3. Schematic of a) the layer-by-layer spin-coating process for desired thickness and b) one single drop casting process.

1.4 Organmetal halide perovskite materials and solar cells

1.4.1 Perovskite materials

Lead-halide perovskite devices have been considered as a potential photovoltaics owing to the high power conversion efficiencies and simple, low-cost fabrictaion techniques. [24-25] in 2009, Miyasaka *etal* first reported $CH_3NH_3PbX_3$ as a semiconductor sensitizer in DSSC solar cells, [26] which obtained more 3% efficiency. Little attention has been focused until long-term stability perovskite with exceeding 9% efficiency was achieved in 2012.[27] Since then perovskites experienced a very fast development with more than 20% efficiency.[28-29] besides, high quality perovskite accompanying enhanced long-term stability was achieved.

Perovskite materials commonly consists of a group number of compounds whose general formula is ABX_3 structure. As shown in Figure 1.4, in lead-based perovskite lattice, B-site is the lead, and A sites can be occupied by K^+, Rb^+, Cs^+, $CH_3NH_3^+$ (MA^+) and $CH_2CH{=}NH_2^+$ (FA^+), X-site elements usually are halide (Br^-, I^-). In general, perovskite lattice shows the cubic structure

based on its following geometric tolerance factor (t) in order to keep the corner-sharing structure.

$$t = \frac{r_A + r_x}{\sqrt{2}(r_B + r_x)}$$

Where r_X , r_A and r_B denote the effective ionic radius of X, A and B ions respectively. Ideally, cubic perovskite lattice is highly expected when the t is in the range of 0.75 to 1. If the t is smaller than 0.75, implying the ions are too small to hold the PbX_6 octahedron. If the t value exhibits larger than 1, the cubic structure is distorted and then collapsed. Additionally, the octahedral factor μ, $\mu=r_B/r_X$, which is an empirical parameter to evaluate the formation of PbX_6 octahedron. A μ value ranging from 0.4 to 0.9 can stabilize PbX_6 octahedra.

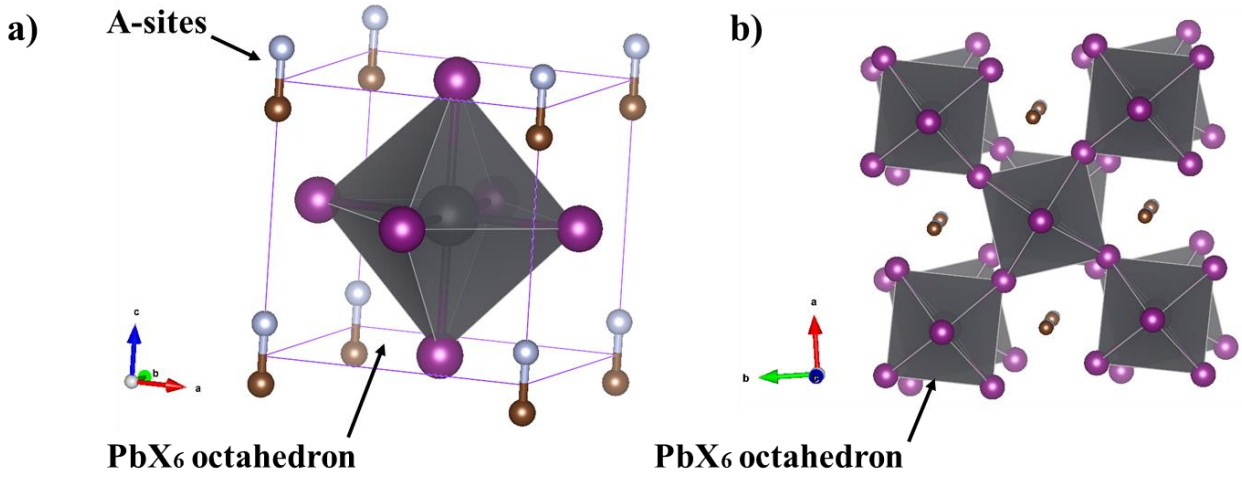

Figure 1.4. Schematic illustration of lead-halide perovskite structure along a and c axes direction respectively.

1.4.2 Optelectric properties of perovskites

For the Pb-based perovskite as light absorbing materials, the absorption coefficient of $MAPbI_3$ was estimated to be 1.5×10^4 cm^{-1} at about 550 nm, this is comparable to previous light absorbing materials such as CIGS or CdTe.[30] Besides, Pb-halide perovskites show the balanced hole and electron-transporting behavior. For example, the electron and hole diffusion length of

$MAPbI_xCl_{1-x}$ was estimated to be 1069 nm and 1213 nm respectively, suggesting that perovskite materials exhibit low exactions energy induced by light illumination. This demonstrates that perovskite possess high density of states and high open-circuit voltage with low traps compared with the conventional silicon or organic light absorbing materials. The bandgap of perovskites is significantly of importance for absorbing light in rang wavelength of sunlight, influencing the application of perovskite solar cells. Replacing the A-sites with other organic cation or X sites with other halides can significantly tune the bandgap of perovskites. Almost all Pb-halides perovskites were reported with the bandgap ranging from 1.5 eV to 2.2 eV, which is generally desirable for the application of perovskite solar cells.

Table 1.1. Theoretical bandgaps and Experimental bandgaps of perovskite materials.[31-34]

Perovskites	Theoretical bandgap/eV	Experimental bandgap/eV
$CH_3NH_3PbI_3$	1.5-1.61	1.55-1.61
$CH_3NH_3PbBr_3$	2.3	2.32
$CH_3NH_3PbI_{3-x}Cl_x$	-	1.55-1.64
$HC(NH_2)_2PbI_3$	1.48	1.47
α-$CsPbI_3$	1.52	1.73

1.4.3 Preparation of perovskite polycrystalline

The low perfromance of perovskite solar cells arise from inferior quality of perovskite films with much larger trap densities along the grain boundaries and the lack of excellent preparation method of perovskite devices at the early stage of perovskite development. For Pb-halide perovskites, perovskite single crystals can be prepared by a solution method. One-step and

two-step low-temperature solution-processing approaches are the two main methods for preparation of perovskite films. Kim *et al* first developed the one-step process for polycrystalline perovskite films in 2012, [27] as shown in Figure 1.5 a. First, wet and compact PbI_2 film is prepared by 70°C treatment, then drop of MAI solution on the PbI_2 film immediately lead to color change from pale yellow to dark red, implying the fast conversion to perovskite lattice, and then finally become dark after thermal annealing. in 2014, Nam-Gyu Park *et al* reported a two-step method to prepare perovskite polycrystalline films by spin-coating as shown in Figure 1.5 b.[35] The MAI and PbI_2 mixture in polar solvent was dropped on substrate and the anti-solvent (e.g. toluene, ethyl acetate) is dropped on the spin-coating wet perovskite film. The dark-brown perovskite is obtained upon thermal annealing. In order to achieve polycrystalline morphology with lower trap densities, various approaches are applied to optimize the process to obtain excellent better crystalline,[36-40] which mainly originate from the suppressed trap-assisted recombination and decreased trap densities.

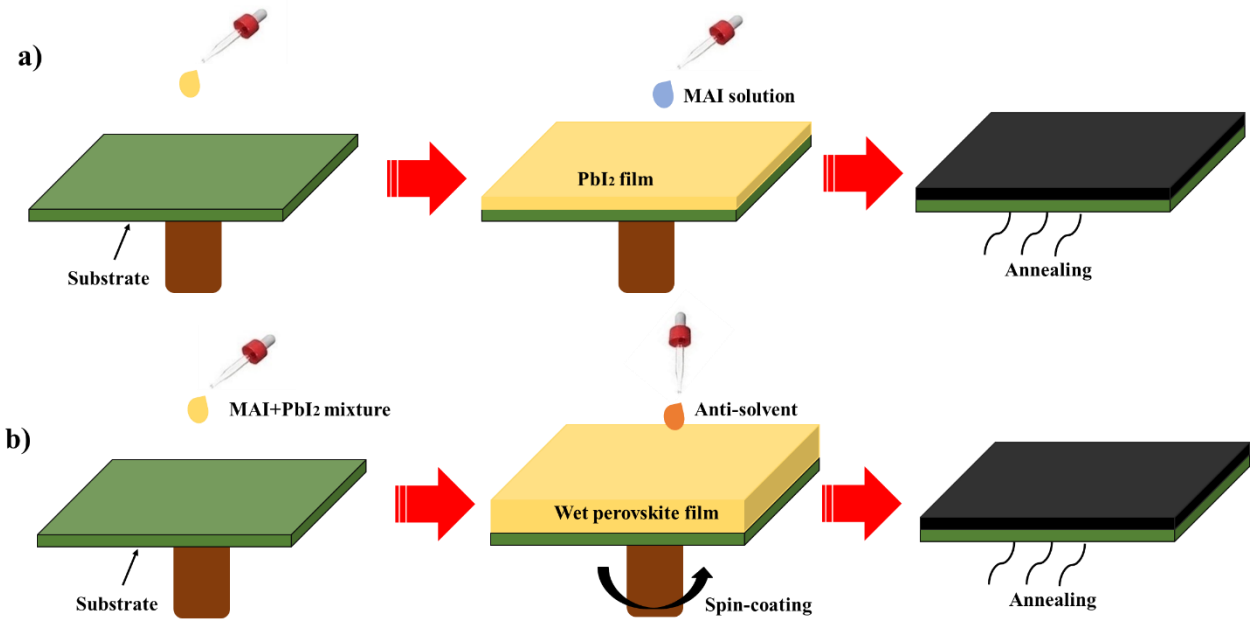

Figure 1.5. Typical procedures for two main process for the polycrystalline perovskite film.

1.4.4 Perovskite device structures and working principle

Based on the excellent properties of Pb-halide perovskite discussed above, two typical architectures are introduced and constructed: Mesoscopic nanostructure and planar structure (Figure 1.6). In general, TiO_2 mesoscopic structure is used as electron transport layer (ETL) with mesoscopic nanostructure. In this case, charge transport or transfer into TiO_2 ETL has two paths as shown in Figure 1.6 a. comparatively, the carrier transfer in planar structure has only one path. Studies demonstrated that the former structure shows relatively low efficiency than the latter. The charge transport in two different structures exhibited similar results but the former shows higher trap-assisted recombination at the interface between perovskite layer and TiO_2 probably due to the larger area of interface between perovskite and TiO_2.[41] Spiro-MeOTAD is usually applied as the hole transport layer (HTL) to achieve high performance because of its high mobility.

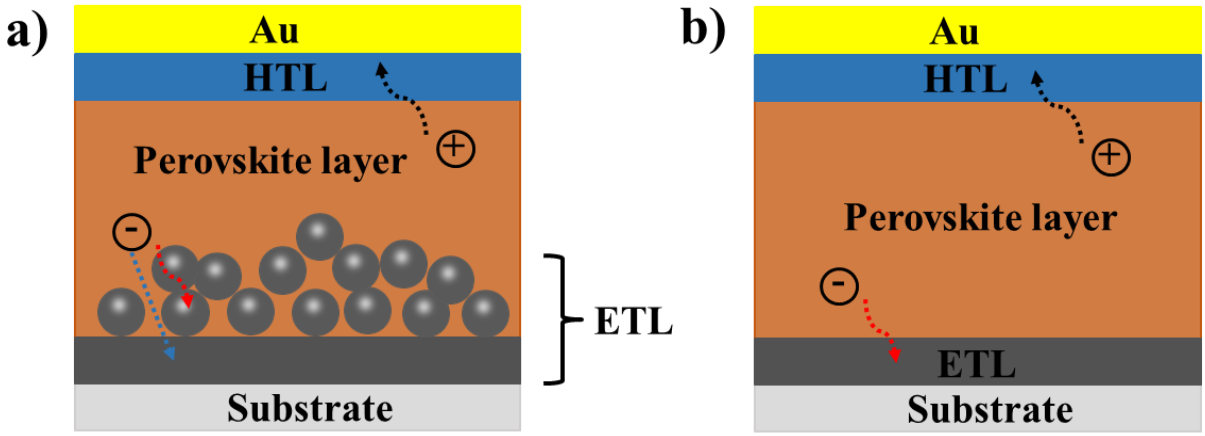

Figure 1.6. Perovskite Solar cells with a) mesoporous electron transport layer (ETL) and b) planar structure. HTL represents the hole transport layer.

Besides, the valence and conduction band should be aligned well with the ETL and HTL in order to realize the efficient carriers transfer. Additionally, the device open-circuit voltage is related with the conduction band of ETL and valence band of HTL. We can not obtain the theoretical value of voltage directly through the difference between the conduction band of ETL

and valence band of HTL.

1.5 Motivation and objectives of this work

Pb-based photovoltaics exhibit excellent optelectric properties in the application of solar cells. However, the performance of perovskite solar cells leave much room for improvement. On one hand, the Pb-based QDs show low carrier mobility own to the existence of long insulating organic molecules. Furthermore, the stability of perovskite devices needed to be solved due to the easier degradation in operation atmosphere (room temperature or relative high humidity). Typically the perovskite absorbing layer degrades along the grain or the interface between perovskite and charge selective layer, which can be ascribed to the large trap densities at the grain boundary or interface.

In this thesis, Firstly, for the QDs solar cells, we try to explore the ligand exchange by atomic coordination on QDs surface, aiming at increased the charge mobility and charge transport in QDs. Secondly, we focus on the research on passivation of grain boundary and interface to suppress the trap-assisted recombination, meanwhile, the passivation on perovskite is expected to prevent the moisture invasion. Thirdly, the all-inorganic perovskites exhibit more sensitive to the moisture in ambient atmosphere. All-inorganic cubic perovskite structure is explored to enhance the phase stability.

Reference

[1] G. Tiao, G. Box, W. Hamming, *Journal of the Air Pollution Control Association* **1975**, 25, 260.

[2] A. Brown, S. Müller, Z. Dobrotkova, *IEA information paper* **2011**.

[3] S. Rehman, M. A. Bader, S. A. Al-Moallem, *Renewable and sustainable energy reviews* **2007**, 11, 1843.

[4] A. Al-Hasan, A. Ghoneim, A. Abdullah, *Energy conversion and management* **2004**, 45, 483.

[5] N. Amin, S. A. Shahahmadi, P. Chelvanathan, K. S. Rahman, M. I. Hossain, M. Akhtaruzzaman, in *Encyclopedia of Sustainable Technologies*, Elsevier **2017**, p. 11.

[6] W. G. Adams, R. E. Day, *Proceedings of the Royal Society of London* **1877**, 25, 113.

[7] B. van der Zwaan, A. Rabl, *Solar energy* **2003**, 74, 19.

[8] W. M. Keogh, A. W. Blakers, *Progress in Photovoltaics: Research and Applications* **2004**, 12, 1.

[9] J. I. Hanoka, *Solar energy materials and solar cells* **2001**, 65, 231.

[10] C. S. Ferekides, D. Marinskiy, V. Viswanathan, B. Tetali, V. Palekis, P. Selvaraj, D. Morel, *Thin Solid Films* **2000**, 361, 520.

[11] M. Itoh, H. Takahashi, T. Fujii, H. Takakura, Y. Hamakawa, Y. Matsumoto, *Solar energy materials and solar cells* **2001**, 67, 435.

[12] D. C. Olson, J. Piris, R. T. Collins, S. E. Shaheen, D. S. Ginley, *Thin solid films* **2006**, 496, 26.

[13] J. An, X. Yang, W. Wang, J. Li, H. Wang, Z. Yu, C. Gong, X. Wang, L. Sun, *Solar Energy* **2017**, 158, 28.

[14] K. O. Aruda, M. Bohlmann Kunz, M. Tagliazucchi, E. A. Weiss, *The journal of physical chemistry letters* **2015**, 6, 2841.

[15] S. Z. Bisri, C. Piliego, M. Yarema, W. Heiss, M. A. Loi, *Advanced Materials* **2013**, 25, 4309.

[16] V. Colvin, M. Schlamp, A. P. Alivisatos, *Nature* **1994**, 370, 354.

[17] N. Tessler, V. Medvedev, M. Kazes, S. Kan, U. Banin, *Science* **2002**, 295, 1506.

[18] T. Pellegrino, S. Kudera, T. Liedl, A. Muñoz Javier, L. Manna, W. J. Parak, *small* **2005**, 1, 48.

[19] G. Konstantatos, I. Howard, A. Fischer, S. Hoogland, J. Clifford, E. Klem, L. Levina, E. H. Sargent, *Nature* **2006**, 442, 180.

[20] W.-S. Song, H.-S. Lee, J. C. Lee, D. S. Jang, Y. Choi, M. Choi, H. Yang, *Journal of nanoparticle research* **2013**, 15, 1750.

[21] M. R. Buck, I. T. Sines, R. E. Schaak, *Chemistry of Materials* **2010**, 22, 3236.

[22] M. L. Brongersma, Y. Cui, S. Fan, *Nature materials* **2014**, 13, 451.

[23] A. Fischer, L. Rollny, J. Pan, G. H. Carey, S. M. Thon, S. Hoogland, O. Voznyy, D.

Zhitomirsky, J. Y. Kim, O. M. Bakr, *Advanced Materials* **2013**, 25, 5742.

[24] Z. Wei, H. Chen, K. Yan, S. Yang, *Angewandte Chemie International Edition* **2014**, 53, 13239.

[25] P. K. Nayak, D. Cahen, *Advanced Materials* **2014**, 26, 1622.

[26] A. Kojima, K. Teshima, Y. Shirai, T. Miyasaka, *Journal of the American Chemical Society* **2009**, 131, 6050.

[27] H.-S. Kim, C.-R. Lee, J.-H. Im, K.-B. Lee, T. Moehl, A. Marchioro, S.-J. Moon, R. Humphry-Baker, J.-H. Yum, J. E. Moser, *Scientific reports* **2012**, 2, 591.

[28] M. Liu, M. B. Johnston, H. J. Snaith, *Nature* **2013**, 501, 395.

[29] D. Liu, T. L. Kelly, *Nature photonics* **2014**, 8, 133.

[30] S. De Wolf, J. Holovsky, S.-J. Moon, P. Löper, B. Niesen, M. Ledinsky, F.-J. Haug, J.-H. Yum, C. Ballif, *The journal of physical chemistry letters* **2014**, 5, 1035.

[31] W.-J. Yin, J.-H. Yang, J. Kang, Y. Yan, S.-H. Wei, *Journal of Materials Chemistry A* **2015**, 3, 8926.

[32] W. J. Yin, T. Shi, Y. Yan, *Advanced Materials* **2014**, 26, 4653.

[33] K. R. Kendall, C. Navas, J. K. Thomas, H.-C. zur Loye, *Chemistry of materials* **1996**, 8, 642.

[34] H. Tsai, W. Nie, J.-C. Blancon, C. C. Stoumpos, R. Asadpour, B. Harutyunyan, A. J. Neukirch, R. Verduzco, J. J. Crochet, S. Tretiak, *Nature* **2016**, 536, 312.

[35] J.-H. Im, I.-H. Jang, N. Pellet, M. Grätzel, N.-G. Park, *Nature nanotechnology* **2014**, 9, 927.

[36] Y. H. Lee, J. Luo, R. Humphry-Baker, P. Gao, M. Grätzel, M. K. Nazeeruddin, *Advanced Functional Materials* **2015**, 25, 3925.

[37] A. R. Pascoe, S. Meyer, W. Huang, W. Li, I. Benesperi, N. W. Duffy, L. Spiccia, U. Bach, Y. B. Cheng, *Advanced Functional Materials* **2016**, 26, 1278.

[38] J. Gong, M. Yang, D. Rebollar, J. Rucinski, Z. Liveris, K. Zhu, T. Xu, *Advanced Materials* **2018**, 1800973.

[39] A. Pradhan, T. Morimoto, M. Saikiran, G. Kapil, S. Hayase, S. S. Pandey, *Journal of Materials Chemistry A* **2017**, 5, 22672.

[40] S. Sun, T. Salim, N. Mathews, M. Duchamp, C. Boothroyd, G. Xing, T. C. Sum, Y. M. Lam, *Energy & Environmental Science* **2014**, 7, 399.

[41] V. Gonzalez-Pedro, E. J. Juarez-Perez, W.-S. Arsyad, E. M. Barea, F. Fabregat-Santiago, I. Mora-Sero, J. Bisquert, *Nano letters* **2014**, 14, 888.

Chapter 2. Investigation of charge transport in quantum dots and photovoltaic performance in ambient atmosphere

2.1 Introduction

Semiconductor quantum dots (QDs) have drawn tremendous interests since 20 years ago due to their excellent optoelectronic advantages. First, QDs exhibit large coefficients in the quantum confinement effect. In addition, multiple exciton generation can be obtained own to the generated multiple electron-hole pairs in one single photo absorption. Finally, QDs absorption can be tuned by the synthesized QDs size. [1-2]

The exploitation of these superior properties requires the knowledge of nanocrystal surface chemistry as this determines the size and morphology of the resultant NCs and hence the overall optoelectronic properties. Mass production of colloidal QDs is another advantage of this material, being made possible through the use of colloidal aqueous synthesis in which various capping ligands could be used to functionalize the surface of QDs without the need of inert atmosphere and using conventional solvents [3-4]. Introducing inorganic/organic capping ligands passivates the dangling bonds on the surface of QDs and reduces the presence of charge trapping sites [5]. On the negative side, Incorporation of long insulating organic molecules on the surface of QDs for dispersion in organic solvents results in to weak inter-particle interaction leading to the hampered charge separation and charge transfer[6]. Therefore, logical efforts must be directed towards the reduction of inter-QD distance and lowering of energetic barrier along with effective surface states passivation to improve the optoelectronic properties and devices performance. Reducing the alkyl chain length of organic ligands by their short alkyl-chain counterparts or

inorganic species has been reported to improve the surface passivation and optoelectronic properties [7-12]. However, there is tradeoff between electronic defects and the charge transport properties when shorter ligands are used.

To address this issue, a novel and facile strategy to realize selective inorganic ligand (S^{2-}) exchange on Pb-rich surface of PbS colloidal quantum dots (QDs) has been demonstrated. This was achieved via xanthate ligand decomposition at room temperature without damaging the QDs surface. This proposed method offers an amicable solution for the limitation that inorganic-terminated colloidal QDs are restricted by the specific requirement to solvents with high dielectric constant.

2.2 Preparation of PbS quantum dots and device fabrication

2.2.1 Materials

All chemicals were purchased without further purification. And instruments used in experiments are listed below.

Table 2.1 Reagents used in experiments

Reagent	Purity	Company
Zinc acetate	99.99%	Sigma-aldrich
Lead(II) Oxide	99.0%	Wako Pure Chemical Industry
oleic acid	99.0%	Tokyo Chemical Industry
1-octadecene	99.0%	Wako Pure Chemical Industry
Hexamethyldisilathiane (TMS)	99.9%	Sigma-aldrich
Cadmium Chloride	95.0%	Wako Pure Chemical Industry
tetradecylphosphonic acid (TDPA)	99.0%	Tokyo Chemical Industry

oleylamine	>50%	Tokyo Chemical Industry
tetrahydrofuran	99.0%	Wako Pure Chemical Industry
potassium hydroxide	-	Wako Pure Chemical Industry
carbon disulfide	99.0%	Wako Pure Chemical Industry
ethylene dithiol	99.0%	Wako Pure Chemical Industry
Cetyltrimethylammonium bromide (CTAB)	99.0%	Wako Pure Chemical Industry

Table 2.2 Instruments used in experiments

Apparatus	Model	Company
Spin-coater	SC-150	Oshigane Co.,Ltd.,Japan
Hot plate	C-MAG HS7	IKA Co.,Ltd.,Germany
Ohmmeter	FULL-TECH FT-101	FULL-TECH Co.,Ltd., Japan
Solar simulator	CEP-2000	Bunkou Keiki Co., Ltd., Japan
Standard solar cell	BS-520BK	Bunkou Keiki Co., Ltd., Japan
X-ray diffractometer	Rigaku	Rigaku Co., Ltd., Japan
TEM	JEM-2100F	JEOL Co., Ltd., Japan
Uv-visible	V-670	JASSCO Co., Ltd., Japan
FT-IR	JASCO FTIR 4100	JASSCO Co., Ltd., Japan
Thermogravimetric	DTG-60	Rigaku Co., Ltd., Japan
AFM	NanoScope IV	Rigaku Co., Ltd., Japan

2.2.2 Synthesis and characterization of PbS quantum dots and xanthate

Synthesis of potassium O-hexyl xanthate (KHX) : 5 ml distilled water was added in 30 ml tetrahydrofuran containing 2.75 g potassium hydroxide (KOH, 49 mmol). 1-hexanol (49 mmol, 5.01 g) was added to the above solution at room temperature and after stirring for another 1 h, carbon disulfide (73.4 mmol, 5.59 g) was added dropwise to the solution for 10 min l. The crude product thus obtained was washed with ethanol and ether consecutively to obtain potassium O-hexyl xanthate with a yield of 85 % after the evaporation of solvent.

PbS QDs: PbS QDs with the first excitonic peak at 1035 nm were synthesized according to previously reported method [13]. PbS quantum dots were synthesized following the procedure reported by Fischer et al [14]. 6 mmol PbO and 15 mmol oleic acid were added in a flask containing 50 ml of 1-octadecene. Solution was stirred and degassed for 20 min at room temperature, then degassing was continued for another 3h at 90°C. Subsequently, the solution was heated up to 120°C followed by swift injection of 3 mmol of hexamethyldisilathiane (TMS) diluted with 10 mmol of 1-octadecene under nitrogen. $CdCl_2$-TDPA-oleylamine solution [1 mmol $CdCl_2$, 0.1 mmol tetradecylphosphonic acid (TDPA), 3 g oleylamine] was injected when the solution mixture was cooled down to 75 °C (Figure 2.1). After cooling down to room temperature, PbS QDs were purified by washing with acetone and methanol. Finally, PbS QDs were collected by centrifugation and dried in vacuum. QDs were redispersed in octane or toluene.

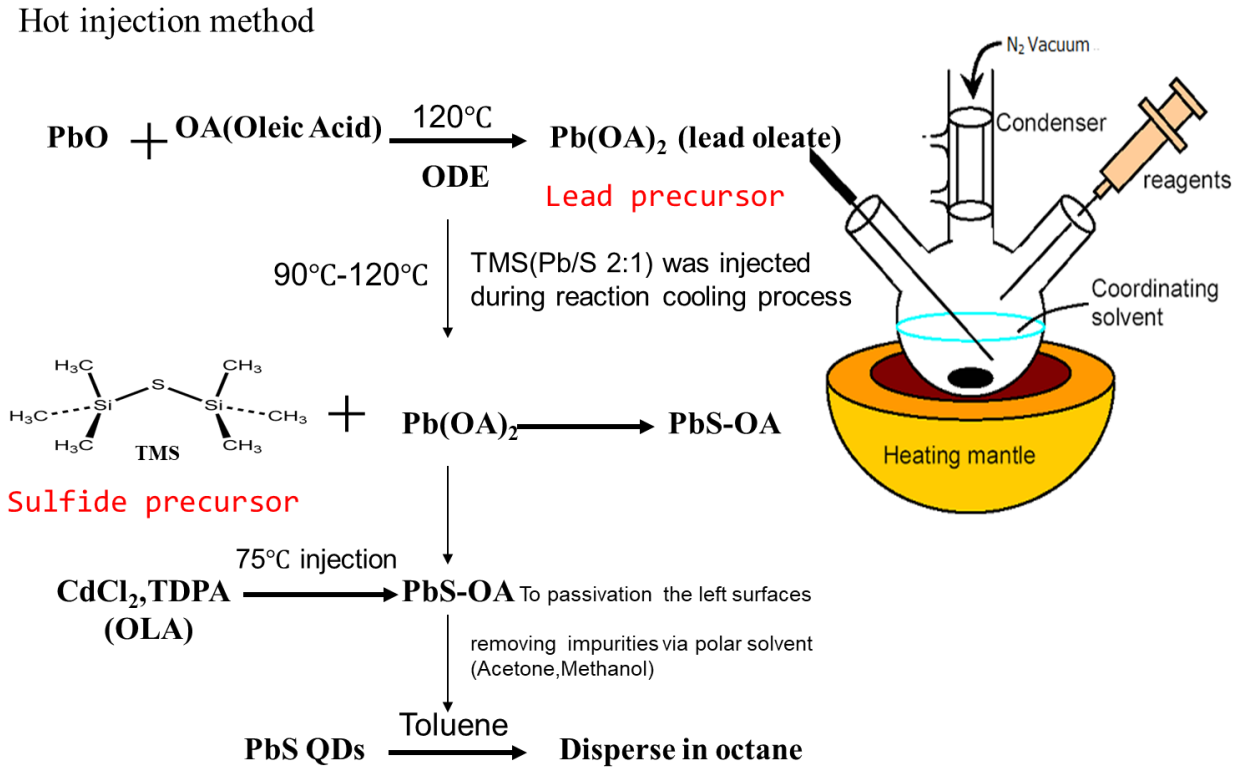

Figure 2.1. Procedure of PbS QDs synthesis.

2.2.3 Fabrication of PbS QDs device

5 ml of QDs dispersed toluene and 3 ml of KHX in methanol solution (130 mM) were mixed in homogeneous phase for several seconds, followed by centrifugation and drying in vacuum. Octane was added to disperse OA/Xth-QDs and the solution was filtered with 0.22 μm filter prior to spin coating. For the preparation of OA/Xth-QDs film, the glass substrates were cleaned by distilled water and acetone for 20 min each. Mesoporous TiO_2 was prepared by spin-coating from ethanol diluted TiO_2 paste (30 nm TiO_2 nanoparticle) followed heating at 125 °C for 20 min and 500 °C for 30 min. OA/Xth-QDs octane solution was spin-coated on the substrates, then the substrate was immersed in KHX acetonitrile solution (1 vol%, 3 vol% and 5 vol% respectively) for 5 seconds. OA/S-QDs were obtained through spin-coating to remove residual solvent. To

displace the remaining OA molecules, CTAB methanol solution (30 mM) was used to exchange the OA ligands according to previous method [14]. Finally, CTAB and sulfur-capped PbS QDs film was obtained (Figure 2.2).

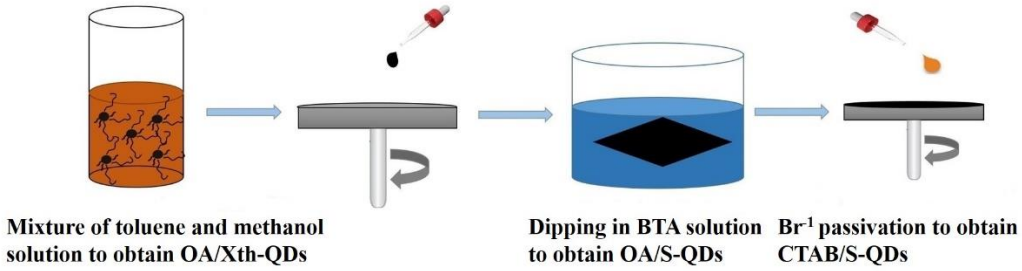

Figure 2.2. Schematic representation for the fabrication of sulfur-connected thin films of PbS QDs.

ZnO sol was prepared based on the previously reported method [15]. Typically, 0.1M of zinc acetate dihydrate and monoethanolamine (1:1) were dissolved in 2-methoxyethanol. Solution was filtered through a 0.2 μm filter syringe filter and used for spin coating on FTO substrate. Spin-coating was performed at 2000rpm for 30s, followed by annealing at 200°C for 10 min. CTAB-passivated QDs layer were deposited on ZnO substrate by typical layer-by-layer method as per the reported procedure[45]. Thin film of as-synthesized PbS colloidal layer was prepared by spin-coating at 2500 rpm for 15s and QDs film was treated with cetyltrimethylammonium bromide (CTAB) solution (30 mM) for 60s, then washed with methanol 3 times. This QDs spin coating procedure was repeated 8 times to achieve desired thickness. For the CTAB/S-passivated QDs, film was prepared as described above, and then repeated 8 times. Then two layers of ethylene dithiol (EDT) passivated QDs was deposited as p-type region. Finally, top Au electrode (100 nm) was thermally evaporated using shadow mask to complete the quantum dot sensitized solar cells (QDSSCs) used in this work (Figure 2.3).

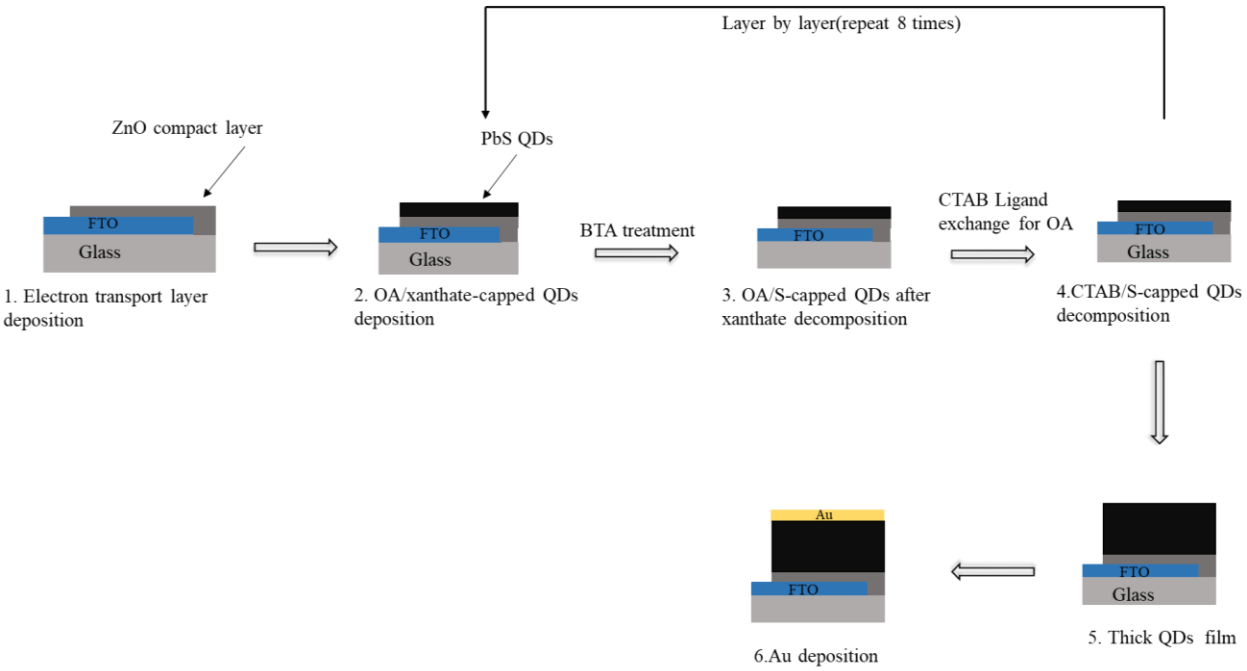

Figure 2.3. Schematic illustration of fabrication of QDs solar cell.

2.3 Results and discussion

2.3.1 Properties of QDs

To ensure that OA^- was exchanged by xanthate selectively, we added a certain amount of OA prior to xanthate ligand exchange in order to prevent uncontrolled displacement of oleic acid by xanthate ligands due to smaller binding energy on (100) surface than that on (111) facet[16]. OA/Xth-QDs was prepared as per the chemical reaction shown in the equation 1

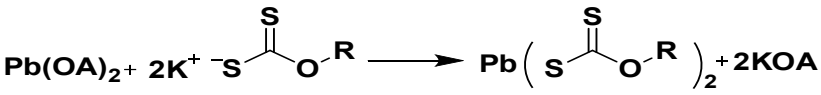

Secondly, deposited OA/Xth-QDs films were immersed into acetonitrile solution containing varying concentration of BTA (denoted as OA/S-QDs after BTA treatment). Finally, OA molecules were subjected to the ligand exchange by hexadecyltrimethylammonium bromide (CTAB) for

excellent passivation (denoted as CTAB/S-QDs). Thermogravimetric analysis (TGA) was performed to confirm QDs surface modification and structural characterization as shown in the Figure 2.4. It was found that OA/Xth-QDs and lead O-hexyl xanthate decomposed in same temperature range (120°C~130°C), indicating that partial OA was displaced by X-type xanthate (Xth) ligands due to high binding affinity of xanthate to lead. QDs continued to decompose up to 300°C, which is consistent with other reports on native OA-QDs[14]. OA/Xth-QDs exhibit a weight loss of 12% and 16% respectively with molar ratio of OA to xanthate to be 0.81.

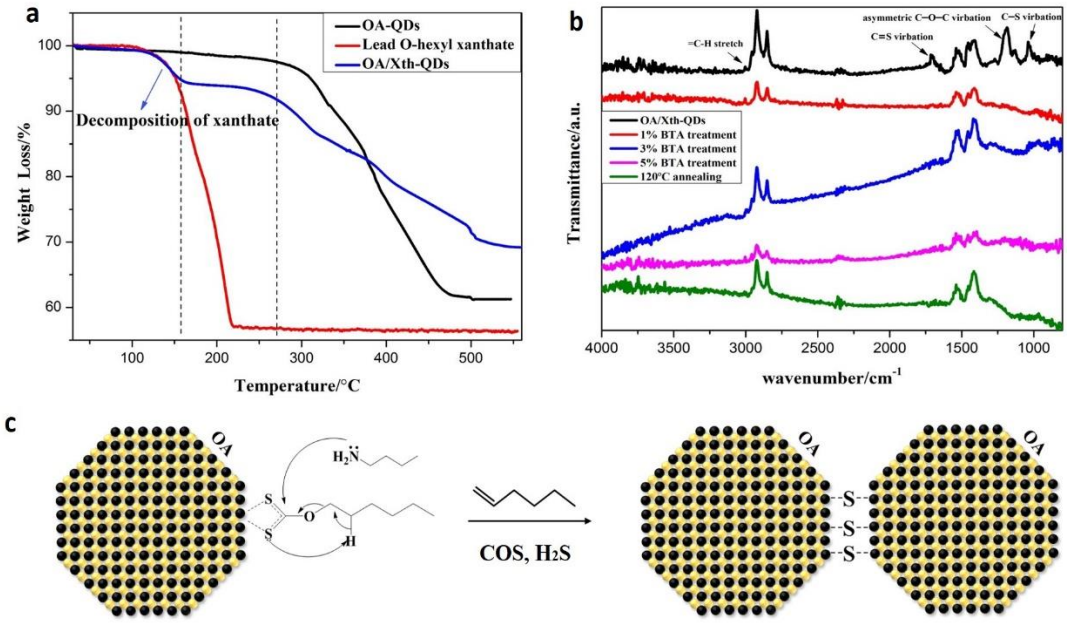

Figure 2.4. (a) Thermogravimetric analysis (TGA) to document weight loss of OA/Xth-capped QDs compared with lead O-hexyl xanthate and OA-QDs. (b) Scheme of OA/S-QDs obtained from OA/Xth-QDs after BTA treatment. (c) Attenuated total reflectance FTIR spectra of OA/Xth-QDs through 1%, 3%, 5% BTA and 120°C annealing treatment

Figure 2.4 c shows xanthate decomposition mechanism after BTA treatment, in which BTA acts as additive and promotes the decomposition of xanthate ligands leading to sulfur-crosslinking QDs via the formation of volatile reaction intermediates such as 1-hexene and carbonyl sulfide (COS). ATR-FTIR was performed to investigate the decomposition process for samples treated with varying BTA concentrations (1 vol%, 3 vol% and 5 vol% respectively). A

perusal of the FTIR results shown in the Figure 2.4 b. clearly indicates the disappearance of C-S, C-O and C=S stretching vibration at 1047cm^{-1}, 1189cm^{-1} and 1650cm^{-1} respectively[17] corroborating that lead xanthate were decomposed with the aid of BTA without any effect on OA.

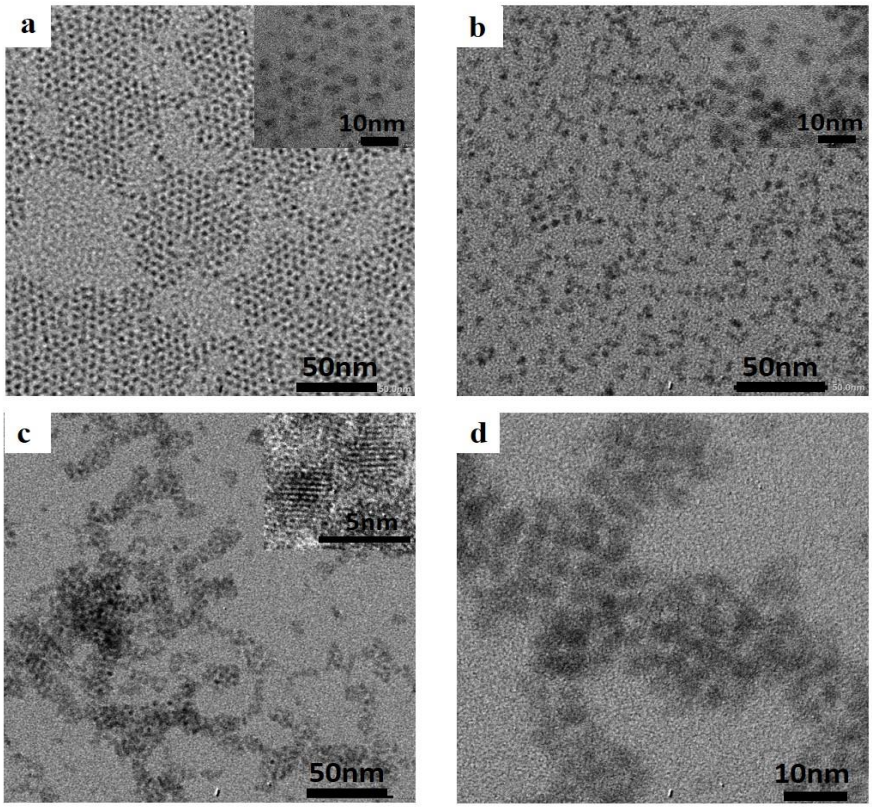

Figure 2.5. TEM images of (a) as-synthesized OA-QDs, (b) OA/Xth-QDs, (c) OA/S-QDs after 3% BTA treatment and (d) OA/S-QDs with 10nm scale bar. Inset images show the same samples correspondingly with different scale bar.

X-ray photoelectron spectroscopy (XPS) and TEM characterization was performed to confirm that xanthate ligands are exchanged on Pb-rich (111) facet preferentially. Usually X-type ligands are only displaced by X-type because direct exchange of X-type with other type ligands influences QDs surface charge neutrality [11]. From the XPS results summarized in the table 2.1, it can be noted that OA/Xth-QDs obtained from OA-QDs through xanthate ligand exchange, the ratio of lead to sulfur-interior remained unchanged (0.64). This suggests that X-type OA- on (111) facet were exchanged by X-type xanthate selectively and ligand exchange did not influence the

QDs surface charge neutrality. Figure 2.5 show the TEM of as-synthesized OA-QDs, OA/Xth-QDs and OA/S-QDs (3% BTA treatment) respectively. TEM analysis revealed that spacing between adjacent QDs was decreased due to the shorter alkyl chain length of xanthate and there was no structural change after the xanthate ligand exchange. OA/S-QDs showed further reduced spacing meanwhile adjacent QDs were connected by direct attachment after BTA treatment. Inset image of Figure 2.5 shows clearly that diffraction fringes were parallel providing evidence for the sulfur crosslinking of the QDs. Additionally, It can also be noted that ordered OA/S-QDs arrays (Figure 2.5 d) were formed after the xanthate decomposition, which was lacking for OA/Xth-QDs.

Table 2.3 Summary of PbS QDs chemical composition obtained from as-deposited films, including traditional CTAB-QDs, native OA-QDs, OA/Xth-QDs, OA/S-QDs and CTAB/S-QDs.

	Pb	S-total	S-interior	S-Xanthate(Xth)	Br	Ratio of (S^{2-} +0.5×Br^{-})/Pb^{2+}
CTAB-QDs	1	0.75	0.75		0.67	1.08
OA-QDs	1	0.64	0.64			0.64
OA/Xth-QDs	1	0.91	0.63	0.28		
OA/S-QDs (1%BTA treatment)	1	0.71	0.71	0		
OA/S-QDs (3%BTA treatment)	1	0.72	0.72	0		
OA/S-QDs (5%BTA treatment)	1	0.72	0.72	0		
CTAB/S-QDs	1	0.78	0.78	0	0.32	0.94

[a] All chemical compositions are normalized to Pb, S-total represents the total Sulfur amount in film, S-interior refers to sulfur content inside PbS QDs or sulfur content binding to Pb only, S-xanthate refers to sulfur content in xanthate.

XPS analysis was further performed to elucidate the effect of xanthate decomposition on QDs surface and its mechanism upon BTA treatment [18]. Wide band XPS spectra depicts the absence of N_{1s} around the binding energy of 400ev for different BTA concentration treatments (Figure 2.6). This is attributed to the disappearance of residual organic amine residues due to its high volatility. Table 2.3 shows the summary of lead and sulfur composition (normalized to Pb) measured by XPS obtained from native OA-QDs films, OA/Xth-QDs films, OA/S-QDs films after BTA treatment and CTAB/S-QDs film after CTAB ligands exchange. When OA was displaced by xanthate ligands, S_{2p} peak fitting (Figure 2.7) shows that a new S_{2p} peak is dominated at 160.7ev, which has been assigned to the xanthate ligands binding to the PbS surface. After the xanthate decomposition, one sulfur was left on the surface of QDs while other was removed as COS gas leading to increased amount of sulfur. Finally, adjacent QDs are connected by sulfur atoms. The S_{2p} peak of xanthate ligands disappeared and the amount of S-Pb bonds increased due to the formation of Pb-S bonds on surface. About a quarter amount of sulfur atoms in xanthate were left due to the decomposition reaction without the loss of sulfur, which is consistent with amount of sulfur atoms measured by XPS ($0.71 \approx 0.63+0.28/4$).

PbS QDs are promising materials for optoelectronic device due to their larger wave function overlaps, where stronger coupling between local wave functions generates a new delocalized state in QDs in the solid-states [19]. CTAB/S-QDs films were prepared on glass substrate by spin coating and subjected to electronic absorption spectral characterization. Two unique characteristics were noticed from the perusal of the solid-state electronic absorption spectra as shown in the Figure 2.6 b, first, apparent excitonic absorption signature was observed around 1000-1100nm implying that strong quantum confinement was retained after BTA and CTAB treatments. Second, there was spectral broadening of excitonic peak and enhancement of the

optical absorption as compared to that of CTAB-QDs films under the similar film thickness. Such behavior has been previously observed in the case of highly confined and coupled QDs as reported by Carey et al [20]. This demonstrates that sulfur substitution by CTAB to connect QDs results in stronger coupling of QDs. Inset of the Fig. 3b shows that 3% and 5% BTA treatment induced nearly similar full width at half maximum (FWHM) but higher than that of 1% BTA treatment indicating about the formation of dense QDs arrays.

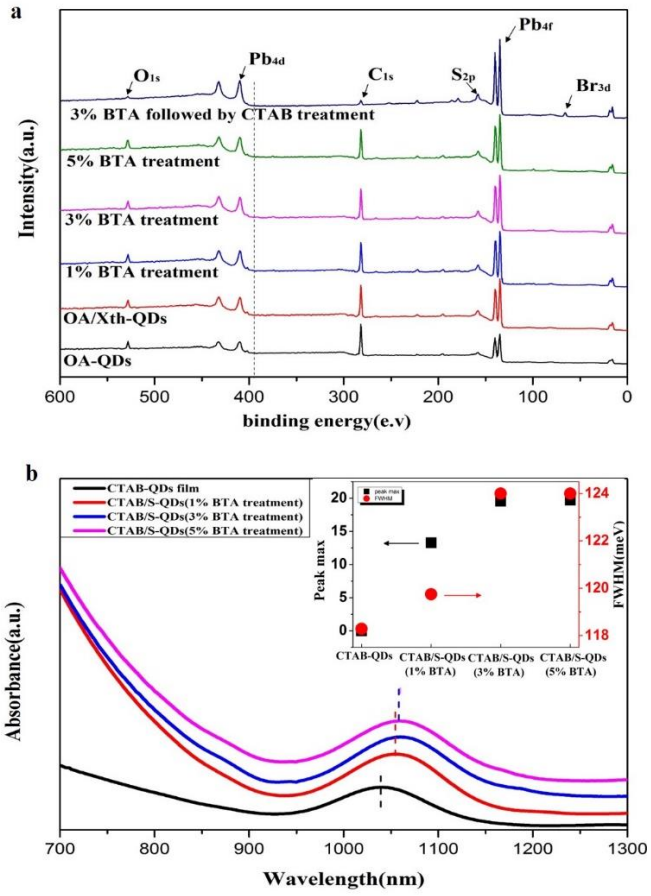

Figure 2.6. XPS wide scan spectrum of OA/Xth-capped QDs, OA/S-QDs treated with varying BTA concentration. (b) Absorption spectra of CTAB/S-QDs obtained after BTA treatment and CATB-QDs. Inset shows redshift (black) and broadening (red) of excitonic peak with different ligand composition and BTA treatment.

Negligible difference of sulfur contents between OA/S-QDs indicates that various BTA

concentration promoted decomposition reaction completely and no oxidation of sulfur like sulfate species formed on QDs surface (Figure 2.7). XPS spectra also confirm that sulfur atoms were not oxidized. Interestingly, it can be noted that X-type xanthate ligand exchange maintains the stoichiometry of internal S and Pb atoms as compared to traditional approach of displacing native ligands, which in turn prove that Pb atoms were not etched away and X-type xanthate only displace X-type OA^- preferably. Sulfur from xanthate were not displaced by CTAB, which is also consistent with reported reference that PbS QDs could not be repaired by other ligands [21]. We have calculated the ratio of inorganic components $[(S^{2-}+0.5\times Br^-)/Pb^{2+}]$ under different ligand exchange conditions considering charge of Br as -1, Pb as +2 and S as -2. Results of this calculation as summarized in the table 2.3 exhibits a significant increase in the ratio indicates improved charged balance due to the introduction of sulfur from xanthate molecules but not because of loss of internal S and Pb atoms.

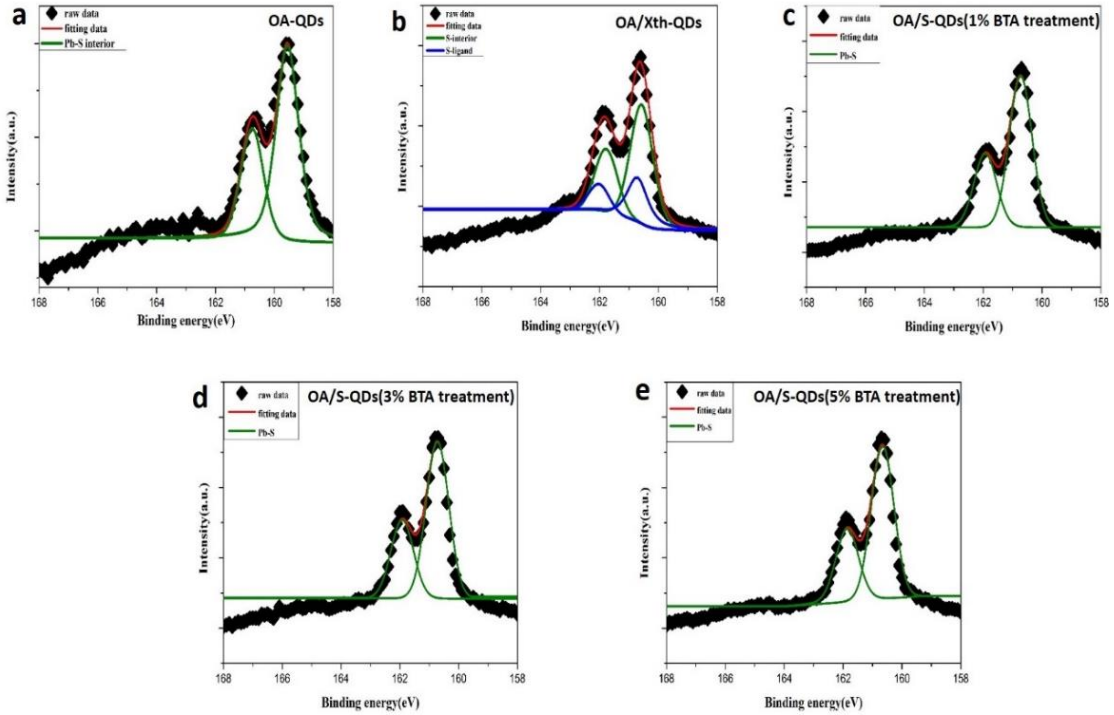

Figure 2.7. XPS spectra for S_{2p} peak of a) as-synthesized OA-QDs, b) OA/Xth-QDs, c) OA/S-QDs (1% BTA treatment), d) OA/S-QDs (3% BTA treatment), e) OA/S-QDs (5% BTA treatment).

2.3.2. Microstructural investigation of QDs

Figure 2.8 shows the schematic diagram comparing CTAB-QDs in the presence and absence of S-crosslinking. Decomposition of lead xanthate led to the formation of Pb-S bond after BTA treatment, allowing for decreased inter-dot spacing and dense packing finally leading to ordered CTAB/S-QDs. High quality films with excellent morphology and low roughness is crucial for the efficient charge transport since rough surfaces result in poor interfacial contact with electron (hole) transport layer[22]. Surface microstructural characterization was performed by AFM to examine the morphology of the QD films prepared by different concentration of BTA treatment. AFM images of CTAB/S-QDs films show smooth morphology with uniform distribution compared to that of CTAB-QDs films. A root mean square (Rms) roughness of 1% and 3% BTA treated CTAB/S-QDs films decreased to 0.74 and 1.41 nm from 5.72 nm for CTAB-QDs films as shown in the Figure 2.9. This morphology and surface roughness is comparable to samples prepared by transfer-printing process[22]and spray coating method[23]. At the same time, PbS QDs films were ordered

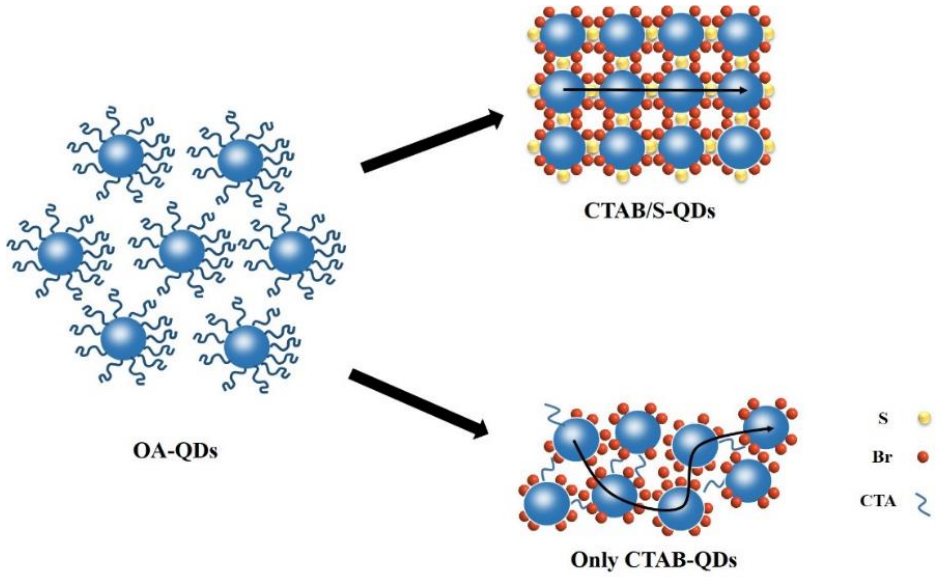

Figure 2.8. Schematics for the quantum dots film after different ligand exchange processes, sulfur-crosslinking of QDs promotes the formation of ordered QDs arrays compared to CTAB-QDs film.

and crack-free after 1% and 3% BTA treatments. In contrast, 5% BTA treatment results in poor morphology and non-uniformity, since primary amine have higher surface binding than OA[24].

Strongly coupled sulfur-crosslinking QDs are expected to have high charge mobility because ordered QD system can result in improved charge transport, which is of critical importance for device applications. In the case of FET, most of the carrier traps are filled resulted from higher fermi level raised by gate bias [25], but only non-trapped carriers are measured in the Hall-effect. [26] Therefore, both of these measurements provide the similar trend of mobility values which are close to the trap-free mobility especially for PbS QDs [27]. In this work, carrier mobility was determined by Hall-effect measurement using spin-coated PbS QDs thin films (30nm) measured at 300K. Table 2.4 summaries the carrier mobility for CTAB-QDs and CTAB/S-QDs films under different BTA treatment conditions as compared with reported data of as-synthesized OA-QDs films.

Table 2.4 Carrier Mobility measured by Hall Effect.

Type	OA-QDs[28]	CTAB-QDs	CTAB/S-QDs (1% BTA)	CTAB/S-QDs (3% BTA)	CTAB/S-QDs (5% BTA)
Mobility $cm^2/(v\ s)$	1.66×10^{-4}	5.7×10^{-2}	4.6×10^{-1}	5.0×10^{-1}	2.8×10^{-1}

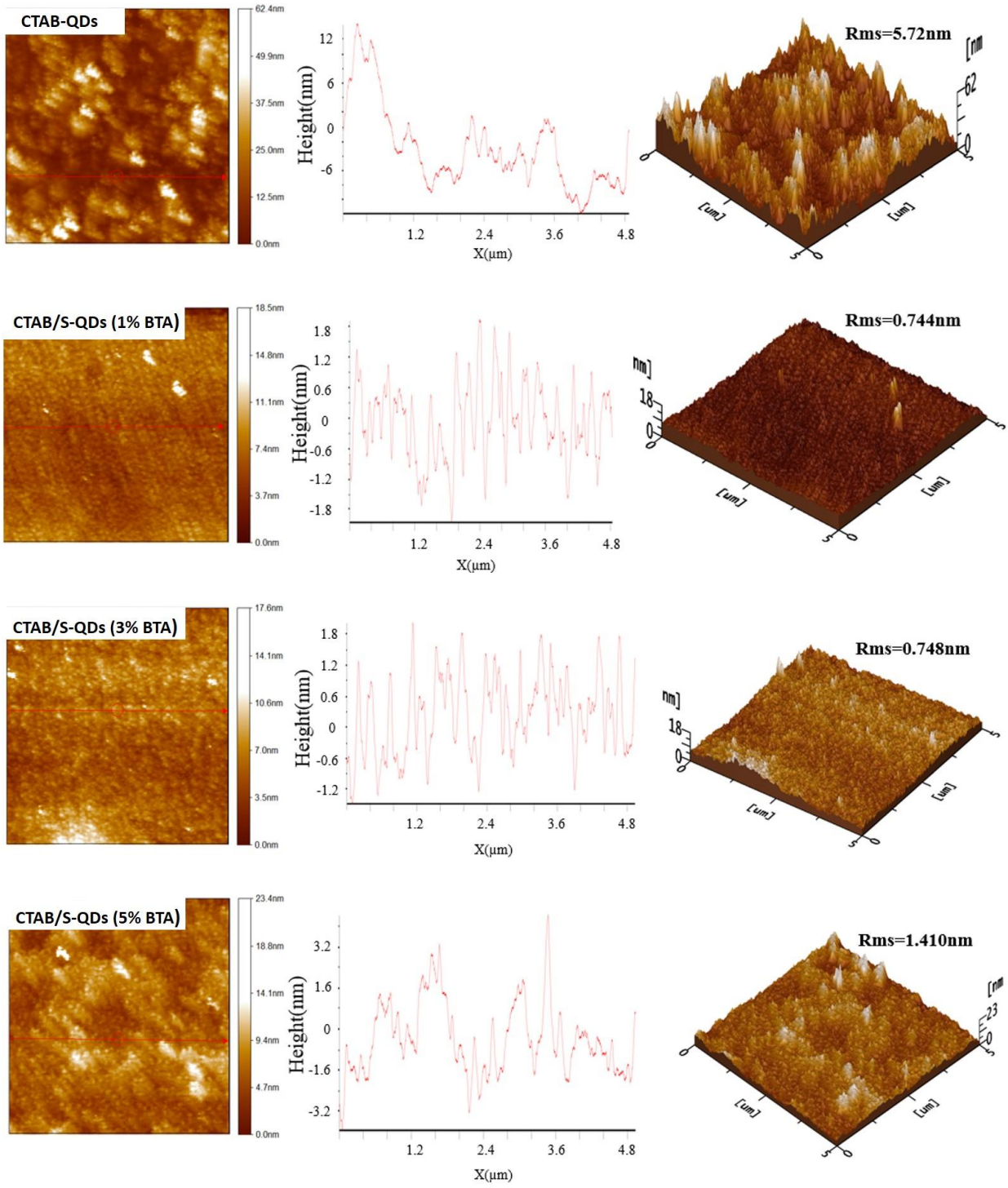

Figure 2.9. AFM images (height, line scan and 3D) for CATB-QDs, CTAB/S-QDs prepared after treatment with different BTA concentrations.

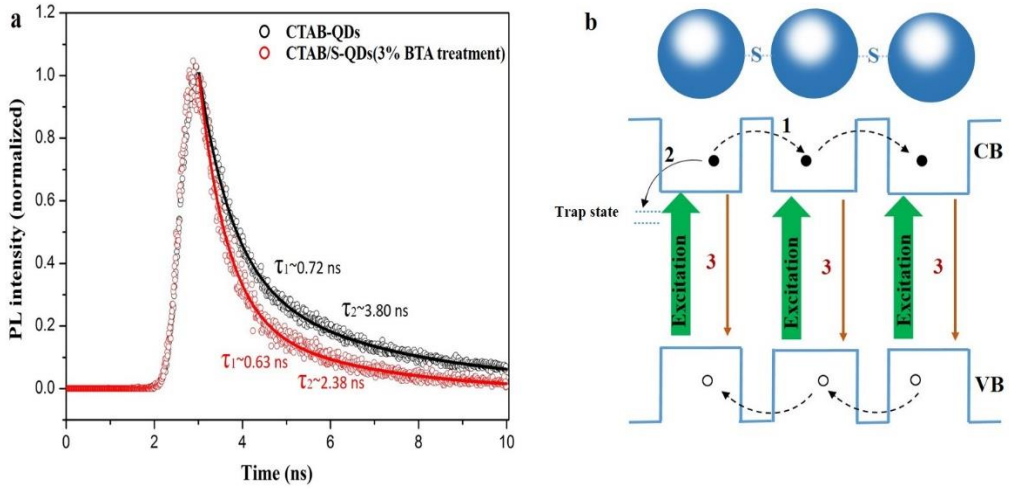

Figure 2.10 a) PL transient spectra of deposited CTAB-QDs film and CTAB/S-QDs film (3% BTA treatment), the corresponding solid lines represent bi-exponential fitting curve. b) Illustration of extion relaxtion process in stronger coupled CTAB/S-QDs array mainly including (1) exciton dissociation (2) charge trapping (3) radiative PL emission.

Obtained carrier mobility of CTAB/S-QDs were found to be nearly 3 orders of magnitude higher than that of as-synthesized OA-QDs. Apart from this, mobility of sulfur crosslinking QDs treated with varying BTA concentrations shows almost ten times higher than that without the introduction of S^{2-}. This excellent mobility can be attributed to the formation of ordered QDs array that leads to stronger coupling between adjacent QDs and optimizes charge transport pathways as shown schematically in the Figure 2.8, leading to facile charge transport in the QDs films [22]. Additionally, Photoluminescence (PL) transient spectra as shown in the Figure 2.10 a exhibited bi-exponential decays before and after the introduction of S^{2-}. Introduction of S^{2-} on the surface of QDs exhibits faster PL decay due to the increased dissociation of photoinduced excitons via charge transfer of strongly coupled QDs resulted from high mobility of sulfur-crosslinking QDs arrays. [21] This indicates that photoinduced carriers can be easily extracted in QDs film before recombination from trap sites and radiative emission, as schematically shown in the Figure 2.10 b.

We have introduced bromide to passivate QDs aiming towards suppression of mid-gap electronic traps [29].

2.3.3. Fabrication of devices and performance

Encouraged by improved carrier transport and validate the advantage of CTAB and sulfur passivated QDs, efforts were directed to investigate their photovoltaic behavior by fabricating QD-sensitized solar cells (QDSSC). A representative CTAB/S-QDs (3% BTA treatment) was utilized for QDSSC fabrication in the device architecture as shown schematically in the Figure 2.11. A ZnO compact layer was prepared using Zinc acetate dehydrate solution, serving as electron extraction layer. CTAB/S-PbS QDs layer was deposited on to FTO/ZnO substrate. Reference device was also made by using only CTAB-passivated PbS QDs for comparison. Coating of PbS QD layer was then followed by 2 layers of p-type QDs film prepared by the ethanedithiol (EDT) exchange. Finally, top Au electrode was thermally evaporated to complete the QDSSC. Fig. 7b depicts the photovoltaic (J-V) curves for the QDSSCs fabricated using CTAB-QDs and CTAB/S-QDs layer as photosensitizer after simulated solar irradiation at 1 sun. J-V curves reveal that QDSSC fabricated by CTAB/S-QDs exhibited a short circuit current density (Jsc) of 26.04 mA/cm^2, an open circuit voltage (Voc) of 0.43 V and fill factor (FF) of 0.44 leading of power conversion efficiency (PCE) of 4.96 %. Contrary to this, QDSSC fabricated using only CTAB-QDs without introduction of S-crosslinking QDs resulted in to hampered PCE of 3.04 % with Jsc, Voc and FF of 20.07 mA/cm^2, 0.41 V and 0.37, respectively.

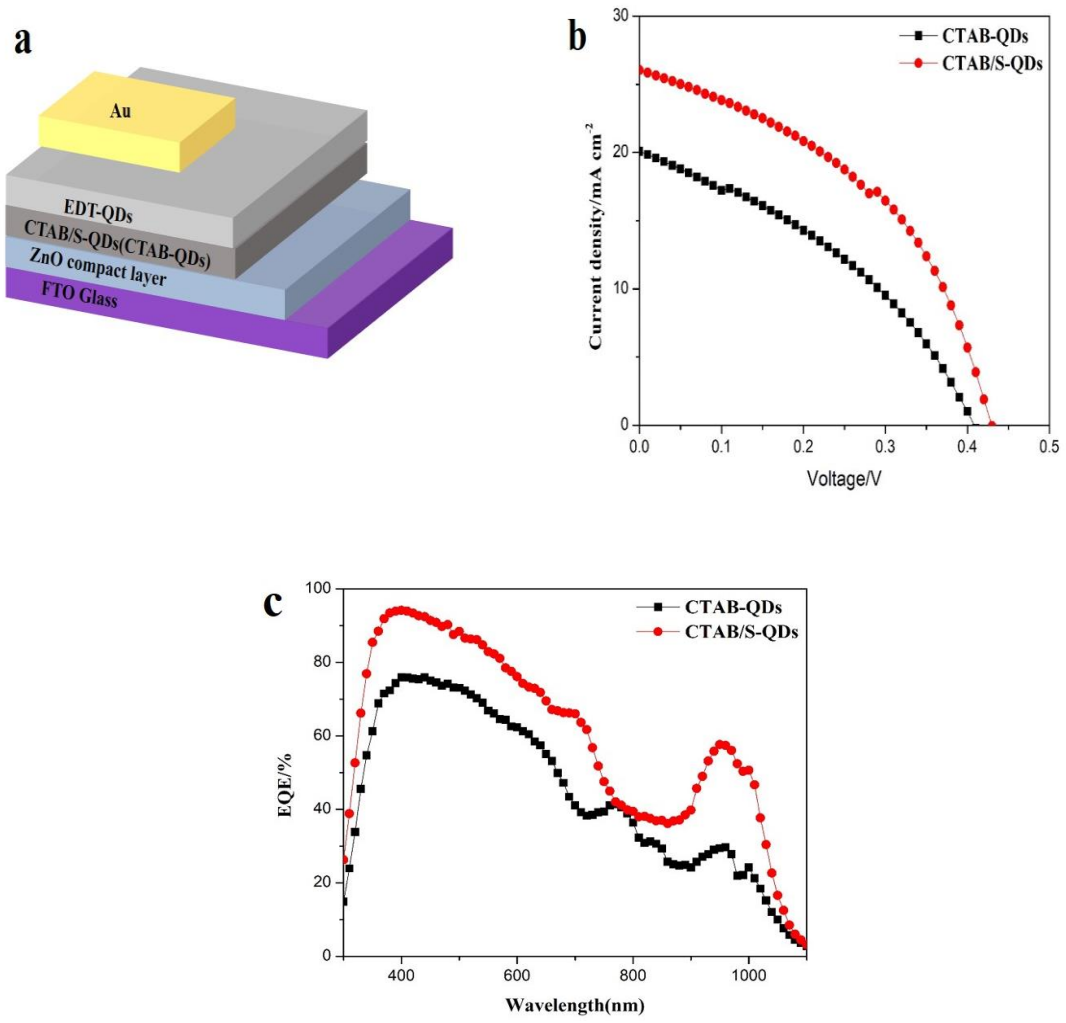

Figure 2.11. (a) Schematic illustration of QDs solar cell. (b) J-V curve under simulated AM 1.5G illumination for the CTAB-QDs and CTAB/S-QDs layer as the n-type. (c) External quantum efficiency (EQE) spectra for the CTAB-QDs and CTAB/S-QDs layer as the n-type.

Although all of the photovoltaic parameters were found to be increased for CTAB/S-QDs (with S-crosslinking) based devices as compared to that their CTAB/-QDs (without S-crosslinking) device counterparts but improvement in the Jsc (from 20 mA/cm^2 to 26 mA/cm^2) was responsible for remarkable boost in the PCE. This clearly justifies the importance and role-played by S-crosslinking QDs on the facile transport of photogenerated charge carriers, Photocurrent action spectrum (a plot of external quantum efficiency (EQE) as function of wavelength) has been widely

used for the explanation of differential photovoltaic behavior in general and Jsc in particular. A perusal of photocurrent action spectra shown in the Figure 2.11 c, clearly corroborates that there was remarkable improvement in the photon harvesting for the CTAB/S-QDs based QDSSCs in the entire wavelength (400 nm-1100 nm) region as compared to that of devices based on CTAB-QDs. Enhanced PCE (especially Jsc) observed for QDSSCs based on S-crosslinking QDs after 1 sun illumination (Figure 2.11 b) was further confirmed by estimation of integrated Jsc from the photocurrent action spectra shown in the Figure 2.11 c. Increase in the integrated Jsc from 19.23 mA/cm^2 (CTAB-QDs devices) to 25.5 mA/cm^2 (CTAB/S-QDs devices) indicates the efficient carrier transport and charge extraction.

2.4 Conclusions

In conclusion, selective exchange of OA by xanthate moieties on the QDs surface was demonstrated as confirmed by TEM and XPS leading to stronger inter-QDs coupling. N-butylamine treatment decomposed xanthate molecules as QDs surface ligand into Pb-S bond to form sulfur-crosslinking QDs array at room temperature. Decomposition of xanthate precursor was responsible for providing the driving force for formation of sulfur- crosslinking QDs with smooth morphology as confirmed by TEM and AFM. The increased mobility of sulfur-crosslinking QDs films shows one order of magnitude higher than reference CTAB-QDs films due to the packed and ordered array of QDs. A high mobility with strong quantum confinement would become an asset in QDs device with ordered QDs array. This improved mobility and decreased QDs film roughness facilitate their use of a p-type light absorbing layer for QDSSCs. QDSSCs fabricated using Sulfur-crosslinking promoted CTAB/S-QDs as photosensitizer led to improved PCE especially the notable increase in Jsc from 20 mA/cm^2 to 26 mA/cm^2. This novel processing method provides potential strategy to apply inorganic chalcogenide nanocrystals in semiconductor device and is

promising in eventual device application through controlling stoichiometry and QDs surface morphology.

References

[1] A. Nozik, *Physica E: Low-dimensional Systems and Nanostructures* **2002**, 14, 115.

[2] M. Hanna, A. Nozik, *Journal of Applied Physics* **2006**, 100, 074510.

[3] K. O. Aruda, M. Bohlmann Kunz, M. Tagliazucchi, E. A. Weiss, *The journal of physical chemistry letters* **2015**, 6, 2841.

[4] M. Liu, O. Voznyy, R. Sabatini, F. P. G. de Arquer, R. Munir, A. H. Balawi, X. Lan, F. Fan, G. Walters, A. R. Kirmani, *Nature materials* **2017**, 16, 258.

[5] A. H. Ip, S. M. Thon, S. Hoogland, O. Voznyy, D. Zhitomirsky, R. Debnath, L. Levina, L. R. Rollny, G. H. Carey, A. Fischer, *Nature nanotechnology* **2012**, 7, 577.

[6] M. S. Kodaimati, C. Wang, C. Chapman, G. C. Schatz, E. A. Weiss, *ACS nano* **2017**, 11, 5041.

[7] A. Nag, M. V. Kovalenko, J.-S. Lee, W. Liu, B. Spokoyny, D. V. Talapin, *Journal of the American Chemical Society* **2011**, 133, 10612.

[8] A. T. Fafarman, W.-k. Koh, B. T. Diroll, D. K. Kim, D.-K. Ko, S. J. Oh, X. Ye, V. Doan-Nguyen, M. R. Crump, D. C. Reifsnyder, *Journal of the American Chemical Society* **2011**, 133, 15753.

[9] H. Zhang, J. Jang, W. Liu, D. V. Talapin, *ACS nano* **2014**, 8, 7359.

[10] S. Ananthakumar, J. Ramkumar, S. M. Babu, *Solar Energy* **2014**, 106, 151.

[11] D.-K. Ko, A. Maurano, S. K. Suh, D. Kim, G. W. Hwang, J. C. Grossman, V. Bulović, M. G. Bawendi, *ACS nano* **2016**, 10, 3382.

[12] N. S. M. Mustakim, C. A. Ubani, S. Sepeai, N. A. Ludin, M. A. M. Teridi, M. A. Ibrahim, *Solar Energy* **2018**, 163, 256.

[13] J. Chang, Y. Kuga, I. Mora-Seró, T. Toyoda, Y. Ogomi, S. Hayase, J. Bisquert, Q. Shen, *Nanoscale* **2015**, 7, 5446.

[14] A. Fischer, L. Rollny, J. Pan, G. H. Carey, S. M. Thon, S. Hoogland, O. Voznyy, D. Zhitomirsky, J. Y. Kim, O. M. Bakr, *Advanced Materials* **2013**, 25, 5742.

[15] L. K. Jagadamma, M. Abdelsamie, A. El Labban, E. Aresu, G. O. N. Ndjawa, D. H. Anjum,

D. Cha, P. M. Beaujuge, A. Amassian, *Journal of Materials Chemistry A* **2014**, 2, 13321.

[16] M. T. Frederick, V. A. Amin, L. C. Cass, E. A. Weiss, *Nano letters* **2011**, 11, 5455.

[17] J. Leppinen, *International Journal of Mineral Processing* **1990**, 30, 245.

[18] M. M. Krause, L. Jethi, T. G. Mack, P. Kambhampati, *The journal of physical chemistry letters* **2015**, 6, 4292.

[19] J.-H. Choi, A. T. Fafarman, S. J. Oh, D.-K. Ko, D. K. Kim, B. T. Diroll, S. Muramoto, J. G. Gillen, C. B. Murray, C. R. Kagan, *Nano letters* **2012**, 12, 2631.

[20] G. H. Carey, L. Levina, R. Comin, O. Voznyy, E. H. Sargent, *Advanced Materials* **2015**, 27, 3325.

[21] H. Zhang, B. Hu, L. Sun, R. Hovden, F. W. Wise, D. A. Muller, R. D. Robinson, *Nano letters* **2011**, 11, 5356.

[22] T.-H. Kim, K.-S. Cho, E. K. Lee, S. J. Lee, J. Chae, J. W. Kim, D. H. Kim, J.-Y. Kwon, G. Amaratunga, S. Y. Lee, *Nature photonics* **2011**, 5, 176.

[23] K. J. Chen, H. C. Chen, K. A. Tsai, C. C. Lin, H. H. Tsai, S. H. Chien, B. S. Cheng, Y. J. Hsu, M. H. Shih, C. H. Tsai, *Advanced Functional Materials* **2012**, 22, 5138.

[24] J. K. Cooper, A. M. Franco, S. Gul, C. Corrado, J. Z. Zhang, *Langmuir* **2011**, 27, 8486.

[25] S. Z. Bisri, C. Piliego, M. Yarema, W. Heiss, M. A. Loi, *Advanced Materials* **2013**, 25, 4309.

[26] J. Jang, W. Liu, J. S. Son, D. V. Talapin, *Nano letters* **2014**, 14, 653.

[27] M. J. Speirs, D. N. Dirin, M. Abdu-Aguye, D. M. Balazs, M. V. Kovalenko, M. A. Loi, *Energy & Environmental Science* **2016**, 9, 2916.

[28] M. M. Tavakoli, A. Tayyebi, A. Simchi, H. Aashuri, M. Outokesh, Z. Fan, *Journal of nanoparticle research* **2015**, 17, 9.

[29] J. Tang, K. W. Kemp, S. Hoogland, K. S. Jeong, H. Liu, L. Levina, M. Furukawa, X. Wang, R. Debnath, D. Cha, *Nature materials* **2011**, 10, 765.

Chapter 3. Interface engineering of organic-inorganic perovskite solar cells to enhance efficiency and stability in humid air

3.1 Introduction

Organic-inorganic perovskite materials based on methylammonium lead iodide ($CH_3NH_3PbI_3$) have attracted tremendous attention since the first report on perovskite-sensitized solar cells in 2009 by Miyasaka et al.[1] Just within a few years, the power conversion efficiency (PCE) has increased exponentially from 3.8% to 22.1%,[2] the success of perovskite solar cell is due to its long exciton diffusion length, low exciton binding energy and high charge mobility. [3-5] However, the large number of traps residing in the perovskite layer and at the interface are unavoidable in polycrystalline films, resulting in nonradiative charge recombination which will reduce the carrier lifetime. Much efforts have been devoted to achieve high efficiency and intrinsic stability in planar architecture of photovoltaic device. Interfacial engineering plays an important role for improving the charge extraction capability, perovskite crystal growth and further photo-harvesting. When light was absorbed by perovskite layer in solar cells, photoinduced carriers diffuse toward contact layer spontaneously, the formed charge-depletion region makes the charge transport across the interface happen through equalizing the Fermi energy level,[6] however, charge extraction is subjected to recombination at the interface due to the unavoidable interfacial trap sites,[6] also, ion migration and accumulation at the external interface is thought to be responsible for observed hysteresis behaviors.[7] So far, there has been a variety of organic interfacial modulation to mitigate the influence of defects on the charge transfer kinetics and energetically favorable rapid nucleation, such as amino acid, self-assembled layer (SAM).[8-10] One of the main

challenges for scale-up production of perovskite solar cells is the device stability, this issue can be addressed by interfacial engineering.[11-12] However, these approaches involved multiple and complex fabrication process or using complicated organic molecules which is not favorable in terms of fabrication cost. Additionally, the effectiveness of passivation for defects were limited due to the unavoidable defect in the interconnection among organic compounds.[13]

Non-negligible loss of halide ions or undercoordinated Pb^{2+} in $CH_3NH_3PbI_3$ ($MAPbI_3$) film near the interface with ETL contributes to more traps during the perovskite annealing and crystallization which reduces the charge carrier collection.[14-15] Electronic coupling between SnO_2 ETL and perovskite allows for efficient electron extraction and this reduces charge accumulation near the interface,[10, 16] which results in strong hysteretic behavior. In order to suppress the deep traps and enhance passivation between perovskite grain boundaries and crystallinity, sulfur-containing molecules or solvents have been showed to form an adduct with PbI_2 which is a Lewis acid through the interaction with sulfur bearing Lewis base,[17-19] other examples include thiophene derivatives with π- conjugated system can directly coordinate with lead atoms in perovskite,[18] where the sulfur atoms with lone pair electrons in thiophene derivatives can interact with perovskite valance band, leading to efficient carrier extraction via thiophene and high efficiency device. In addition, thiourea,[20] thiadiazole derivatives[21] containing S-donor all could coordinate with perovskite to control perovskite nucleation and crystal growth, which confirms that weak interaction between Pb and sulfur ($R_2C{=}S{\cdot}PbI_2$) strongly influence the grain size, perovskite morphology and device efficiency.

3.2 Materials and experiments

3.2.1 Materials

All chemicals were purchased without further purification. Which are listed below.

Table 3.1 Reagents used in experiments

Reagent	Purity	Company
SnO_2 colloids	15% in water	Alfa Aesar
Zinc powder	99.99%	Sigma-aldrich
Hydrochloric acid	36.5%	Wako Pure Chemical Industry
ITO glass	Glass	Opvtech
PbI_2	98%	Tokyo Chemical Industry
CH_3NH_3I	99%	Tokyo Chemical Industry
Ethyl acetate	99.99%	Sigma-aldrich
LiTFSI	99.99%	Macklin Co., LTD
Spiro-MeOTAD	99.7%	Macklin Co., LTD
4-tert-butylpyridine	AR	Sigma-aldrich
Chlorobenzene	99.9%	Sigma-aldrich
N, N-dimethylformamide	99.99%	Sigma-aldrich
Dimethyl sulfoxide	99.99%	Sigma-aldrich
Au	-	Macklin Co., LTD

3.2.2 Perovskite devices fabrication and characterization

ITO substrates were sequentially sonicated with distilled water, isopropanol, acetone, water

for 20 minutes in each solvent, the ITO substrates were further treated with UV-O_3 for 15 minutes prior to deposition of SnO_2 ETL. Diluted SnO_2 colloid precursor was spin-coated on glass/ITO, and then annealed in ambient air at 200°C for 30min. For sulfur functionalized SnO_2, 0.03M potassium O-hexyl xanthate in methanol was loaded on SnO_2 ETL for 2min, then the ITO/SnO_2 substrate was spin-coated at 3000rpm for 20s and washed thoroughly by methanol 3 times, finally the substrate was annealed at 130 °C for 10min to decompose xanthate molecules. $MAPbI_3$ perovskite precursor solution was prepared by dissolving MAI (1.5M) and PbI_2 (1.5M) in mixed solvent DMF:DMSO (4:1). 80 μL of precursor solution was spin-coated on ITO/SnO_2 ETL substrate at 4000 rpm for 25s at 60% RH, during the spin coating process, 500 μL ethyl acetate was quickly dripped on the spinning SnO_2 substrate, and then the film was annealed on a hot plate at 100 °C for 10min. after cooling down to room temperature, spiro-OMeTAD in chlorobenzene (72mg/ml) was deposited on ITO/SnO_2 (or SnO_2/S)/ perovskite substrate by spin-coating, spiro-OMeTAD was added with 17.5 μL Li-TFSI in acetonitrile(520mg/ml) and 28.8 μL 4-tertbutylpyridine. Finally, 80nm gold was deposited by thermal evaporation onto the spiro-OMeTAD layer.

For the characterization, **t**he current density-voltage characteristics of solar cells were measured under AM 1.5G simulated solar illumination. The external quantum efficiencies were measured by illuminating solar cells under monochromatic light from 900nm to 300nm (300W Xenon lamp with a monochromator, Newport 74010). Perovskite film morphology were characterized by SEM (HITACHI S4800). XRD pattern was analyzed by D8 X-ray diffractometer, using Cu Kα radiation. The steady-state photoluminescence (PL) and timed-resolved PL measurement was obtained by the Fluorolog-3-p spectrophotometer by excitation light. X-ray photoelectron spectroscopy (XPS) was performed by XPS system with Thermo Scientific,

ESCLAB 250Xi. Electrochemical impedance spectra was measured by an electrochemical workstation (Parstat 2273, Princeton) under 0.6V positive bias. Thermally stimulated current (TSC) was performed using TS-FETT electron trapping measuring system (Rigaku).

3.3 Results and discussion

3.3.1 Interface sulfur functionalization

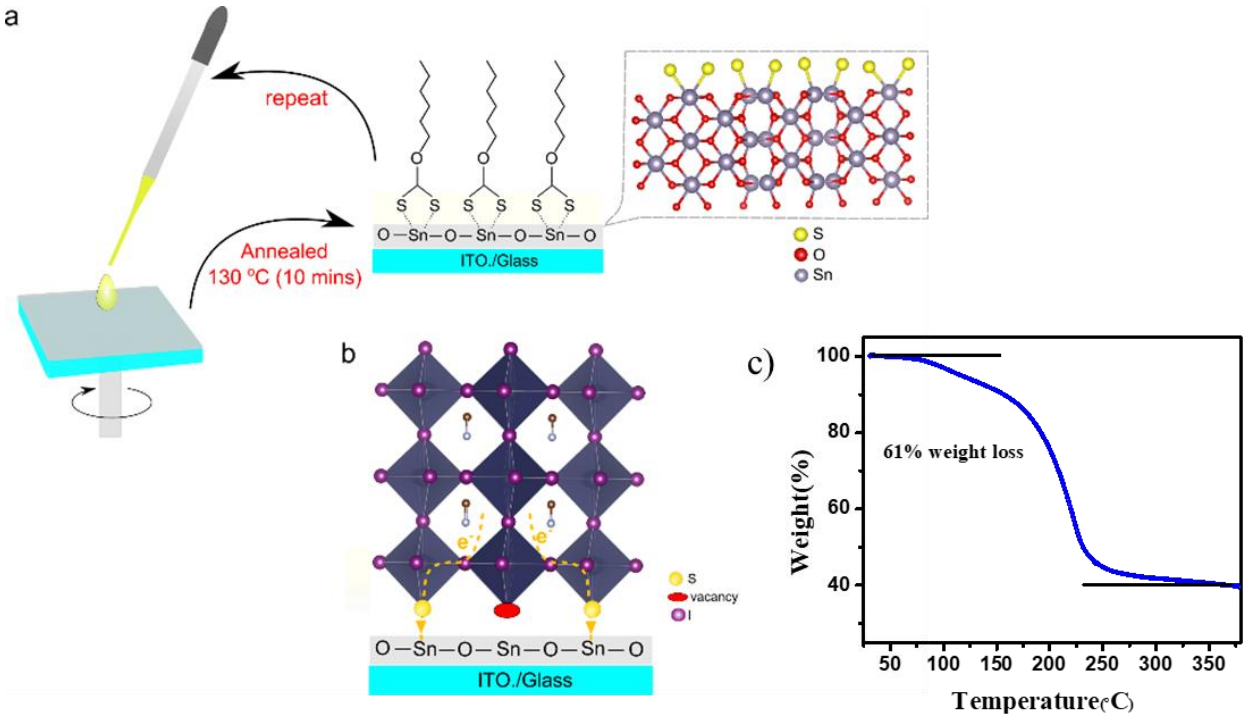

Figure 3.1 a) sulfur-functionalized electron transport layer via xanthate annealing. b) Device interfacial structure. c) Thermogravimetric analysis (TGA) to document the weight loss of decomposition, Tin xanthate began to decompose from 130 °C to 150°C with 61% weight loss, consistent with xanthate decomposition mechanism.

SnO_2 compact layer is used as electron transport layer (ETL), sulfur functionalization on SnO2 surface is employed by the xanthate molecules decomposition at relatively low temperature.

Figure 3.1 a shows the schematic diagram of xanthate deposition process where tin xanthate precursor was decomposed into tin sulfide[22] at about 130°C revealed by thermogravimetric analysis (Figure 3.1 c). Figure 3.1 b demonstrates the device structure upon interfacial sulfur functionalization. Xanthate solution on SnO_2 ETL through chemical binding was annealed for several minutes to ensure complete xanthate decomposition at 130°C. attenuated total reflection-FTIR (ATR-FTIR) measurement and X-ray photoelectron spectroscopy (XPS) before and after annealing treatment of xanthate respectively is shown in Figure 3.2 a,b.Peak of xanthate C-S bonds at about 1030 cm^{-1} appears and disappeared completely again after annealing, resulting in sulfur

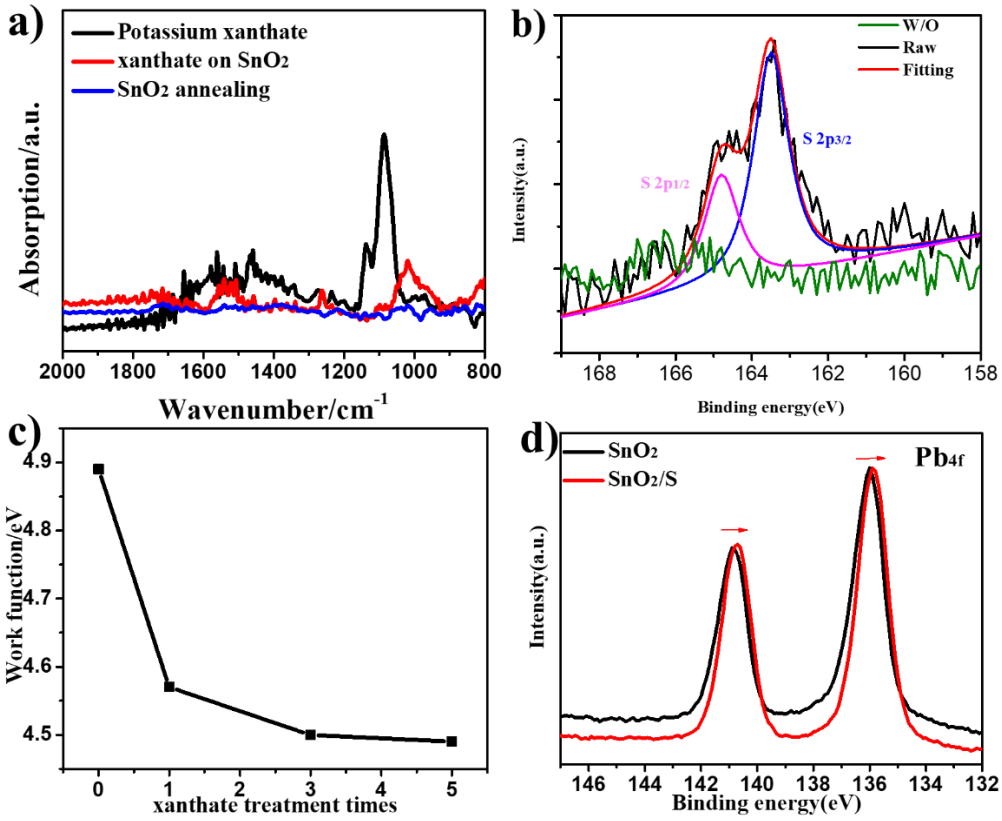

Figure 3.2 a) Attenuated total reflectance FTIR spectra of potassium xanthate, xanthate loading on SnO_2 ETL and annealing treatment of xanthate on SnO_2 ETL. b) X-ray photoelectron spectroscopy (XPS) of S2p of SnO_2 ETL with and without sulfur functionalization. c) Work function of SnO_2 ETL as a function of xanthate treatment times. d) XPS spectra of Pb4f upon PbI_2 deposition on SnO_2 ETL under high-resolution.

functionalization on SnO_2 surface. The presence of sulfur revealed by the additional peaks at 163.5 eV and 164.7 eV (corresponding to $S2p_{3/2}$ and $S2p_{1/2}$ respectively) in the case of sulfur functionalized SnO_2 was observed.

Figure 3.2 c shows the work function (WF) of SnO_2 with and without sulfur functionalization as a function of xanthate treatment times, A WF value of 4.89eV for untreated SnO_2 ETL was obtained, and upon xanthate treatment the WF decreased to 4.57, 4.50 and 4.49 eV after 1, 3, 5 times xanthate treatment respectively, this decreased WF will contribute to better energy level alignment and facilitating electron extraction from SnO_2 ETL.[9, 23] We then examined the XPS spectra of Pb_{4f} through PbI_2 deposition on SnO_2 with or without sulfur functionalization. The slightly shifted binding energies to lower energies for the Pb valence electron in $4f_{7/2}$ and $4f_{5/2}$ on sulfur functionalized SnO_2 surface (Figure 3.2 d), proved the presence of chemical interaction between PbI_2 and sulfur on SnO_2 surface due to the coordination reaction of sulfur with perovskite.

3.3.2 Optoelectronic properties of perovskites

We investigated the effect of sulfur-functionalized surface on the crystallinity of $MAPbI_3$ perovskite film by X-ray diffraction (XRD), as shown in Figure 3.3 a. From the diffraction spectra, the perovskite films coated on SnO_2 with or without sulfur functionalization exhibit diffraction peaks at 14.1°, 28.2°,31.8° corresponding to (110), (220), (310) facets respectively, which is consistent with main $MAPbI_3$ lattice structure.[24] All XRD peaks based on sulfur-functionalized SnO_2 become narrower, for (110) peak, the full width at half maximum (FWHM) based on sulfur-functionalized SnO_2 (SnO_2/S) is 0.102°, lower than that based on bare SnO_2 ETL (0.122°), indicating the enhanced crystallinity in the presence of sulfur-functionalized ETL, which is in agreement with the enlarged grains from SEM study which will be discussed. Figure 3.3 b demonstrates the transparency of ETL and the ultraviolet-visible (UV-vis) absorption spectroscopy

of perovskite on SnO_2 and SnO_2/S substrates. No significant difference in transmittance spectra was observed in the range of 380~800 nm, an indication of no induced optical losses after sulfur-functionalized SnO_2 surface, which is important to absorption of perovskite layer in order to obtain maximum photocurrent. Meanwhile, absorption of perovskite film on SnO_2/S substrate was increased in 380-550 nm regime, which was related with better perovskite crystallinity.

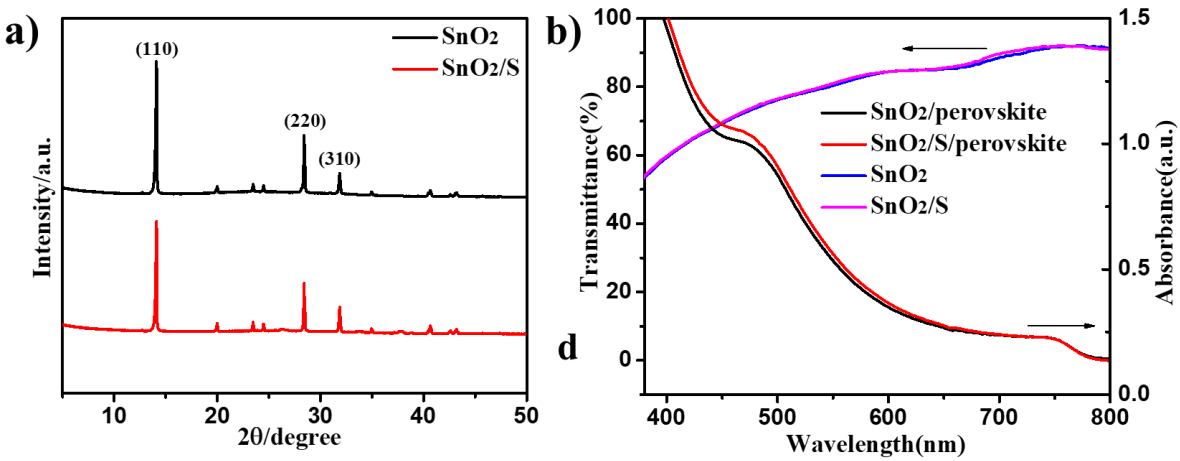

Figure 3.3 a) XRD pattern of perovskite films based on SnO_2 substrates with and without sulfur functionalization. b) Transmittance spectroscopy of SnO_2 and SnO_2/S on ITO glass and absorption spectroscopy of perovskite thin film on SnO_2 and SnO_2/S ETL.

Besides, the interface sulfur functionalization influenced the crystallinity process during the annealing. substrates surface optimization is beneficial for the perovskite nucleation and crystal growth.[10] To assess the impact of sulfur on SnO2 surface on the perovskite film quality, $MAPbI_3$ perovskite films on SnO_2 with or without sulfur functionalization were studied by scanning electron microscopy (SEM), Figure 3.4 shows the SEM images of perovskite films on SnO_2 ETL with 1, 3 and 5 times xanthate treatment and the corresponding size histograms, in all case of xanthate treatment, the perovskite grains sizes are relatively bigger compared with that without sulfur functionalization, which may originates from formed Sn-S-Pb chemical interaction, which

is favorable for perovskite crystal growth. Presumably adjusted surface energy resulted from changed interaction contributed to the improved nucleation and crystal growth,[9] finally leading to uniform surface and larger grains size. However, the presence of pin-holes (marked in red circle) in perovskite film could be seen on sample with 5 times xanthate treatment, which may be ascribed to excess sulfur amount with more than monolayer on SnO_2 ETL which is detrimental to rapid and homogeneous nucleation.

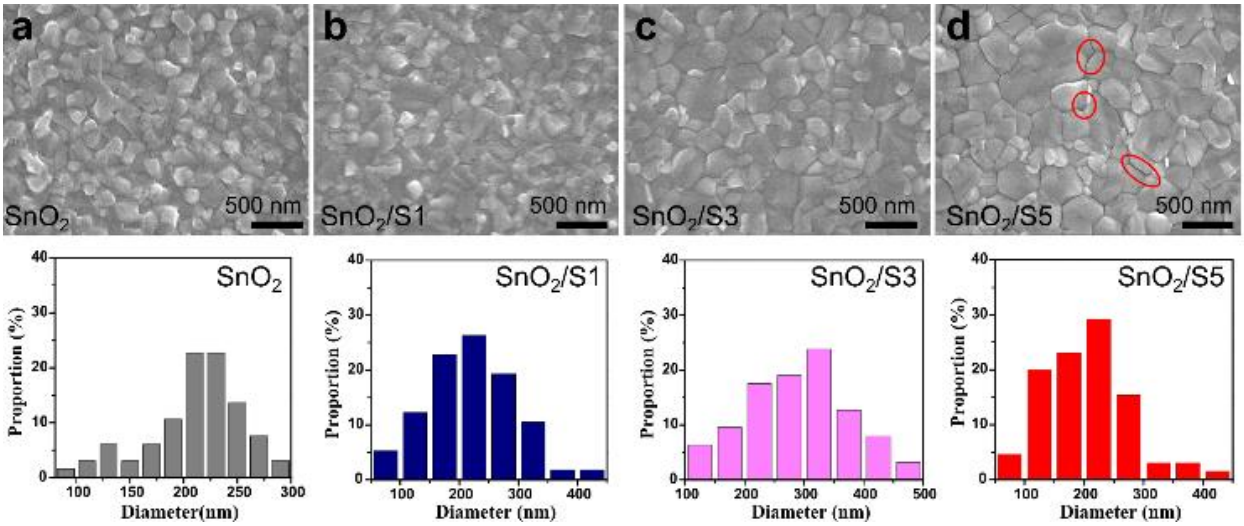

Figure 3.4 SEM images of $MAPbI_3$ perovskite films based on a) SnO_2, b) SnO_2/S1, c) SnO_2/S3, d) SnO_2/S5. Column graphs of perovskite grain size statistics are shown below correspondingly.

3.3.3 Photovoltaic performance of perovskite solar cells

Normal structure perovskite solar cells having the following configuration of indium tin oxide (ITO)/SnO_2/$CH_3NH_3PbI_3$ ($MAPbI_3$)/Spiro-OMeTAD/Au were fabricated under ambient atmosphere at more than 60% RH and the corresponding the photocurrent density-voltage (J-V) characteristics based on SnO_2 substrate with different xanthate treatment times is shown in Figure 3.5. The detailed result for the different device parameters are summarized in Table 3.2. The control device based on untreated-SnO_2 ETL shows efficiency of 16.56% with Jsc of 21.74 mA

cm^{-2}, Voc of 1.03 and FF of 73.65%. The solar cell efficiencies increased significantly with 1 and 3 times xanthate treatment (denoted as SnO_2/S1 and SnO_2/S3 respectively). The best performing solar cell was achieved with device fabricated with SnO_2/S3 at high humidity condition with efficiency of 18.41%, Jsc of 22.61 mA cm^{-2}, Voc of 1.06 and FF of 76.85%. However, the device performance SnO_2/S5 decreased significantly.

Figure 3.5 b demonstrates the performance J-V characteristics of perovskite device based on SnO_2 and SnO_2/S at forward and reverse scan directions. It can be noted that hysteresis was reduced evidently upon sulfur functionalization, to quantify the hysteresis variation in the solar cells, hysteresis index (HI) was calculated.[25-26] HI value decreases from 0.221 based on SnO_2 ETL to 0.054 based on SnO_2/S ETL, notably, the hysteresis behavior was suppressed dramatically, which can be ascribed to the suppressed surface trapping due to better quality of perovskite film and better interfacial interaction contributing to efficient electron injection into ETL.[27-28] Under the optimized sulfur-functionalized ETL condition, current density of perovskite solar cell enhanced from 21.74 mA cm^{-2} to 22.61 mA cm^{-2}, which agrees with the integrated current densities without (21.22 mA cm^{-2}) and with (22.09 mA cm^{-2}) sulfur functionalization on ETL respectively (Figure 3.5 c) as calculated from the external quantum efficiency measurement. We conducted the steady-state output power of perovskite solar cells under continuous AM 1.5G illumination with and without sulfur functionalization, as shown in Figure 3.5 d, the efficiency of about 18.0% was obtained for sulfur functionalization at 0.90V, however, initial efficiency of about 16.3% gradually decreased. Importantly, the device after sulfur functionalization shows better stability compared to that without sulfur functionalization.

Table 3.2 Best performing efficiency of perovskite based on bare SnO_2 ETL (denoted as SnO_2/S0) and sulfur-functionalized SnO_2 ETL with 1, 3, and 5 times xanthate treatment, which correspond to SnO_2/S1, SnO_2/S3, and SnO_2/S5 respectively.

PSCs	Jsc (mA cm^{-2})	Voc (V)	FF (%)	PCE (%)
SnO_2/S0	21.74	1.03	73.65	16.56
SnO_2/S1	22.55	1.02	75.20	17.38
SnO_2/S3	22.61	1.06	76.85	18.41
SnO_2/S5	21.18	1.02	69.22	14.98

To further investigative the origin of enhanced perovskite efficiency and the interfacial carrier transport, steady-state photoluminescence (PL) spectroscopy of perovskite films on SnO_2 or SnO_2/S substrate was measured, and the result is shown in Figure 3.6 a. A strongly quenched PL upon different times of sulfur-functionalized SnO_2 substrate was observed, indicative of efficient electron transfer in the presence of sulfur. Besides, perovskite film on SnO_2/S substrate displayed a blue-shift PL peak compared to that on SnO_2 substrate, indicating the efficient traps passivation at the ETL/the perovskite interface, [29] presumably due to the interaction between sulfur atoms and uncoordinated Pb^{2+}, contributing to efficient surface passivation of perovskite We further measured time-resolved PL to analyze the charge transport kinetics as shown in Figure 3.6 b. The decay curves of perovskite on SnO_2 or SnO_2/S substrates are fitted with bi-exponential components, where the fast (τ_1) decay is mainly correlated to interfacial charge transfer, and the slow (τ_2) decay was caused by radiative emissions of the bulk perovskite film involving trap-assisted recombination.[14] The fast decay (τ_1) of the perovskite decreased from 15.5 ns to 10.3 ns

upon sulfur functionalization, indicating a more rapid interfacial electron transfer from perovskite to ETL. The slow decay (τ_2) constant decreased from 138.9 ns to 63.8 ns, which is ascribed to

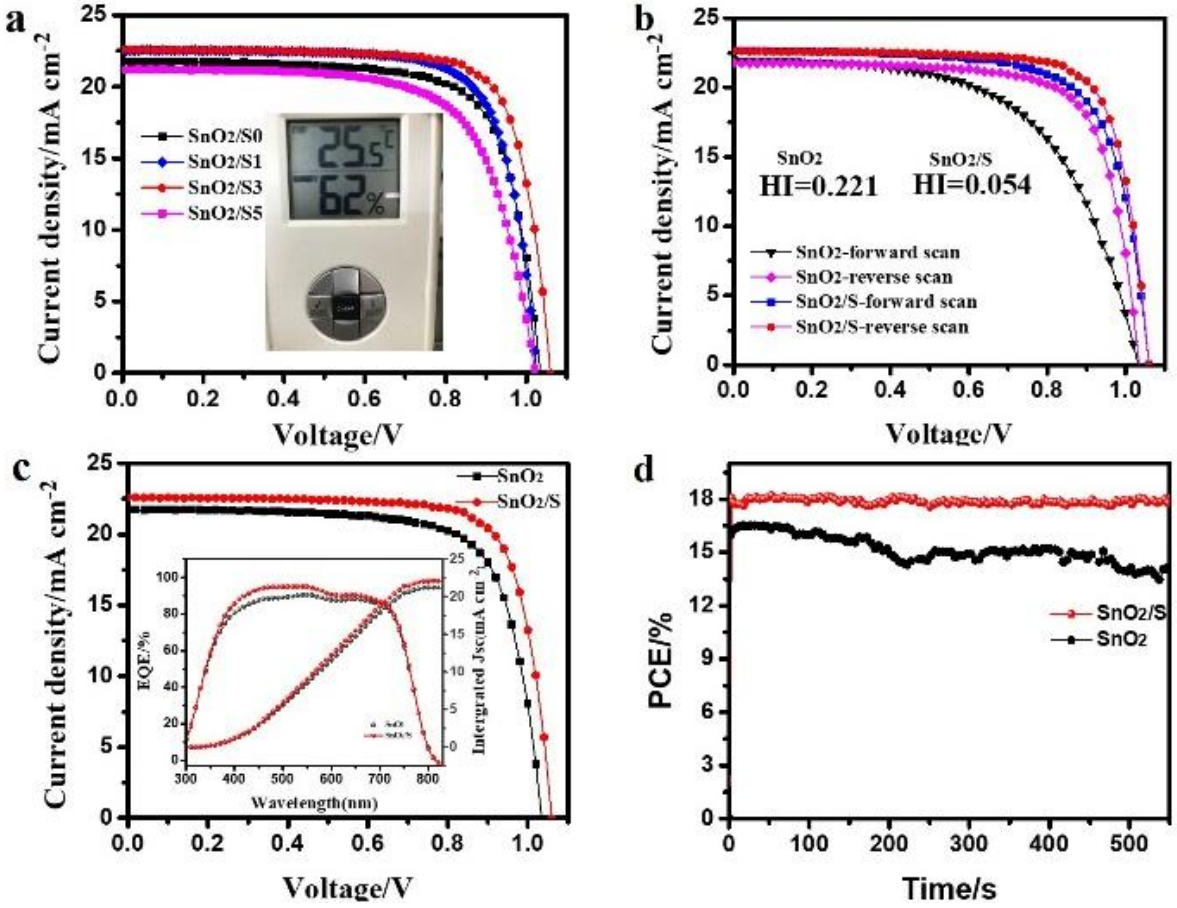

Figure 3.5 a) current density-voltage characteristics of best performing device based on SnO_2 without and with 1, 3, 5 times sulfur functionalization (xanthate treatment). Inset was humidity condition of device fabrication. b) Comparison of current density-voltage on SnO_2 and sulfur-functionalized SnO_2 measured by forward and reverse scan, inset text shows the calculated hysteresis index (HI). c) Compared current density-voltage of best performing perovskite solar cells with and without sulfur functionalization. Inset shows the IPCE spectra of corresponding devices. d) Steady output power of perovskite solar cells with and without sulfur functionalization.

reduced defect-assisted Shockley-Read-Hall recombination in the high quality perovskite with enlarged grain size.[14, 30] The surface passivation and suppressed recombination in perovskite bulk

all contributed to decreased carrier losses and enhanced perovskite device performance.[31]

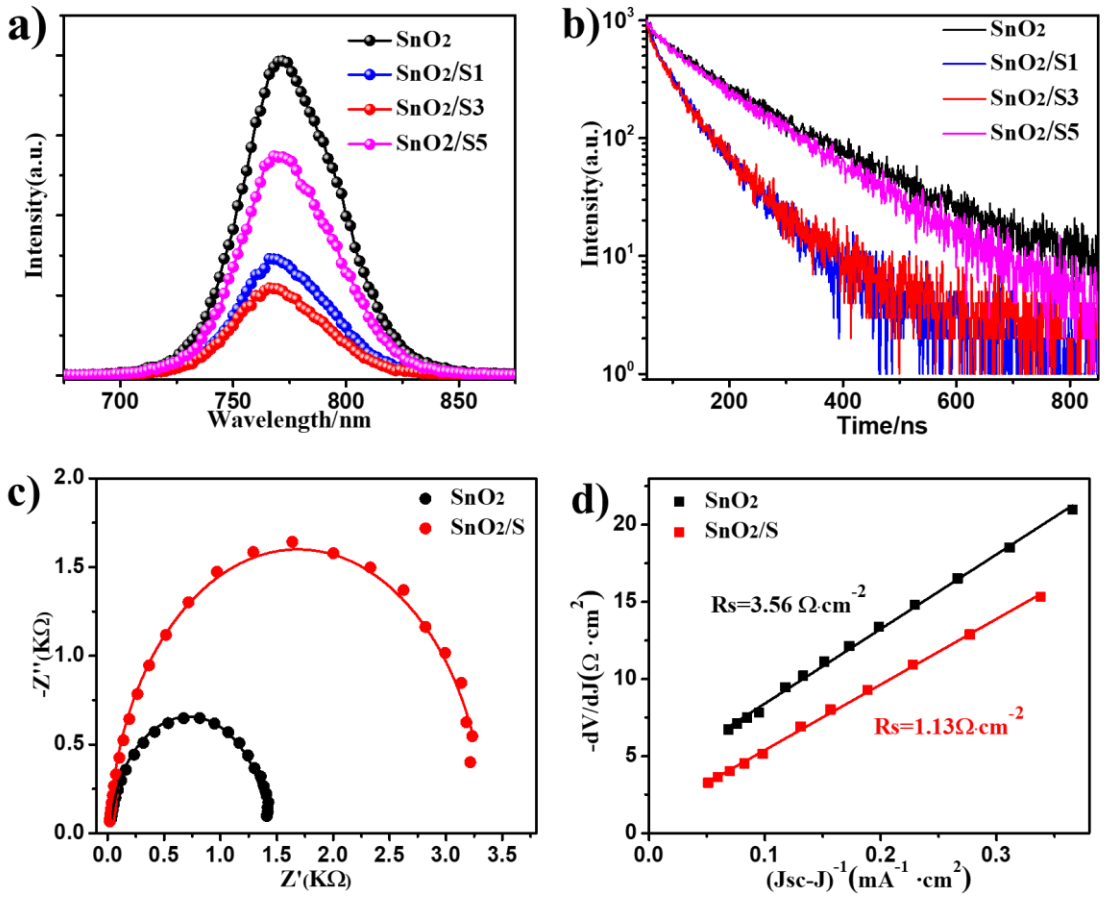

Figure 3.6 a) steady-state photoluminescence (PL) spectra of perovskite film on SnO_2 or sulfur-functionalized SnO_2 with different xanthate treatment. b) Time-resolved photoluminescence of perovskite based on SnO_2 or sulfur-functionalized SnO_2 with different xanthate treatment. c) Nyquist plots of $MAPbI_3$ perovskite solar cells with fitting results under equivalent circuit model. d) Plots of $-dV/dJ$ vs $(Jsc-J)^{-1}$ and linear fitting of perovskite solar cells with and without sulfur functionalization.

We further measured electrochemical impedance spectroscopy (EIS) of perovskite device to characterize the charge transfer and carrier recombination. A 0.6V bias was applied to examine the perovskite solar cells with and without interfacial sulfur functionalization. We extracted the recombination resistance (R_{rec}) and series resistance (R_s) based on the equivalent circuit model. Figure 3.6 c shows the Nyquist plots with diacritical characteristic arcs with and without sulfur functionalization, the decreased R_s (19.19 Ω) as compared with that of control perovskite (27.32 Ω) was observed, agreement with the faster charge transfer at the interface of SnO_2 and perovskite. Furthermore, the Rrec increased from 1386 Ω to 3335 Ω upon the sulfur functionalization on SnO_2 ETL, which is attributed to the suppressed recombination in perovskite device after introduction of sulfur at the interface. These results indeed confirm that the presence of sulfur at the interface contributed to a more efficient charge transfer injection and at the same time mitigated the non-radiative recombination process. To understand the effect of sulfur functionalization in solar cell, Figure 3.6 d compares the plots of –dV/dJ vs $(Jsc-J)^{-1}$ extracted from the dark J-V curve to analyze the series resistance (R_s) and ideality factor (n) by fitting the dark current according to the Equation 1.[32-33]

$$-\frac{\mathrm{dV}}{\mathrm{dJ}} = \frac{nKT}{q}(Jsc - J)^{-1} + Rs \qquad (1)$$

The decreased value of ideality factor from 1.87 to 1.64 confirms the suppressed recombination at the interface after interfacial sulfur functionalization.[34] It has been reported that lower Rs demonstrates that at high bias voltage, the carrier loss is suppressed.[33]

Thermally stimulated current (TSC) allows for the investigation of semiconducting materials on electronic traps. Firstly perovskite film was cooled to a low temperature below the activation energy of electronic trap states, at which point upon by light illumination, the charge

carriers filled the trap sites and subsequently, charge carriers in the trap sites of perovskite were gradually released when the sample was heated up to 370K at a constant rate, during which current was generated inside the perovskite, the Arrhenius plot of TSC spectra is shown in Figure S8.Trap density distribution in perovskite bandgaps shown in Figure 3.7 a. The vacuum level was calculated according the following Equation 2[35-36] supposing the perovskite conduction band of MAPbI3 perovskite is -3.9.

$$\text{Evac} = -3.9 - \text{KT}ln\frac{T^4}{\beta} \qquad (2)$$

β is the heating rate applied in TSC measurement. For the perovskite based on SnO_2 ETL, the distribution of electron trap density increased as the vacuum level shifted into deep vacuum level state, and at the same time there exists a distinct peak at around -4.65 eV. After the sulfur functionalization, the electron trap density at the shallower energy level decreased significantly, the trap density from -4.1 eV to -4.65 eV decreased, the trap density was found to be nearly 2 order orders of magnitude lower than that of pristine perovskite at about -4.3 eV from the vacuum level. This decreased trap density in shallow area is favorable for the perovskite device performance [37] and improves the carrier transport properties. [38-39]

Ambient stability of perovskite solar cells without sealing was investigated, where perovskite solar cells after treatment with xanthate exhibited good stability retaining almost 90% of initial PCE after 70 days in desiccator, as shown in Figure 3.7 b, compared to the solar cell fabricated on bare SnO_2 which degraded below 50% of its initial performance. This can be attributed to the high sensitivity of perovskite film to moisture especially in the case of poor quality of perovskite film, leading to dramatic loss in voltage and FF. In addition, sulfur atoms coordinated with Pb^{2+} near the perovskite surface exhibited increased electrostatic interaction with perovskite

structure due to its higher valence anionic charge, which is responsible for prohibiting the moisture invasion at the interface and the long-term stability.[40-41]

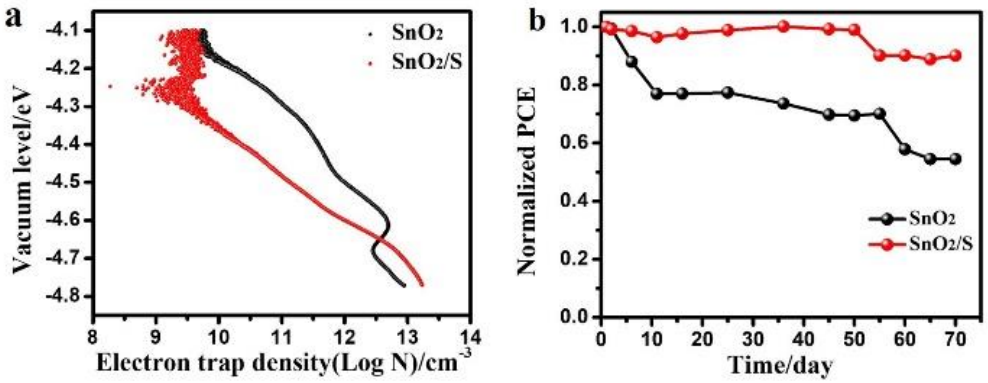

Figure 3.7 a) Vacuum level of perovskite as function of trap density, trap density distribution of perovskite before and after sulfur functionalization on SnO_2 ETL. b) Performance stability of the reference cell and modified perovskite solar cells without encapsulation kept in a dry box at room temperature.

3.4 Conclusions

In summary, we demonstrated facile interfacial sulfur functionalization by xanthate decomposition on SnO_2 ETL. Sulfur atoms at the interface can coordinate with Pb^{2+} in perovskite and passivate perovskite surface, which is favorable for perovskite crystal growth, leading to better surface morphology and enhanced crystallinity with larger perovskite grain size as revealed by SEM and XRD. Additionally, TSC measurement shows the decreased trap density in shallow trap area. Despite the device fabrication process in the relative high humidity, the perovskite solar cells prepared using the modified SnO_2 showed improved efficiency from 16.5% to 18.4% with suppressed hysteresis behavior, which originates from accelerated charge transfer at SnO_2/perovskite interface as revealed by PL study and IS. Considerable retardation of solar cell

degradation was achieved by the interfacial sulfur functionalization, retaining almost 90% of its initial efficiency after 70d storage due to increased electrostatic interaction between sulfur and perovskite. We believe that facile sulfur functionalization at the interface provides an opportunity for improving efficiency, stability of these materials.

References

[1] A. Kojima, K. Teshima, Y. Shirai, T. Miyasaka, *Journal of the American Chemical Society* **2009**, 131, 6050.

[2] W. S. Yang, B.-W. Park, E. H. Jung, N. J. Jeon, Y. C. Kim, D. U. Lee, S. S. Shin, J. Seo, E. K. Kim, J. H. Noh, *Science* **2017**, 356, 1376.

[3] Y. K. Wang, Z. C. Yuan, G. Z. Shi, Y. X. Li, Q. Li, F. Hui, B. Q. Sun, Z. Q. Jiang, L. S. Liao, *Advanced Functional Materials* **2016**, 26, 1375.

[4] W. Ke, D. Zhao, C. Xiao, C. Wang, A. J. Cimaroli, C. R. Grice, M. Yang, Z. Li, C.-S. Jiang, M. Al-Jassim, *Journal of Materials Chemistry A* **2016**, 4, 14276.

[5] H. S. Kim, J. Y. Seo, N. G. Park, *Chemsuschem* **2016**, 9, 2528.

[6] Y. Bai, X. Meng, S. Yang, *Advanced Energy Materials* **2018**, 8, 1701883.

[7] W. Tress, N. Marinova, T. Moehl, S. M. Zakeeruddin, M. K. Nazeeruddin, M. Grätzel, *Energy & Environmental Science* **2015**, 8, 995.

[8] Y. Shih, L. Wang, H. Hsieh, K. Lin, *Journal of Materials Chemistry A* **2015**, 3, 9133.

[9] G. Yang, C. Wang, H. Lei, X. Zheng, P. Qin, L. Xiong, X. Zhao, Y. Yan, G. Fang, *Journal of Materials Chemistry A* **2017**, 5, 1658.

[10] L. Zuo, Q. Chen, N. De Marco, Y.-T. Hsieh, H. Chen, P. Sun, S.-Y. Chang, H. Zhao, S. Dong, Y. Yang, *Nano letters* **2016**, 17, 269.

[11] F. Zhang, X. Yang, M. Cheng, W. Wang, L. Sun, *Nano Energy* **2016**, 20, 108.

[12] M. Moriya, D. Hirotani, T. Ohta, Y. Ogomi, Q. Shen, T. S. Ripolles, K. Yoshino, T. Toyoda, T. Minemoto, S. Hayase, *Chemsuschem* **2016**, 9, 2634.

[13] P. L. Qin, G. Yang, Z. w. Ren, S. H. Cheung, S. K. So, L. Chen, J. Hao, J. Hou, G. Li, *Advanced Materials* **2018**, 30, 1706126.

[14] S. You, H. Wang, S. Bi, J. Zhou, L. Qin, X. Qiu, Z. Zhao, Y. Xu, Y. Zhang, X. Shi, *Advanced*

Materials **2018**, 30, 1706924.

[15] D. Bi, *Chemsuschem* **2016**, 10, 1624.

[16] H. Zhou, Q. Chen, G. Li, S. Luo, T.-b. Song, H.-S. Duan, Z. Hong, J. You, Y. Liu, Y. Yang, *Science* **2014**, 345, 542.

[17] L. Zhu, Y. Xu, P. Zhang, J. Shi, Y. Zhao, H. Zhang, J. Wu, Y. Luo, D. Li, Q. Meng, *Journal of Materials Chemistry A* **2017**, 5, 20874.

[18] T. Y. Wen, S. Yang, P. F. Liu, L. J. Tang, H. W. Qiao, X. Chen, X. H. Yang, Y. Hou, H. G. Yang, *Advanced Energy Materials* **2018**, 8, 1703143.

[19] L. Liu, S. Huang, Y. Lu, P. Liu, Y. Zhao, C. Shi, S. Zhang, J. Wu, H. Zhong, M. Sui, *Advanced Materials* **2018**, 1800544.

[20] C. Fei, B. Li, R. Zhang, H. Fu, J. Tian, G. Cao, *Advanced Energy Materials* **2017**, 7.

[21] H. Zhu, F. Zhang, Y. Xiao, S. Wang, X. Li, *Journal of Materials Chemistry A* **2018**, 6, 4971.

[22] M. Al-Shakban, Z. Xie, N. Savjani, M. A. Malik, P. O'Brien, *Journal of Materials Science* **2016**, 51, 6166.

[23] C. Goh, S. R. Scully, M. D. McGehee, *Journal of Applied Physics* **2007**, 101, 114503.

[24] K. M. Lee, M. Y. Hou, V. Suryanarayanan, M. C. Wu, *Chemsuschem* **2018**.

[25] J. Cao, Y.-M. Liu, X. Jing, J. Yin, J. Li, B. Xu, Y.-Z. Tan, N. Zheng, *Journal of the American Chemical Society* **2015**, 137, 10914.

[26] S. You, S. Bi, J. Huang, Q. Jia, Y. Yuan, Y. Xia, Z. Xiao, Z. Sun, J. Liu, S. Sun, *Chemistry-A European Journal* **2017**, 23, 18140.

[27] A. Guerrero, A. Bou, G. Matt, O. Almora, T. Heumüller, G. Garcia-Belmonte, J. Bisquert, Y. Hou, C. Brabec, *Advanced Energy Materials* **2018**, 1703376.

[28] S. Ravishankar, O. Almora, C. Echeverría-Arrondo, E. Ghahremanirad, C. Aranda, A. Guerrero, F. Fabregat-Santiago, A. Zaban, G. Garcia-Belmonte, J. Bisquert, *The Journal of Physical Chemistry Letters* **2017**, 8, 915.

[29] C. Sun, Z. Wu, H. L. Yip, H. Zhang, X. F. Jiang, Q. Xue, Z. Hu, Z. Hu, Y. Shen, M. Wang, *Advanced Energy Materials* **2016**, 6.

[30] W. Tress, J. P. Correa Baena, M. Saliba, A. Abate, M. Graetzel, *Advanced Energy Materials* **2016**, 6.

[31] M. Li, Z. K. Wang, Y. G. Yang, Y. Hu, S. L. Feng, J. M. Wang, X. Y. Gao, L. S. Liao, *Advanced Energy Materials* **2016**, 6.

[32] Q. Dong, Y. Shi, K. Wang, Y. Li, S. Wang, H. Zhang, Y. Xing, Y. Du, X. Bai, T. Ma, *The Journal of Physical Chemistry C* **2015**, 119, 10212.

[33] X. Zhao, L. Tao, H. Li, W. Huang, P. Sun, J. Liu, S. Liu, Q. Sun, Z. Cui, L. Sun, *Nano letters* **2018**, 18, 2442.

[34] P. Liao, X. Zhao, G. Li, Y. Shen, M. Wang, *Nano-Micro Letters* **2018**, 10, 5.

[35] Z. Fang, L. Shan, T. Schlesinger, A. Milnes, *Materials Science and Engineering: B* **1990**, 5, 397.

[36] J. Schafferhans, C. Deibel, V. Dyakonov, *Advanced Energy Materials* **2011**, 1, 655.

[37] Y. Ogomi, A. Morita, S. Tsukamoto, T. Saitho, Q. Shen, T. Toyoda, K. Yoshino, S. S. Pandey, T. Ma, S. Hayase, *The Journal of Physical Chemistry C* **2014**, 118, 16651.

[38] G. Xing, N. Mathews, S. Sun, S. S. Lim, Y. M. Lam, M. Grätzel, S. Mhaisalkar, T. C. Sum, *Science* **2013**, 342, 344.

[39] S. D. Stranks, G. E. Eperon, G. Grancini, C. Menelaou, M. J. Alcocer, T. Leijtens, L. M. Herz, A. Petrozza, H. J. Snaith, *Science* **2013**, 342, 341.

[40] J. Gong, M. Yang, D. Rebollar, J. Rucinski, Z. Liveris, K. Zhu, T. Xu, *Advanced Materials* **2018**, 1800973.

[41] J. Gong, M. Yang, X. Ma, R. D. Schaller, G. Liu, L. Kong, Y. Yang, M. C. Beard, M. Lesslie, Y. Dai, *The journal of physical chemistry letters* **2016**, 7, 2879.

Chapter 4. Passivation of grain boundary by squaraine zwitterions for efficient and stable perovskite solar cells

4.1 Introduction

A recent study has clearly shown that $CH_3NH_3PbI_3$ ($MAPbI_3$) single crystals without grain boundary (GBs) and low surface defects exhibited much enhanced stability. [1-2] Unwanted defects in polycrystalline perovskite films along GBs could create pin-hole and nonradiative recombination center, defects-induced GBs create a convenient diffusion passage for oxygen and moisture in perovskite films, which accelerate performance degradation and hamper the stability of the photovoltaic device. The low formation energy of organometal halide perovskite and the tendency of the organic components to decompose during the annealing process results in the formation of vacancies defects which would eventually become the nonradiative recombination centers.[3-4] The presence of functional group such as carboxyl (-COOH),[5] amino group[6], which can coordinate with Pb is an important criterion in selecting a molecule as the passivation materials, these materials can interact with Pb to form passivator-PbI_2 adduct, bridging the neighboring crystal grains and influencing the film crystallization process.[7-9] These efficient defect passivation of the perovskite layer is achieved to date leave much room for further improvement. Therefore, selection of a well-designed and suitable materials to passivate perovskite film is of utmost requirement.

Squaraine (SQ) zwitterions exhibit high absorption coefficient with tunable bandgaps, excellent photochemical and thermal stabilities,[10] These functional molecules exhibit substantial bond delocalization and donor-acceptor architecture with notably electron-deficient four-membered ring[11] Herein, three different p-type SQ zwitterions functionalized with bromide or

fluoride (SQ45, SQ63 and SQ81) were designed and synthesized by a simple and cost-effective approach for perovskite films GBs passivation. SQ molecules could enhance charge separation at the perovskite grain/SQ interface due to the fact that the highest occupied molecular orbital (HOMO) of SQ molecules aligned well with valence band (VB) of $MAPbI_3$ perovskite. Additionally, we employed thermally stimulated current (TSC) measurement to study the effect of the SQ passivation on the traps distribution in $MAPbI_3$ perovskite. The efficiency of SQ63 passivated perovskite solar cells was improved up to 18.83%. This strategy also enhanced the stability of perovskite devices, in which 90% of initial performance was still retained after 600 h storage.

4.2 Experimental

4.2.1 Preparation of perovskite solar cells

ITO-coated glass substrates were patterned by etching with zinc powder and HCl solution, then substrates were sequentially sonicated with distilled water, ethanol, acetone, water for 15minutes in each solvent. Diluted SnO_2 colloid precursor (2.67% in water) was spin-coated on glass/ITO after 15 min UV-O_3 treatment at 2000rpm for 30s, which is followed by annealing in ambient air at 150^{o}C for 30min. MAPbI3 perovskite precursor solution was prepared by dissolving MAI (1.5M) and PbI_2 (1.5M) in mixed solvent DMF:DMSO (4:1). 100 µL of the precursor solution was spin-coated on ITO/SnO2 substrate at 4000 rpm for 25s under about in air at 60% RH condition. 0.5 ml of ethyl acetate (EA) with or without SQ45,SQ63 and SQ81 molecules was quickly dropped on the spinning SnO_2 substrate, followed by annealing on a hot plate at 100 ^{o}C for 10min. Spiro-OMeTAD in chlorobenzene (72mg/ml) was spin-coated on ITO/SnO_2/ perovskite substrate (4000rpm for 30s) after cooling down to room temperature. Spiro-OMeTAD

was prepared with the following additives, 17.5 μL lithium bis(trifluoromethane)sulfonimidate (Li-TFSI) in acetonitrile (520 mg/ml) and 28.8 μL 4-tertbutylpyridine. Finally, 80nm gold was deposited by thermal evaporation onto the spiro-OMeTAD layer.

4.2.2 Characterization

The current density-voltage characteristics of solar cells were measured under AM 1.5G simulated solar illumination. The external quantum efficiencies were measured by illuminating solar cells under monochromatic light from 900nm to 300nm (300W Xenon lamp with a monochromator, Newport 74010). Morphology of perovskite film was characterized by SEM (HITACHI S4800). XRD pattern was analyzed by D8 X-ray diffractometer, using Cu Kα radiation. Fourier Transform Infrared Spectroscopy (FTIR) measurement was performed by JASCO FTIR 4100 for samples in transmission mode. Reflective FTIR for thin film samples was measured using ATR PRO400-S mode. The steady-state photoluminescence (PL) and time-resolved PL measurement were conducted by the Fluorolog-3-p spectrophotometer by the excitation light. Electrochemical impedance spectra were measured by an electrochemical workstation (Parstat 2273, Princeton) under 0.6V positive bias. Thermally stimulated current (TSC) was performed using TS-FETT electron trapping measuring system (Rigaku).

4.2.3 Theoretical calculation

The theoretical molecular orbital calculation was performed using the Time-dependent Density functional Theory program under G09 program package. The squaraine only structure as well the squaraine with the incorporated lead iodide (PbI_2) were programmed for the theoretical calculation. For the squaraine zwitterions alone, the Linear Spin density Approximation was used (LSDA) which uses the Slater exchange functional and the correlation function for its implication

and the basis set 6-311G was employed. It can be clearly visualized that the computed structure of the SQ alone has the Self Consistent Field (SCF) electron density more concentrated on the oxygen of the central squaric acid moiety. Also, the Mullikan charge distribution was found to be -0.381 on that particular oxygen. On the other hand, the approximation B3LYP and the basis set LANL2DZ was implemented when the PbI2 molecule was introduced to the structure of the SQ zwitterions. B3LYP approximation holds good and reliable in terms of enthalpies of formation. The final SQ-PbI_2 complex showed the bond formation between the central core oxygen and metal Pb as given by the increase in the bond length of the carbon and oxygen, which is expected to coordinate with the Pb. The electron density computed by the SCF on the central oxygen Moreover, the Mulliken Charge of on it is found to increase from 0.381 to 0.460, which can be clearly understood by the electronegativity of oxygen on bonding to Pb. Therefore, the theory proves the bond formation between the central oxygen and the Pb.

4.3 Results and discussion

4.3.1 Theoretical calculation and squaraine passivation

In order to confirm the passivation of squaraine (SQ) on perovskite, we performed the density functional theory (DFT) to examine the interaction of SQ and PbI_2. Figure 4.1 a shows calculated interaction between SQ and PbI_2, the optimized geometry demonstrates the interaction of one PbI_2 and squaraine group in SQ63, showing that C=O bond length with PbI_2 interaction (1.28 Å) is slightly longer than that of another C=O bond length (1.24 Å) without PbI_2 interaction. To further visualize the final interaction between SQ63 and two PbI_2, the charge distribution of the optimized geometry before and after coordination is shown in Figure 4.1 b. The electron density of oxygen in SQ63 and SQ63-PbI_2 complex was found to be -0.385 and -0.460

respectively, which can be clearly understood by the increased electronegativity of oxygen after bonding with Pb, resulting in higher electron density in oxygen atoms for the interaction with Pb. We also found that the electron density in cyclobutene ring decreased, drawing the polarizable π electrons from cyclobutene ring due to the Pb coordination with oxygen atoms. We then mapped the electrostatic potential on the SQ63 molecule surface (Figure 4.1 c), PbI_2 coordination draws C=O delocalized electrons from cyclobutene ring and neutralized electrons on O atoms due to the Pb-O bond formation, leading to continues charge distribution at SQ63-PbI_2 junction. According to the calculation, symmetrical squaraine group could interact with PbI_2 strongly, which is expected to passivate defects and reduce trap density on perovskite GBs.

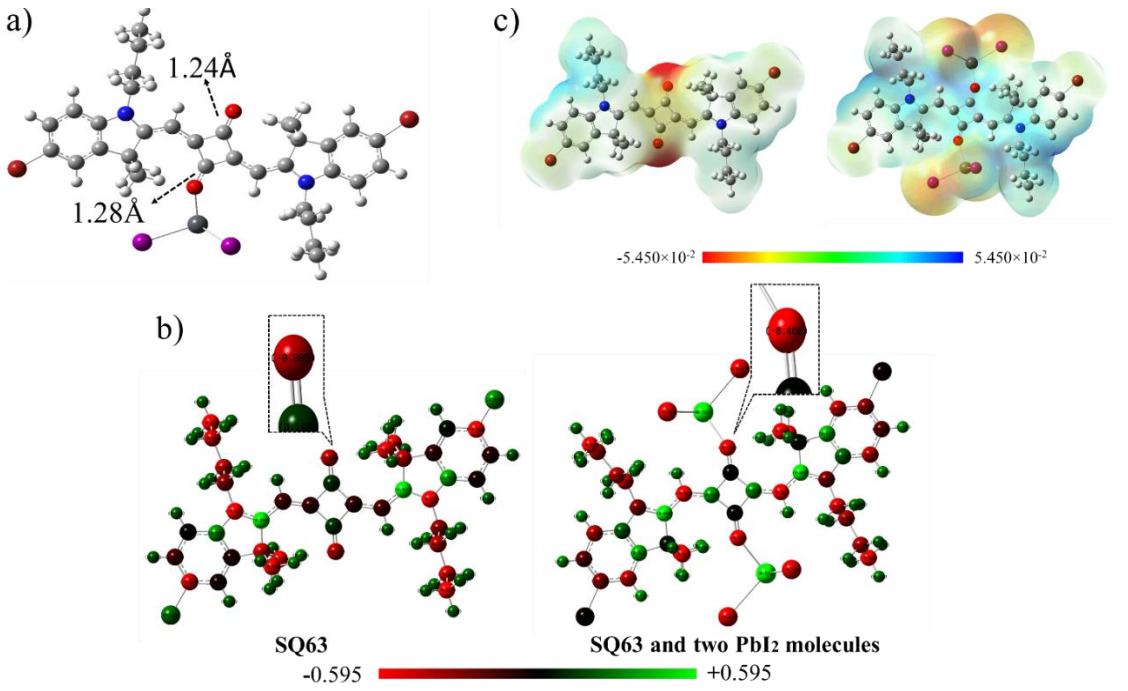

Figure 4.1 a) DFT calculation for an optimized geometry of coordination between SQ63 and one PbI_2. b) The charge distribution of SQ63 and SQ63-two PbI_2 complex after DFT calculation for optimized configuration. The electron density of SQ63 and SQ63-PbI_2 are -0.385 and -0.460 respectively. c) Electrostatic potential mesh maps of SQ63 (left) and SQ63-PbI_2 complex (right).

We characterized SQ passivated $MAPbI_3$ perovskite film using scanning electron microscopy (SEM) and atomic force microscopy (AFM).). Scanning electron microscopy (SEM) images of perovskite films with and without different SQ treatment is shown in Figure 4.2, where the negligible morphological difference was observed with SQ passivation of the perovskite in contrast to the pristine perovskite film, and can be understood due to the extremely low SQ concentration (10^{-3} mg/ml). Interestingly, SQ-passivated perovskite films show smooth morphology compared with the pristine sample as evidenced by atomic force microscopy (AFM). The roughness of films prepared with SQ45, SQ63 and SQ81 passivation were found to be 11.1 nm, 7.8nm and 8.9nm respectively (Figure 4.2) compared to the pristine perovskite (15.4 nm). The roughness of the perovskite surface in the case of SQ passivation decreased due to the fact that SQ molecules with cyclobutene group could coordinate perovskite and further control the crystallization of perovskite. [12]

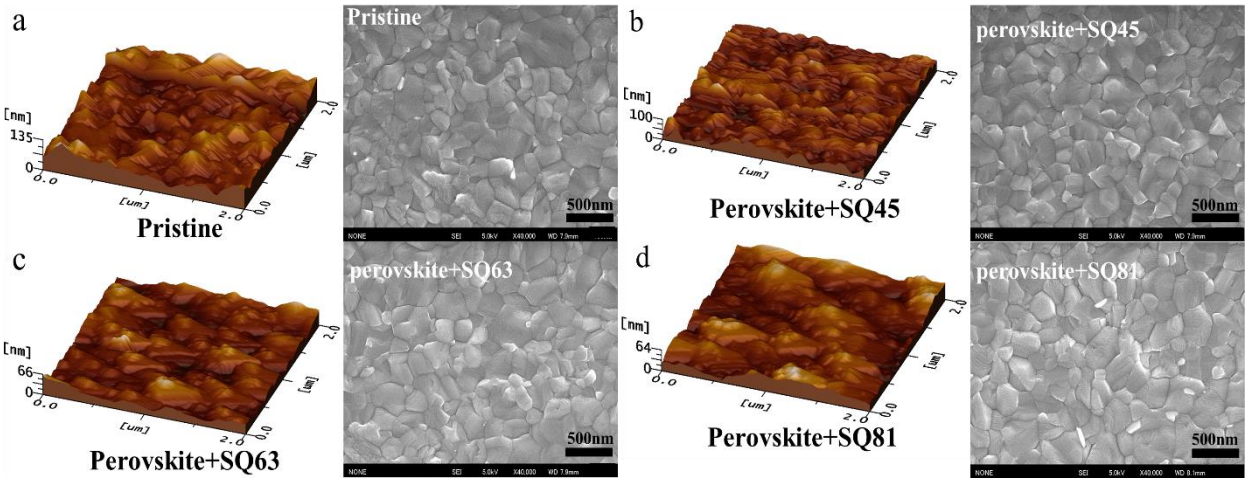

Figure 4.2 Top-view SEM images and AFM 3D graph of a) pristine, b) SQ45-treated, c) SQ63-treated and d) SQ81-treated perovskite films.

It is worth mentioning here that the introduction of the passivator during film preparation process proved to be more effective than mixing in perovskite precursor solution.[13] The

absorbance spectra of the perovskite exhibited nearly identical features, indicating the same light harvesting capability without the influence of SQ molecules (Figure 4.3 a, optimum concentration of 10^{-3} mg/ml). X-ray diffraction (XRD) pattern of perovskite films with and without SQ passivation shows that all XRD pattern of perovskite films exhibit identical diffraction peak at 14.1°, 28.2°, 31.8° corresponding to (110), (220), (310) facets respectively (Figure 4.3 b), which is consistent with the typical main $MAPbI_3$ lattice structure. The diffraction peaks of perovskite film when prepared with SQ molecules were found to be intensified with narrow full width at half maximum (FWHM) of 0.103° (SQ45), 0.101° (SQ63) and 0.106° (SQ81) at (110) peak in comparison to the pristine perovskite (0.128°), indicating that the introduction of SQ molecules in the anti-solvent improved the crystallinity of perovskite films, which can be attributed to the interaction between perovskite and SQ molecules to control perovskite crystal growth during the annealing.

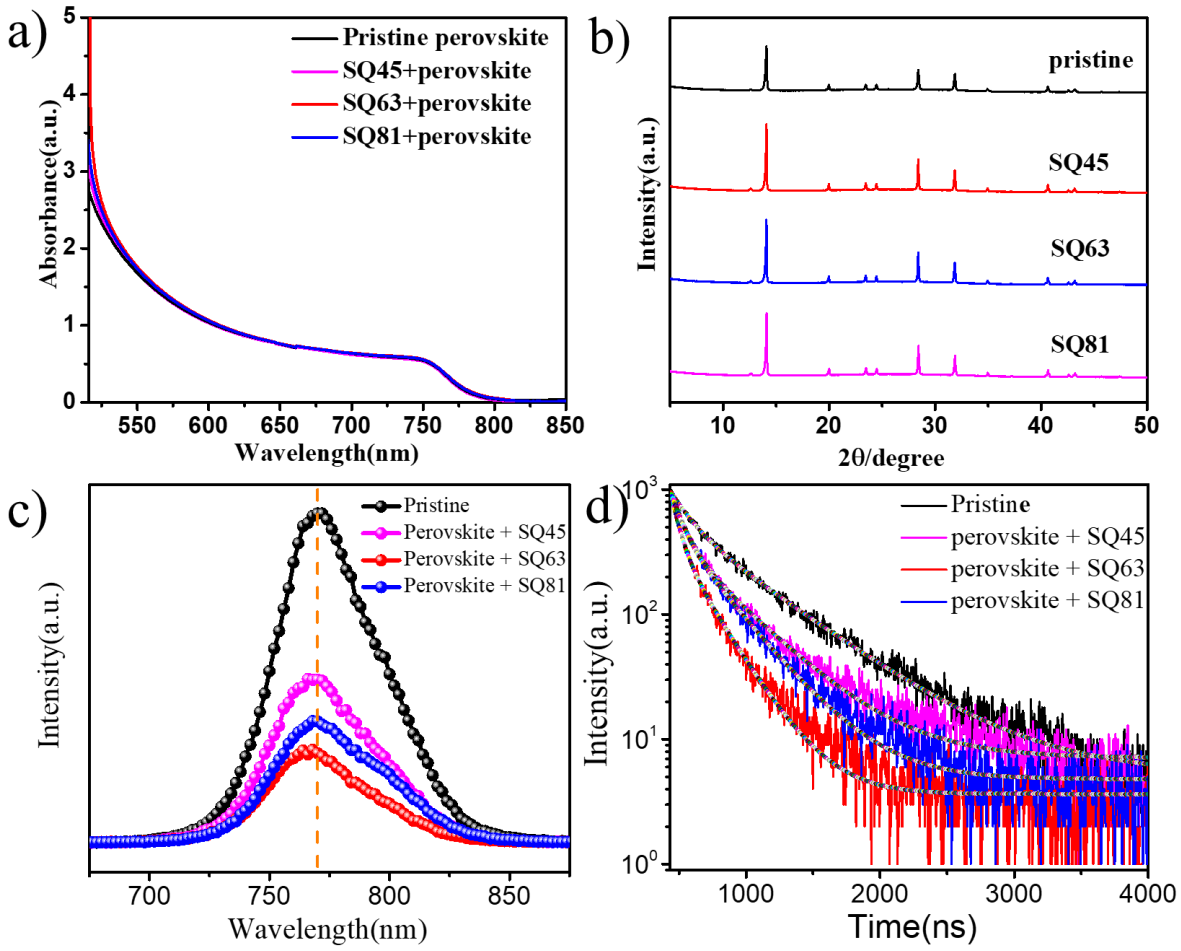

Figure 4.3 a) Absorption spectroscopy of perovskite thin film and b) XRD pattern of perovskite films before and after passivated by SQ45, SQ63 and SQ81 respectively. c) Steady-state photoluminescence (PL) spectra of perovskite film with and without SQ45, SQ63 and SQ81 passivation respectively on glass substrates and the corresponding. d) Time-resolved photoluminescence

It has been demonstrated that the introduction of semiconducting molecules contributed to efficient charge separation and extraction along perovskite GBs.[14] To examine this, steady-state photoluminescence (PL) measurement was performed for the perovskite films with and without SQ passivation as shown in Figure 4.3 c, It can be noted that the PL intensities for SQ45, SQ63 and SQ81-passivated perovskite films were quenched about 50%, 72% and 63% respectively

compared to the reference one, suggesting the suppression of radiative recombination as a result of efficient charge separation at the interface between perovskite grains and SQ molecules, allowing for faster charge transport and collection at external electrode.[15] Additionally, the PL peaks of SQ45, SQ63 and SQ81-passivated perovskite films were blue-shifted to 766nm, 768nm and 768nm compared with the control sample (770nm), indicating effective traps passivation after SQ treatment along the perovskite GBs,[16-17] which agrees well with the assumption that the coordination between lead and squaraine oxygen passivates traps. Time-resolved PL (TRPL) was further performed to evaluate charge extraction between perovskite and SQ molecules as shown in Figure 4.3 d. TRPL curves were fitted with a bi-exponential function, [18] where the fast (τ_1) decay is mainly correlated to charge transfer, and the slow (τ_2) decay is caused by radiative emissions of the bulk perovskite film involving trap-assisted recombination.

4.3.2 Performance of perovskite solar cells

The outstanding effects of interaction between SQ and PbI_2 are expected to improve perovskite solar cell performance and stability, to demonstrate this potential, we fabricated PSCs with the configuration of ITO/SnO_2/$MAPbI_3$ (with and without SQ)/Spiro-OMeTAD/Au in ambient atmosphere with more than 60% RH condition (Figure 4.4 a). The passivated perovskite films were prepared by spin-coating using dripping ethyl acetate (EA) anti-solvent containing SQ45, SQ63 and SQ81 respectively. We have found that the optimum concentration of all three SQ molecules was found to be 10^{-3} mg/ml. The representative current density-voltage (J-V) characteristics of PSCs passivated with different SQ molecules is displayed in Figure 4.4 b, the efficiency of PSCs without SQ passivation was 15.77% with short-circuit current density (Jsc), open-circuit voltage (V_{oc}) and fill factor (FF) of 21.32 mA cm^{-2}, 1.03 V and 71.64% respectively, which is lower than most reported data in the literature since our perovskite fabrication process

was carried in ambient environment with about 60% RH. With the corresponding optimum concentration of SQ45, SQ63 and SQ81 molecules in anti-solvent, the perovskite devices

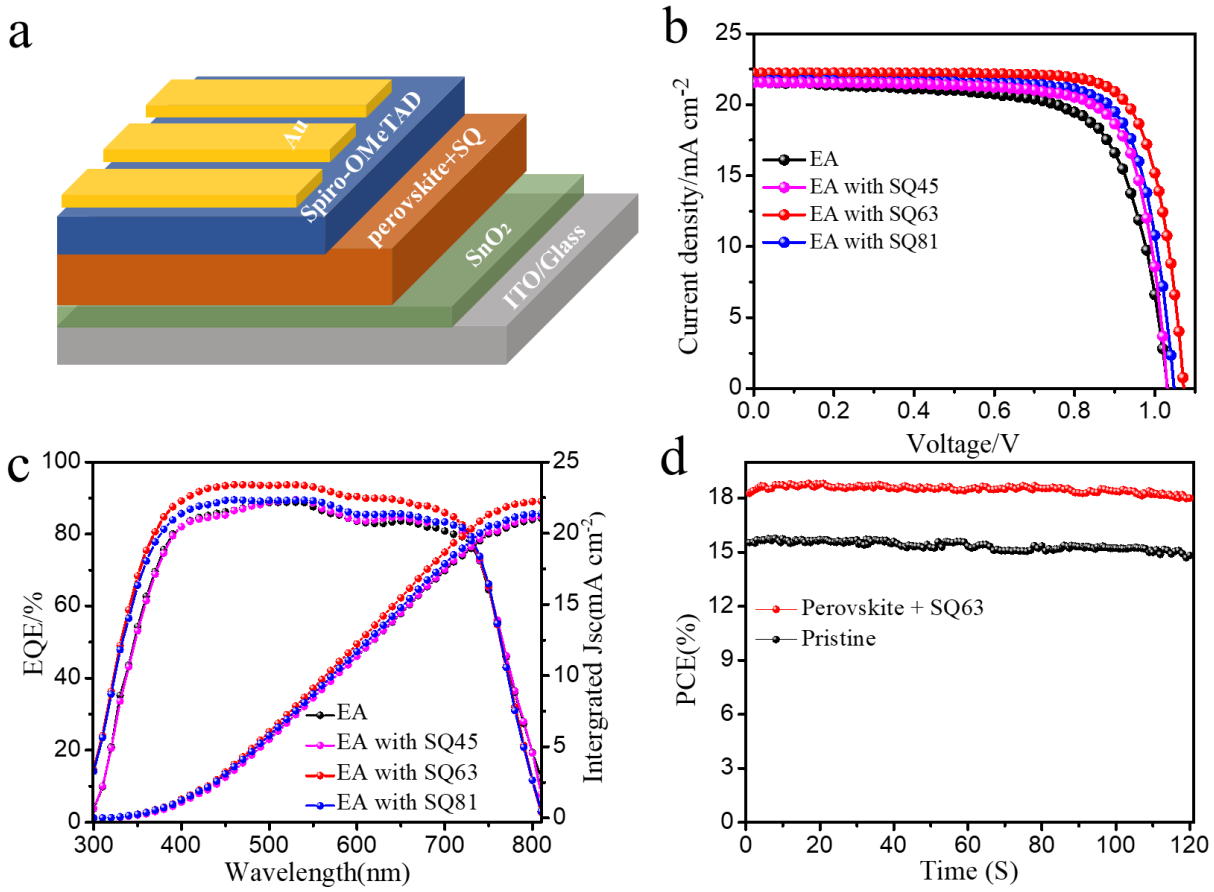

Figure 4.4 a) Schematic diagram of the fabricated PSCs having the structure of ITO/SnO_2/perovskite (with or without SQ)/Spiro-OMeTAD/Au. b) Current density-voltage characteristics of best performing device based on the pristine and SQ45, SQ63, SQ81 passivation dissolved in ethyl acetate (EA) anti-solvent. c) External quantum efficiency (EQE) spectra and integrated Jsc of pristine and SQ-passivated PSCs. d) Steady-state output power of of PSCs based on the pristine and SQ63-passivated PSCs.

Table 4.1 Photovoltaic device parameters for the pristine and SQ45, SQ63, SQ81 passivation under optimum SQ concentration.

	Jsc ($mA\ cm^{-2}$)	Jsc[a] ($mA\ cm^{-2}$)	Voc (V)	FF (%)	PCE (%)
Pristine	21.32	21.04	1.03	71.64	15.77
SQ45	21.55	21.13	1.03	76.83	17.07
SQ63	22.22	22.18	1.07	79.03	18.83
SQ81	21.64	21.32	1.05	77.87	17.66

[a] Calculated current density from the IPCE spectrum

performance based on SQ45, SQ63, and SQ81 passivation showed enhanced efficiency of 17.06%, 18.83% and 17.66% respectively (J-V parameters are given in Table 4.1). All SQ-passivated perovskite devices exhibited higher PCE compared with the pristine sample. All of the photovoltaic parameters are found to be increased for final efficiency increment, current density of PSCs increased from 21.32 mA cm^{-2} for the reference device to 21.55 mA cm^{-2}, 22.22 mA cm^{-2} and 21.64 mA cm^{-2} when the perovskite films were passivated by SQ45, SQ63 and SQ81 respectively, which is in agreement with the integrated current densities calculated from the external quantum efficiency (EQE) measurement (Figure 4.4 c). The FF of SQ63-passivated PSCs was boosted up to nearly 80% compared with the pristine sample (71.64%), which maybe ascribed to efficient charge transfer and reduced traps.[19] The evaluation of the maximum power output of pristine and SQ63-passivated PSCs was carried out under continuous AM 1.5G illumination (Figure 4.4d). SQ63-treated perovskite devices showed a stable efficiency of 18.5% at 0.90 V under continuous illumination. Conversely, the efficiency of about 15.5% for the reference device was observed. From these, we could deduce that SQ45, SQ63 and SQ81 passivation enhanced the

PCE of $MAPbI_3$ perovskite in varying degree, and SQ63 passivation enhanced the efficiency of perovskite by a remarkable of 16%.

4.3.3 Perovskite trap density and stability

Thermally stimulated current (TSC) measurement has been used to quantify the trap density in methylammonium lead iodide perovskite materials.[20] Four different perovskite films-pristine perovskite, SQ45, SQ63 and SQ81 passivated perovskite-were cooled to a low temperature below their respective activation energy of electronic trap states, at which point upon light illumination, the trap sites were filled with charge carriers. Subsequently, charge carriers in the traps were released upon heating up to 350K at a constant rate, during which current was gradually generated inside the pristine or SQ-passivated perovskite films.

Figure 4.5 a showed the TSC spectra of pristine and three SQ-passivated perovskite films. The electrical current is plotted as a function of the temperature for four different perovskite films, supposing all trap sites were all occupied at the starting temperature for simplification, eg., negligible retraping of charge carriers,[42] the number of traps （Nt） should equal the integration of current over time as described in equation 1.

$$\int Idt = qN_t \qquad (1)$$

where q is the elementary charge and I denotes the electrical current generated in perovskite film. As shown in Figure 4.5 a, introduction of three molecules considerably reduced the TSC signal respectively, suggesting the reduction of trap density in perovskite films. We obtained the trap density from the equation above, the trap density significantly decreased from 2.75×10^{17} to 2.55×10^{17}, 4.69×10^{16} and 2.00×10^{17} cm^{-3} for the pristine, SQ45, SQ63 and SQ81 passivated

perovskite respectively. This results proved that squaraine functional group remediates the defects along perovskite GBs, suppressing carrier recombination and thus contributing to increased FF in SQ-treated perovskite devices.[14] Furthermore, SQ63-passivated perovskite exhibited better influence on trap passivation, which is reflected in PSCs performance. In addition, we investigated the impact of SQ molecules treatment on deep traps and shallow traps. Figure 4.5 b shows the trap density distribution in perovskite bandgaps. We calculated the vacuum level of perovskite film according to the following equation 2 supposing the conduction band of $MAPbI_3$ perovskite is -3.93 eV.

$$E_{vac} = -3.93\text{-}KT\ln\frac{T^4}{\beta} \quad (2)$$

where β denotes the heating rate employed in TSC measurement, T is the temperature and K is the Boltzmann constant. After SQ molecules treatment on perovskite films, the electron trap density decreased in perovskite bandgaps from -4.07 eV to -4.77 eV. SQ63 passivation resulted in the reduction of trap density in deep area, which is more than 1 order of magnitude lower than that of the control perovskite between -4.5 eV and -4.77 eV. The deep traps are associated with the structural defects originating from interstitial and antisites defects (Pb-I antisites).[21] Recent study has demonstrated that the deep traps mainly originated from energetically less stable polycrystalline GBs,[22] this considerable decreased trap density in deep area maybe arises from the more efficient passivation using SQ63 functionalized with bromide on perovskite GBs, leading to decreased interstitial or Pb-I antisite defects inside the perovskite film which has been verified by DFT calculation.[23-24] So we confirmed that SQ63 was a more effective material to passivate GBs and surface of perovskite films compared with that of SQ45 and SQ81 passivation. It has also suggested that the hydrogen bonding interaction between MA^+ and aromatic moiety or bromide

restricted organic anion from migration. [25] These results indeed confirmed that SQ molecules on perovskite GBs contributed to a more efficient charge injection and at the same time mitigated the non-radiative recombination process.

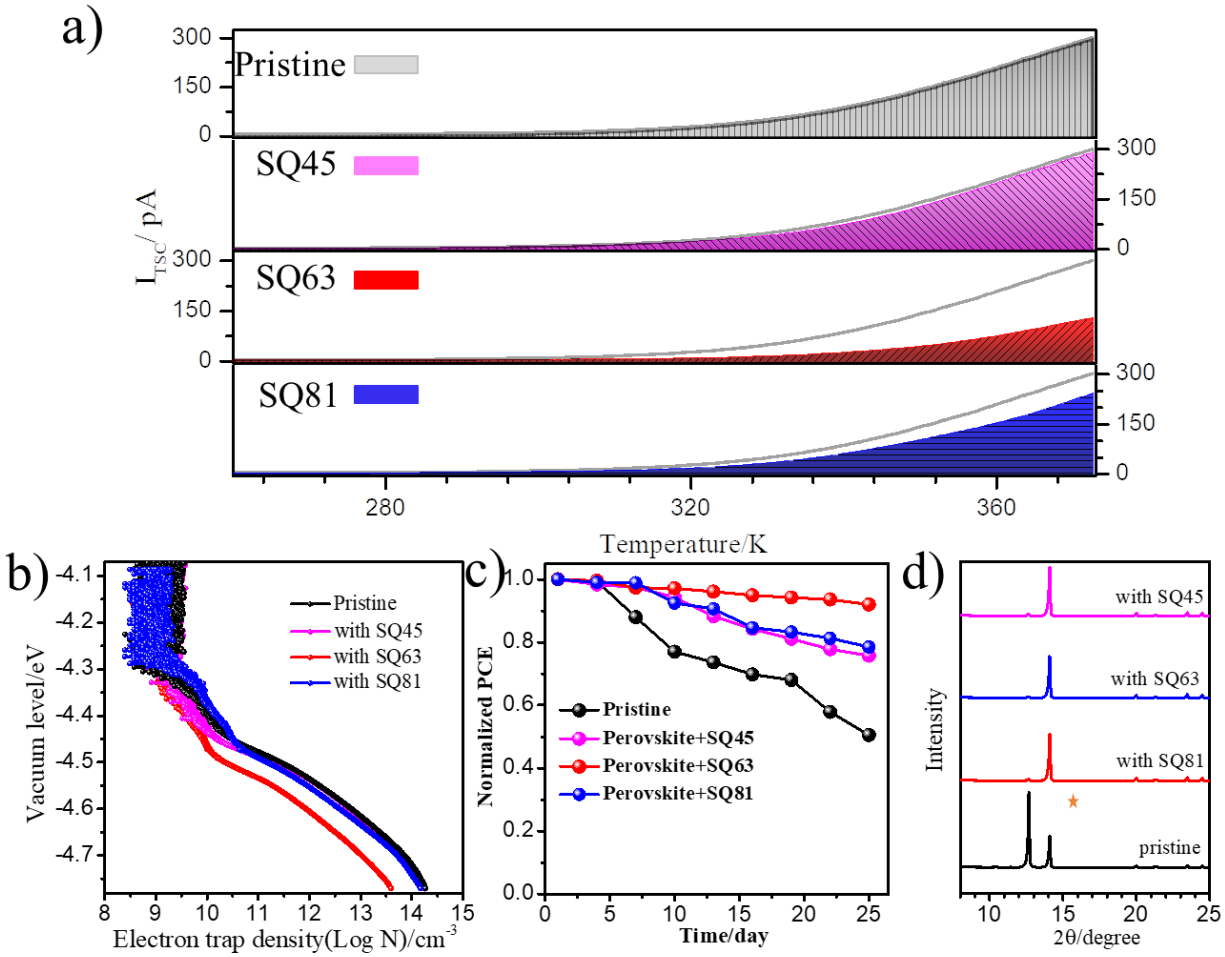

Figure 4.5 a) TSC spectra of pristine, S45, SQ63 and SQ81 perovskite, the colored area demonstrates the amount of trap density in corresponding perovskite films. b) Vacuum level of perovskite as a function of trap density and trap density distribution of perovskite with and without SQ molecules passivation. c) Performance stability of the reference cell and SQ-passivated PSCs without encapsulation stored in air with humidity of 60% RH. d) XRD pattern of corresponding perovskite films after 20 days kept in air at 60±5% RH.

Recent studies have demonstrated that the defects on perovskite GBs initialized the degradation due to the sensitivity of organometal halide perovskite to moisture and oxygen.[26] So the strong interaction of perovskite films with SQ molecules is expected to enhance the stability of perovskite device because SQ molecules could inhibit the diffusion of oxygen and moisture through the defects. Ambient stability of perovskite solar cells without sealing was investigated, perovskite solar cells with three SQ molecules passivation after treatment showed excellent air stability, retaining 92% of the initial PCE for SQ63-passivated perovskite respectively after 600 hours in air at 60%±5% RH (Figure 4.5 c). In comparison, the pristine PSCs degraded to 50% of its initial performance under the same condition. We have also performed XRD measurement for the perovskite films with and without SQ passivation kept at ambient atmosphere with about 60% RH. The XRD patterns (Figure 4.5 d) confirmed the well-maintained crystal perovskite structure after SQ passivation compared with the pristine sample with observable PbI2 signals in the film, this indicates enhanced moisture stability of perovskite film through passivation by SQ molecules. These results clearly demonstrate that SQ-passivated perovskite films possess better moisture resistance and much slower degradation of perovskite layer, which confirmed that SQ molecules could effectively reduced trap sites and enhance the moisture stability of photovoltaic device.

4.4 Conclusions

In summary, we synthesized squaraine molecules and proposed a strategy to passivate the defects in perovskite through the coordination between SQ and perovskite grains, SQ with zwitterion structure could simultaneously passivate the under-coordinated Pb^{2+} vacancies and Pb-I antisite defects between adjacent perovskite grains during the crystal growth, resulting in considerable reduced deep trap density of perovskite as evidenced by TSC measurement. These strong interactions also control the crystal growth to obtain relatively smooth and uniform

perovskite film during the annealing process. In addition, SQ63 molecules with better energy alignment yielded more efficient charge transfer and much reduced deep-level trap density, which resulted in considerable enhancement of the PCE from 15.77% for the pristine device to 18.83% with the FF approaching 80%. Furthermore, considerable retardation of solar cell degradation was achieved by SQ molecules passivation, retaining 87%~90% of its initial efficiency after 600 h of exposure in air at 60% RH without encapsulation. This work provides a new strategy for SQ molecular design and synthesis with suitable energy level to effectively aid charge transfer and passivate the perovskite GBs, making it possible for realizing highly efficient and stable perovskite device.

References

[1] Q. Wang, B. Chen, Y. Liu, Y. Deng, Y. Bai, Q. Dong, J. Huang, *Energy & Environmental Science* **2017**, 10, 516.

[2] X. Zhu, S. Zuo, Z. Yang, J. Feng, Z. Wang, X. Zhang, S. Priya, S. Liu, D. Yang, *ACS applied materials & interfaces* **2018**.

[3] E. Mosconi, D. Meggiolaro, H. J. Snaith, S. D. Stranks, F. De Angelis, *Energy & Environmental Science* **2016**, 9, 3180.

[4] I. Hwang, I. Jeong, J. Lee, M. J. Ko, K. Yong, *ACS applied materials & interfaces* **2015**, 7, 17330.

[5] X. Li, C. C. Chen, M. Cai, X. Hua, F. Xie, X. Liu, J. Hua, Y. T. Long, H. Tian, L. Han, *Advanced Energy Materials* **2018**, 1800715.

[6] X. Li, M. I. Dar, C. Yi, J. Luo, M. Tschumi, S. M. Zakeeruddin, M. K. Nazeeruddin, H. Han, M. Grätzel, *Nature chemistry* **2015**, 7, 703.

[7] Y. Shao, Z. Xiao, C. Bi, Y. Yuan, J. Huang, *Nature communications* **2014**, 5, 5784.

[8] A. Abate, M. Saliba, D. J. Hollman, S. D. Stranks, K. Wojciechowski, R. Avolio, G. Grancini, A. Petrozza, H. J. Snaith, *Nano letters* **2014**, 14, 3247.

[9] J.-W. Lee, H.-S. Kim, N.-G. Park, *Accounts of chemical research* **2016**, 49, 311.

[10] G. Chen, H. Sasabe, T. Igarashi, Z. Hong, J. Kido, *Journal of Materials Chemistry A* **2015**,

3, 14517.

[11] R. W. Bigelow, H.-J. Freund, *Chemical Physics* **1986**, 107, 159.

[12] D. Bi, C. Yi, J. Luo, J.-D. Décoppet, F. Zhang, S. M. Zakeeruddin, X. Li, A. Hagfeldt, M. Grätzel, *Nature Energy* **2016**, 1, 16142.

[13] J. Xu, A. Buin, A. H. Ip, W. Li, O. Voznyy, R. Comin, M. Yuan, S. Jeon, Z. Ning, J. J. McDowell, *Nature communications* **2015**, 6, 7081.

[14] T. Niu, J. Lu, R. Munir, J. Li, D. Barrit, X. Zhang, H. Hu, Z. Yang, A. Amassian, K. Zhao, *Advanced Materials* **2018**, 30, 1706576.

[15] C. Liu, K. Wang, P. Du, C. Yi, T. Meng, X. Gong, *Advanced Energy Materials* **2015**, 5, 1402024.

[16] C. Sun, Z. Wu, H. L. Yip, H. Zhang, X. F. Jiang, Q. Xue, Z. Hu, Z. Hu, Y. Shen, M. Wang, *Advanced Energy Materials* **2016**, 6.

[17] Z. Wang, M. A. Kamarudin, N. C. Huey, F. Yang, M. Pandey, G. Kapil, T. Ma, S. Hayase, *ChemSusChem* **2018**.

[18] S. You, H. Wang, S. Bi, J. Zhou, L. Qin, X. Qiu, Z. Zhao, Y. Xu, Y. Zhang, X. Shi, *Advanced Materials* **2018**, 30, 1706924.

[19] C. Liu, Z. Huang, X. Hu, X. Meng, L. Huang, J. Xiong, L. Tan, Y. Chen, *ACS applied materials & interfaces* **2018**, 10, 1909.

[20] A. Baumann, S. Väth, P. Rieder, M. C. Heiber, K. Tvingstedt, V. Dyakonov, *The journal of physical chemistry letters* **2015**, 6, 2350.

[21] W. S. Yang, B.-W. Park, E. H. Jung, N. J. Jeon, Y. C. Kim, D. U. Lee, S. S. Shin, J. Seo, E. K. Kim, J. H. Noh, *Science* **2017**, 356, 1376.

[22] H. Wei, Y. Fang, P. Mulligan, W. Chuirazzi, H.-H. Fang, C. Wang, B. R. Ecker, Y. Gao, M. A. Loi, L. Cao, *Nature Photonics* **2016**, 10, 333.

[23] M. H. Du, *Journal of Materials Chemistry A* **2014**, 2, 9091.

[24] M.-H. Du, *The journal of physical chemistry letters* **2015**, 6, 1461.

[25] D. Wei, F. Ma, R. Wang, S. Dou, P. Cui, H. Huang, J. Ji, E. Jia, X. Jia, S. Sajid, *Advanced Materials* **2018**, 30, 1707583.

[26] F. Wang, W. Geng, Y. Zhou, H. H. Fang, C. J. Tong, M. A. Loi, L. M. Liu, N. Zhao, *Advanced Materials* **2016**, 28, 9986.

Chapter 5. Divalent S^{2-} doping in all-inorganic perovskite solar cells for enhanced performance and highly stability

5.1 Introduction

Past several years have been witnessing the development of the organic-inorganic perovskite solar cells (PSCs) as a booming technology due to its low-cost fabrication process and high power conversion efficiency with exceeding 23%,[1-3] which is economically attractive and approaches the commercialization of perovskite device. However, the instability of organic-inorganic hybrid perovskite critically hampers the development, because these inorganic-organic hybrid PSCs are prone to damage upon exposure to moisture and decompose under thermal stress at high temperature. This problem should be resolved because the installed perovskite device in the future will be operated under a harsh atmosphere with relatively high humidity and temperature, otherwise. Therefore, Cs-based all-inorganic perovskite is reported to be suitable and much desired due to its thermal stability and attractive device performance. $CsPbX_3$ (X=I or Br) perovskite with more bromide component shows high band gap, $CsPbBr_3$ with best reported stability shows 2.3 eV bandgap which is too large to absorb light beyond 550nm in the spectrum.[4] The $CsPbI_3$ with 1.73 eV bandgap exhibits long-range wavelength spectrum, but it easily suffers from non-perovskite phase transition from the perovskite phase at low temperature.[5-6] Therefore, $CsPbI_2Br$ and $CsPbIBr_2$ are proposed to be promising candidates to achieve the desired efficiency with relative enhanced stability.[7-8]

Recently, precise controlled all-inorganic perovskite crystal growth at room temperature or mild annealing process was investigated, achieving record efficiency of $CsPbI_3$ or $CsPbI_2Br$.[9-10]

In order to enhance their phase stability, perovskite film surface passivation using organic component has been investigated to prevent moisture invasion[11] resulting in state-of-the-art efficiency and stability. Additionally, quasi-2D all-inorganic perovskite was also proved to show higher performance and long-term stability.[12] Despite much improved efficiency of all-inorganic perovskite was achieved, the phase stability of all-inorganic perovskite especially exposure to moisture is still not addressed effectively. Also, in our best knowledge, no work reported the preparation of all-inorganic perovskite under ambient air with high humidity. Divalent S^{2-} exhibits high electronegative nature compared with that of Br^- or I^-,[13] which is expected to have strong chemical bonds with perovskite structure and increases electrostatic interaction to stabilize perovskite phase.[14] Our group applied sulfur atoms at the perovskite surface for efficient interfacial passivation, sulfur atoms filled with the non-negligible iodide vacancies on the surface during the perovskite crystal growth. As a result, the long-term stability and higher efficiency were achieved. [15]

In this chapter, we proposed sulfur doped in $CsPbIBr_2$ all-inorganic perovskite to achieve high efficiency and superior phase stability under humid air with 65% RH. Cesium phenethyl xanthate (CsXth) with high solubility as a sulfur source was used as additives in $CsPbIBr_2$ perovskite. CsXth could be decomposed into cesium sulfides to form stable cubic all-inorganic perovskite during the low-temperature annealing. Xth-induced crystallization engineering to realize sulfur doping in perovskite was achieved. The perovskite phase stability was significantly enhanced from 2 h for the reference perovskite to 432 h in ambient air with 65% RH. Additionally, the bandgap of $CsPbIBr_2$ perovskite was widened greatly after only 2 min aging time in 100% RH atmosphere. However, the bandgap of sulfur-doped perovskite almost keeps the same value after 240 min storage in the same condition. Furthermore, a champion efficiency of 9.78% with a high

open-circuit voltage of 1.30 v was achieved, all of which are the highest values in $CsPbIBr_2$ PSCs. Almost no decay of perovskite performance in 10 h was achieved under ambient air with 65% RH without encapsulation.

5.2 Experimental

5.2.1 Preparation of perovskite solar cells

ITO glasses were sonicated with distilled water, acetone and isopropanol sequentially for 15 min in each solvent, 15 min UV-O_3 treatment was further performed on ITO substrates prior to the deposition of SnO_2 compact layer. Diluted SnO_2 colloid solution (2.67 % in water) was spin-coated on ITO substrates with 2000 rpm for 30 s and then annealed at 150 °C for 30 min, then $SnCl_2$ solution (0.1 M in ethanol) was spin-coated on SnO_2 compact layer with 6000 rpm for 30 s and annealed at 180°C for 1 h.$CsPbIBr_2$ perovskite precursor solution was prepared through mixing CsI (1.35 M) and $PbBr_2$ (1.35 M) in pure DMSO solvent. For CsXth in perovskite solution, 2.5%, 5% and 10% M/M CsXth was dissolved in $CsPbIBr_2$ precursor respectively. All-inorganic perovskite film was fabricated by spin-coating 75 μl perovskite precursor solution at 1000 rpm for 20 s and 3000 rpm for 30 s, 500 μl ethyl acetate was dropped quickly onto the film at the last 10 s during the second step. Then the film was annealed on hotplate at 160 °C for 10min, for CsXth in perovskite, the film was annealed on hotplate at 160 °C for 5 min and increased to 230 °C slowly and annealed for 10 min in inert atmosphere. After cooling down to room temperature, P3HT solution (10 mg/ml in chlorobenzene) was spin-coated at 3000 rpm for 30 s and annealed at 160 °C for 10 min. Finally, 80 nm gold was evaporated as electrode under high vacuum ($<4\times10^{-3}$ Pa).

5.2.2 Characterization

Perovskite film morphology was performed by SEM (HITACHI S4800). The current

density-voltage characteristics of solar cells were conducted under AM 1.5G simulated solar illumination, the active area of each solar cell was 0.10 cm^2 during the test. The external quantum efficiencies were measured by illuminating solar cells under monochromatic light from 900 nm to 300 nm (300W Xenon lamp with a monochromator, Newport 74010). The EQE was performed by under monochromatic light from 800 nm to 300 nm (300W Xenon lamp with a monochromator, Newport 74010). Transform Infrared Spectroscopy (FTIR) measurement was conducted using JASCO FTIR 4100 in transmission mode. XRD pattern was analyzed by D8 X-ray diffractometer, using Cu Kα radiation. The steady-state photoluminescence (PL) and timed-resolved PL measurement was obtained by the Fluorolog-3-p spectrophotometer by excitation light. X-ray photoelectron spectroscopy (XPS) system with Thermo Scientific and C_{1s} binding energy at 284.8 ev as the referenced was applied, ESCLAB 250Xi was used to measure the binding energy of Pb_{4f}, Cs_{3d}, Br_{3d} and S_{2p} element. Electrochemical impedance spectra was measured by an electrochemical workstation (Parstat 2273, Princeton) under 0.6V positive bias. FTIR for perovskite thin films was measured using PRO400-S mode. Thermogravimetric analysis (TGA) was conducted in nitrogen atmosphere at a temperature rate of 10°C per min.

5.3 Results and Discussion

5.3.1 Optoelectronic properties of sulfur doped perovskite

Xanthates with different metal have been proved to be decomposed into corresponding metal sulfides at a different temperature,[16-18] the decomposition reaction of CsXth by thermal annealing is presented as follows

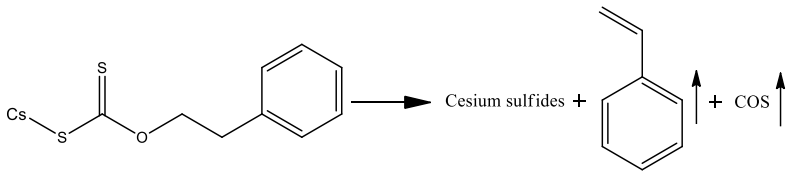

Figure 5.1 a illustrates the potential mechanism of CsXth decomposition into cesium sulfides for sulfur-doped $CsPbIBr_2$ perovskite film. For the sulfur-doped film is heated on 160 for 5 min and slowly increase to 230 for 10 min to ensure the complete decomposition of CsXth. In order to investigate the influence of CsXth decomposition on perovskite crystallinity, scanning electron microscopy (SEM) was measured to examine the morphology with and without CsXth decomposition. As shown in Figure 5.1 b, there are numerous voids and crease within perovskite grains and therefore extremely low crystallization. These disadvantages easily induced shutting paths and unfavourable interfacial charge transfer in perovskite device. [19] When 2.5%, 5% CsXth was decomposed in situ inside perovskite film under 230°C thermal annealing (Figure 5.1 c and d), neighboring grains were expected to become closer and the grain boundary appeared to be blurred upon CsXth decomposition(a% CsXth-$CsPbIBr_2$ is used to mark a% CsXth additives following 230°C annealing resulting in sulfur doping). $CsPbIBr_2$ perovskite film was voids-free and more compact with seemingly low surface roughness. However, 10% CsXth-$CsPbIBr_2$ exhibited submicrometer-sized voids and the surface coverage decreased seriously (Figure 5.1e).

We measured x-ray photoelectron spectroscopy (XPS) to investigate the interaction in perovskite structure. Cs_{3d} XPS spectra slightly shift to lower binding energy for sulfur incorporated in perovskite (Figure 5.2 a), proving the strong interaction of Cs-S, consistent with the reported trend.[14] Additionally, similar trends of Pb_{4f}, I_{3d} and Br_{3d} XPS spectra were observed in Figure 5.2 b-d,

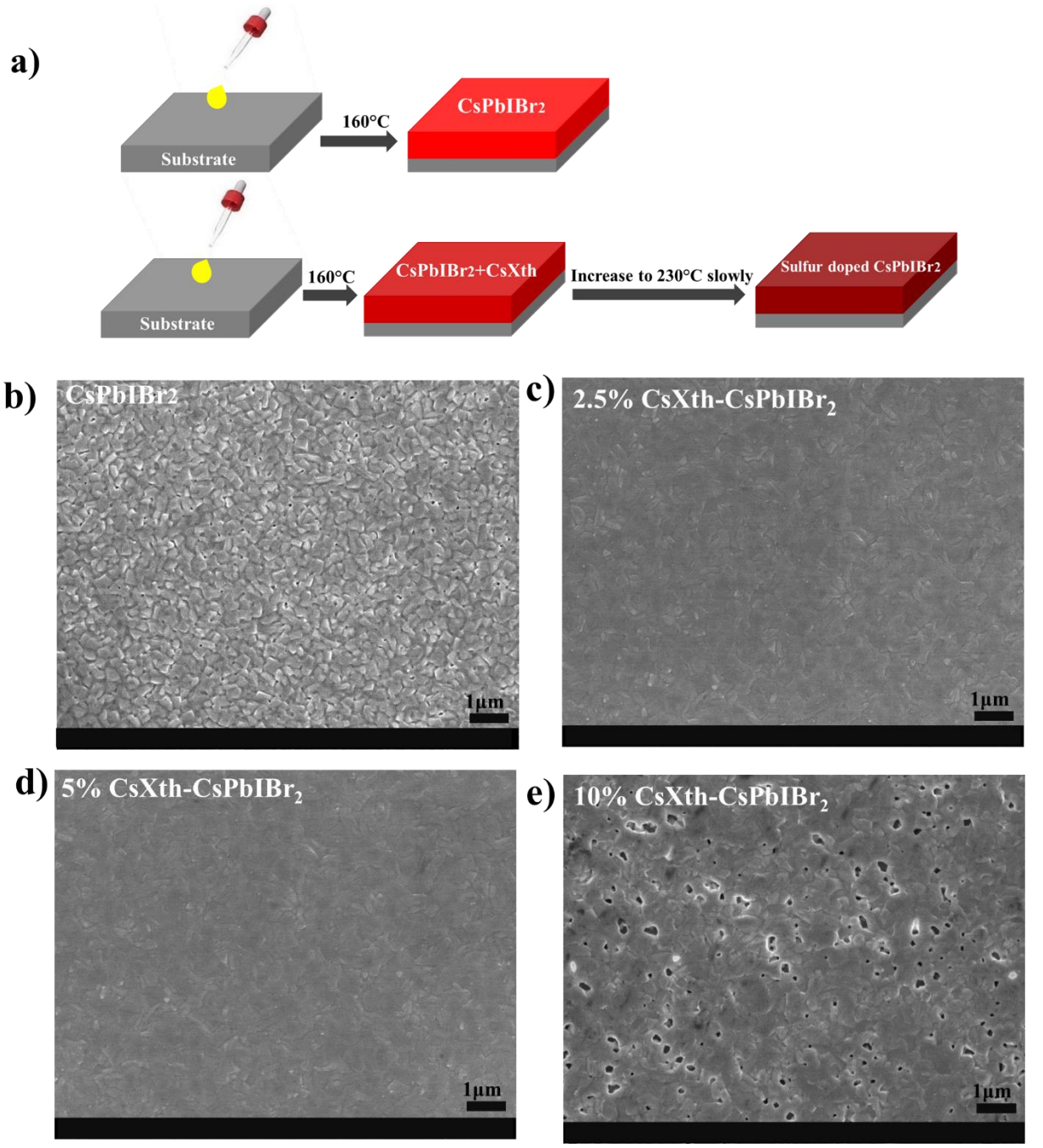

Figure 5.1 a) Schematic diagram of CsXth doped in all-inorganic perovskite and evolution mechanism of CsXth-induced formation of cubic $CsPbIBr_2$ upon decomposition during annealing. Top-view SEM images of $CsPbIBr_2$ b) without and with c) 2.5%, d) 5%, e) 10% CsXth in perovskite films after 230°C annealing.

indicating the existence of an interaction between S and Pb or halide due to the stronger

electronegativity of sulfur. These interactions could assist in stabilizing the all-inorganic perovskite phase and be favourable to the device performance discussed below. Figure 5.2 e displays the S_{2p} XPS spectra before and after CsXth decomposition, we calculated the ratio of Pb to S under different temperature annealing through quantitative analysis, the ratio of S to Pb for 160°C and 230°C treatment was 0.11:1 and 0.028:1 respectively. Three-quarter reduction in sulfur content was in accordance with the decomposition reaction mechanism. Electronic structures of different perovskite films are studied by photoelectron yield spectroscopy (PYS), which was performed to investigate the occupied electron states of semiconductor materials through monitoring the photoelectron current from the valence band maximum (VBM) as increased

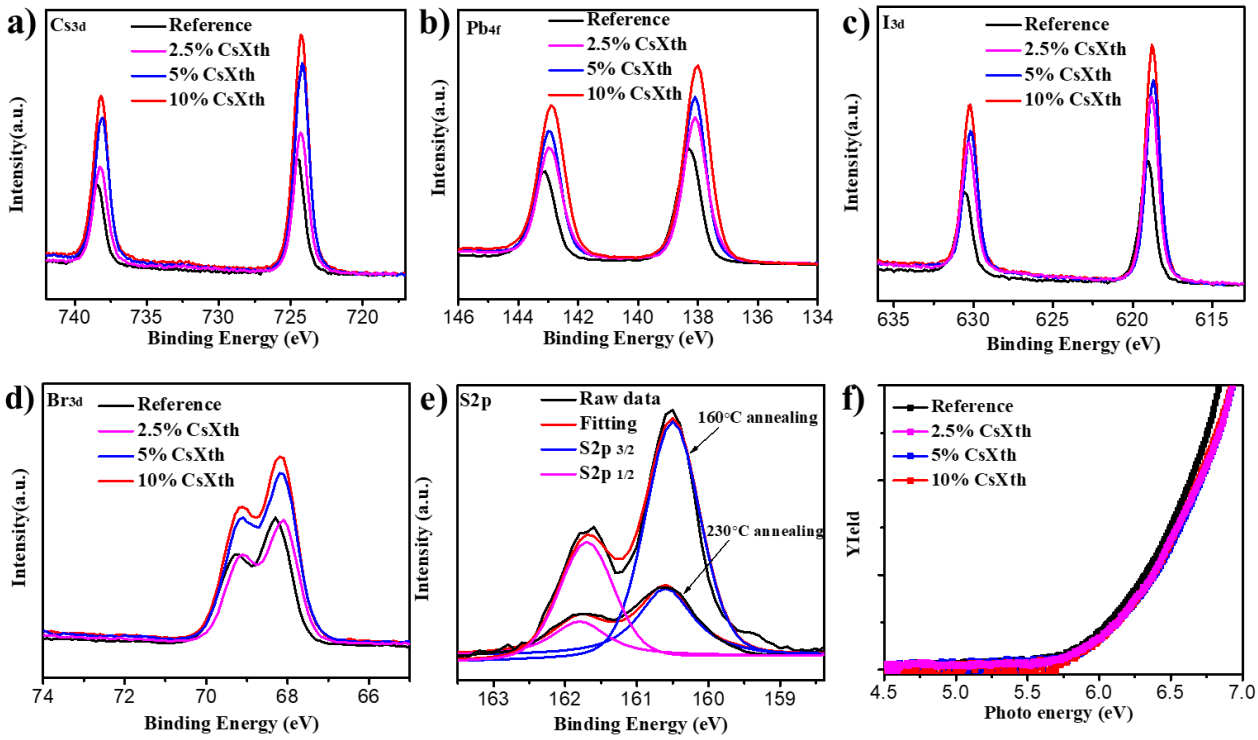

Figure 5.2 X-ray photoelectron spectroscopy (XPS) spectra of a) Cs_{3d}, b) Pb_{4f} ,c) I_{3d} and d) Br_{3d} under 230°C thermal annealing. e) XPS spectra comparison of S_{2p} under 160°C and 230°C thermal annealing respectively. d) Photoelectron yield spectroscopy (PYS) spectra of $CsPbIBr_2$ and 2.5%, 5%, 10% CsXth-$CsPbIBr_2$ films.

incident photon energy.[20] Figure 5.2 f displays the corresponding PYS spectra, showing the slightly shifted lower VBM (5.80 eV, 5.81 eV and 5.84 eV for 2.5%, 5% and 10% CsXth-$CsPbIBr_2$ perovskite respectively) compared with the reference perovskite film (5.78 eV), but this slight shift was not expected to influence the charge transfer.

5.3.2 The phase stability of all-inorganic cubic perovskite

Sulfur-doping in $CsPbIBr_2$ crystals were expected to stabilize perovskite phase due to its greater electronegativity and strong interaction with perovskite lattices, whereas all-inorganic perovskite exhibits higher sensitivity to moisture compared with organic-inorganic hybrid perovskite.[21] In Figure 5.3 a, $CsPbIBr_2$ and 5% CsXth-$CsPbIBr_2$ perovskite thin films were stored in ambient air with 65% RH, $CsPbIBr_2$ film showed phase transition from perovskite phase to non-perovskite phase completely (insets photographs) in 2 h accompanying the decreased optical absorbance sharply, By contrast, 5% CsXth-$CsPbIBr_2$ thin film remained the dark brown color after 432 h exposure to humid air, and negligible change of absorbance in 432 h was observed.

In order to further investigate films stability after sulfur-doped in perovskite, we further created 100% RH atmosphere to test the sensitivity to moisture following previous method (Figure S8b),[14] Figure 5.3 b and c display Tauc plots of reference $CsPbIBr_2$ and 5% CsXth-$CsPbIBr_2$ films to examine the evolution of perovskite bandgaps in 100% RH condition. The reference film absorbed water in 100% RH atmosphere and the color faded in 2 min quickly, meanwhile, its bandgap was widened from 2.03 eV to 2.34 eV. However, the bandgap of 5% CsXth-$CsPbIBr_2$ perovskite exhibited almost constant (2.05 eV) after aging 240 min in 100% RH. Based on these stability results, as shown in Figure 5.3 d, CsXth was decomposed into cesium sulfides, which distributed near perovskite grains, sulfur with strong electronegativity was inserted into the

interstices of $CsPbIBr_2$ and was expected to stabilize α-phase of all-inorganic perovskite and prevent moisture invasion.[22] Normally, for all-inorganic perovskite, moisture can easily trigger phase transition to the non-perovskite phase by introducing halide vacancies in perovskite host lattice (Figure 5.3 e), resulting in the reduction of surface tension and thus accelerating the transition rate due to the existence of halide vacancies.[23-24]

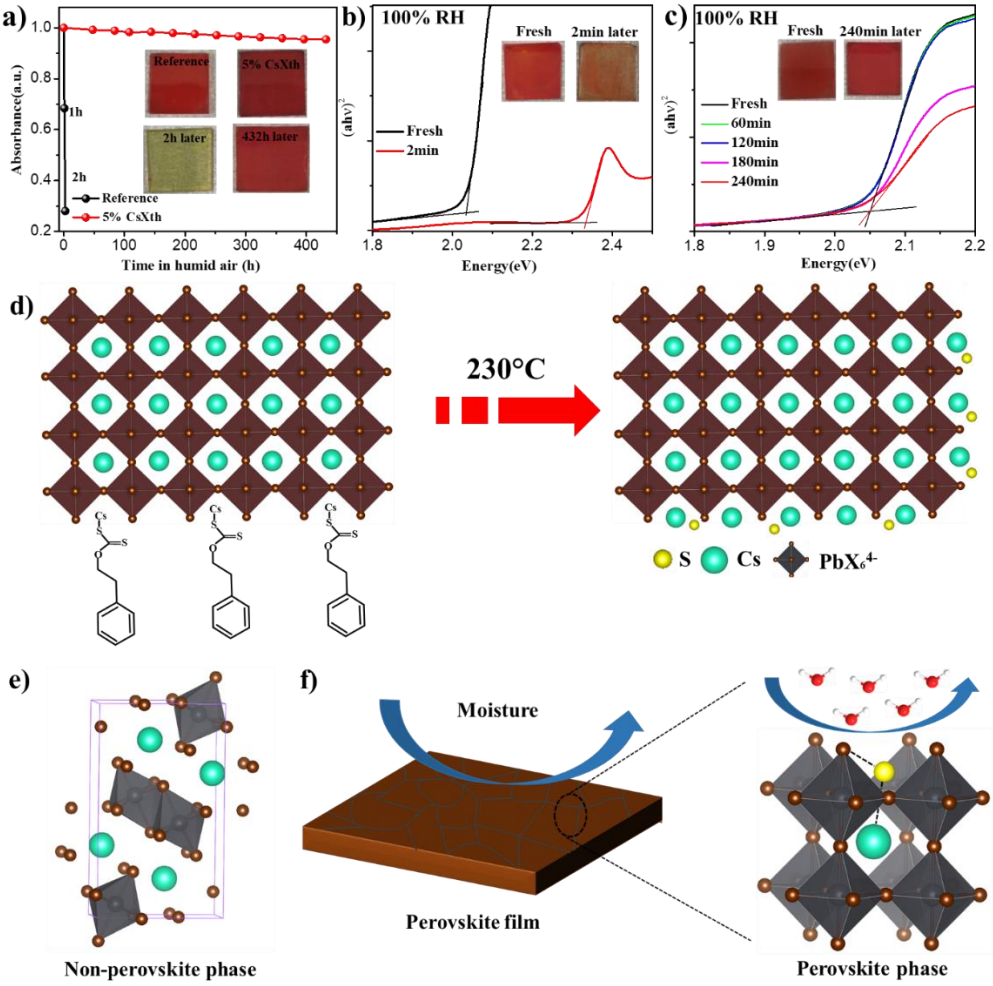

Figure 5.3 a) Time evolution of $CsPbIBr_2$ and 5% CsXth-$CsPbIBr_2$ perovskite film in humid air , Vertical axis is the normalized absorbance at the bandedge, inset images are corresponding films before and after aging time. Tauc plots of b) $CsPbIBr_2$ and c) 5% CsXth-$CsPbIBr_2$ thin films under100% RH condition. d) Illustration of CsXth decomposition and sulfur doping in perovskite. e) Sketch of non-perovskite phase. f) Schematic illustration of sulfur in lattice for improved stability under high humidity.

However, when sulfur was doped in perovskite lattice upon CsXth decomposition, sulfur could coordinate with atoms in perovskite structure and prevent halide loss in perovskite lattice[14, 21] due to the electrostatic interaction with perovskite, while retaining the high surface tension between perovskite and non-perovskite structures (Figure 5.3 f). These have been proved from the peak shift of the elements (Br, I, Pb, Cs) in XPS measurement in Figure 3 discussed below. As a result, the cubic perovskite phase can be maintained regardless the presence of moisture.

5.3.3 The performance of all-inorganic solar cells

We fabricated $CsPbIBr_2$ PSCs in the configuration of indium tin oxide (ITO)/SnO_2 NPs/$CsPbIBr_2$/P3HT/Au (Figure 5.4 a). The $CsPbIBr_2$ PSCs without treatement show the efficiency of 5.16% with Jsc of 8.83 mA cm^{-2}, Voc of 1.07 V and fill factor (FF) of 54.5% (Figure 5.4 b), this low performance can be ascribed to the low quality of perovskite due to the notorious voids on surface, leading to the shunting paths at the interface and serious charge recombination.[25] The efficiency increased as the doped sulfur contents in perovskite increased. The best performing device was achieved based on 5% CsXth-$CsPbIBr_2$ as light absorber with the efficiency of 9.78%, Jsc of 10.19 mA cm^{-2}, Voc of 1.30 V and FF of 73.81%, detailed device parameters are given in Table 5.1. Encouragingly, a remarkable of 90% efficiency enhancement was achieved by sulfur doping upon 5% CsXth decomposition. To the best of knowledge, this is a record efficiency for $CsPbIBr_2$ perovskite reported so far. Also, the V_{oc} of 1.30 V maybe stands the highest value, indicating the minimized energy loss (E_{loss}). Additionally, current density of $CsPbIBr_2$ perovskite enhanced from 8.83 mA cm^{-2} to 10.19 mA cm^{-2}, which agrees with the integrated current densities for $CsPbIBr_2$ (8.75 mA cm^{-2}) and 5% CsXth-$CsPbIBr_2$ (9.88 mA cm^{-2}) PSCs with errors less than 5% (Figure 5.4 c). In order to make sure the reliability of sulfur-doped perovskite performance,

we measured the PCE of best-performing PSCs as a function of time held at 1.05 V bias (V_{MP} value), as shown in Figure 5.4 d, a PCE of about 9.58% can be obtained finally, which is close to that obtained by J-V measurements. When the 10% CsXth-$CsPbIBr_2$ was prepared as light absorber, the corresponding performance of PSCs drops to 5.38% efficiency significantly with J_{sc} of 7.84 mA cm^{-2},V_{oc} of 1.12 V and FF of 61.42%, this maybe originated from the bad quality morphology measured from SEM and poor charge transport due to increased sulfur contents, resulting in the low-resistance shunting paths in perovskite devices.[19]

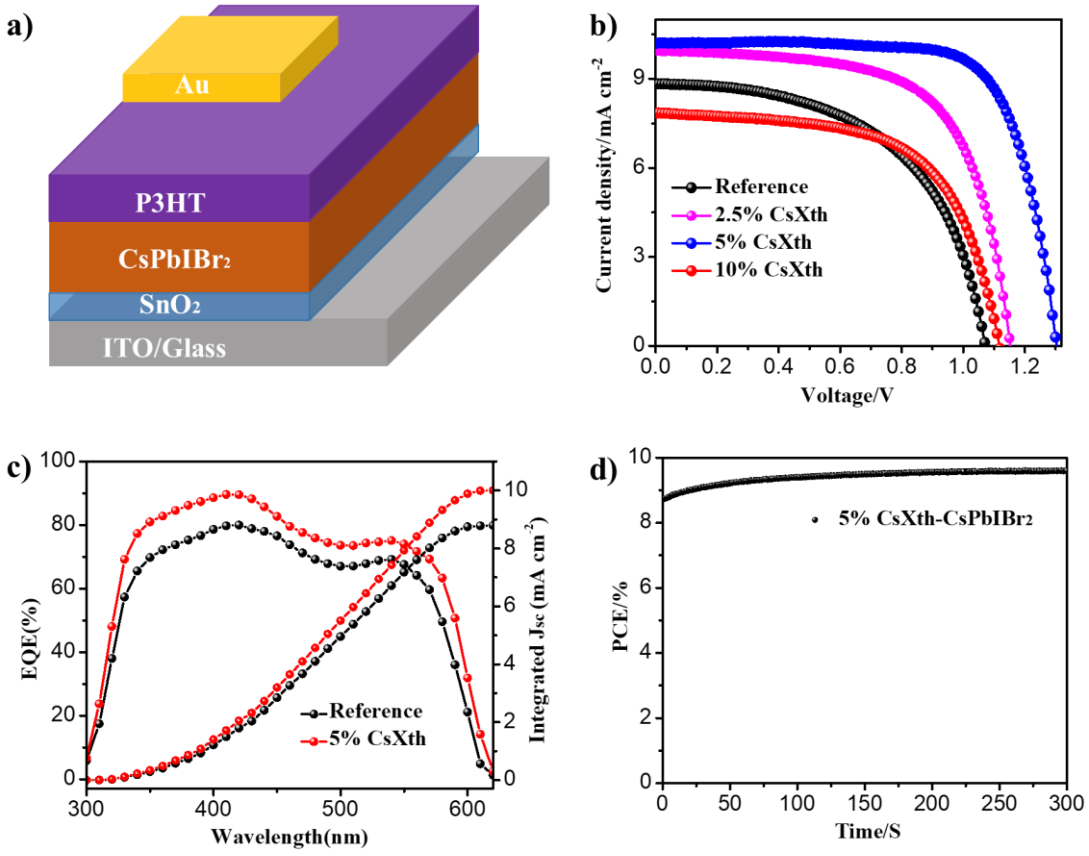

Figure 5.4 a) Schematic diagram of fabricated PSCs with the structure of ITO/SnO_2/$CsPbIBr_2$/P3HT/Au. b) J-V characteristics of best performing PSCs based on $CsPbIBr_2$ and 2.5%, 5%, 10% CsXth-$CsPbIBr_2$. c) External quantum efficiency (EQE) spectra and integrated Jsc of $CsPbIBr_2$ and 5% CsXth-$CsPbIBr_2$. d) PCE as a function of time held at 1.05 V bias.

Table 5.1 Parameters of planar all-inorganic PSCs based on $CsPbIBr_2$ and a% CsXth-$CsPbIBr_2$ as light absorber at forward (F) and reverse (R) scan.

		J_{sc}(mA cm^{-2})	V_{oc} (V)	FF (%)	PCE (%)	Hysteresis Index (%)
Reference	F	8.89	1.04	43.91	4.05	22
	R	8.83	1.07	54.50	5.16	
2.5% CsXth	F	9.95	1.15	65.96	7.54	2
	R	9.95	1.15	64.43	7.39	
5% CsXth	F	10.28	1.30	67.76	9.06	7
	R	10.19	1.30	73.81	9.78	
10% CsXth	F	7.84	1.12	61.42	5.38	5
	R	7.84	1.10	59.47	5.12	

In mixed halide all-inorganic perovskite the phase segregation is more obvious under light illumination, resulting in formation of iodide and bromide-rich phases because of the reduced free energy of perovskite materials in the excited state.[26-27] Moreover, this phase segregation was thought to be responsible for more serious hysteresis due to the ion migration.[28] Figure 5.5 a showed The J-V characteristics of perovskite devices based on $CsPbIBr_2$ and 5% CsXth-$CsPbIBr_2$ as light absorbers at forward (F) and reverse (R) scan directions. A rather strong hysteresis with a hysteresis index of about 22% as defined according to the following equation. [29]

$$\text{Hysteriesis Index} = \frac{PCE_{reverse} - PCE_{forward}}{PCE_{reverse}}$$

The strong hysteresis should be induced by enhanced ion migration at the grain boundaries or interface arising from phase segregation. [28, 30] However, the hysteresis index based on 5% CsXth-$CsPbIBr_2$ perovskite was reduced to 7%, additionally, the corresponding hysteresis index for 2.5% and 10% CsXth-$CsPbIBr_2$ perovskites were reduced to 2% and 5% respectively although the efficiency has dropped greatly when 10% CsXth was added in perovskite (Table 5.1). We speculated that sulfur doped perovskite could prevent the migration of halide/interstitials induced by an external electrical bias, [30] because the ion migration and accumulation can lead to serious hysteresis. Furthermore, crystal defects near grain boundaries can act as ion migration channels in perovskite film and induce stronger hysteresis behavior, sulfur-doped perovskite without voids could effectively hinder ion migration.[29] We also found that the steady photoluminescence (PL) peak at about 600 nm coupled with a shoulder peak at 682 nm (Figure 5.5 b), this shoulder peak was observed frequently in previous reports,[31-32] this was explained by the halide ions and sequent phase segregation to form I^- and Br^- dominated phases. Interestingly, the shoulder peak eliminated following various amount of sulfur doping in perovskite film. More importantly, the PL spectra of 2.5% and 5% CsXth-$CsPbIBr_2$ perovskite film exhibited a significant increase, indicating the decreased crystal defects and carrier recombination centers, effectively suppressing hysteresis phenomena as discussed above. Time-resolved photoluminescence (TRPL) decay spectra were fitted by a double exponential decay function, showing that sulfur-doped perovskite exhibited longer carrier lifetime compared with the reference perovskite (Figure 5.5 c). The fast decay component (τ_1) is mainly correlated to interfacial charge transfer, and the slow decay (τ_2) was caused by radiative recombination of free carriers. [33]

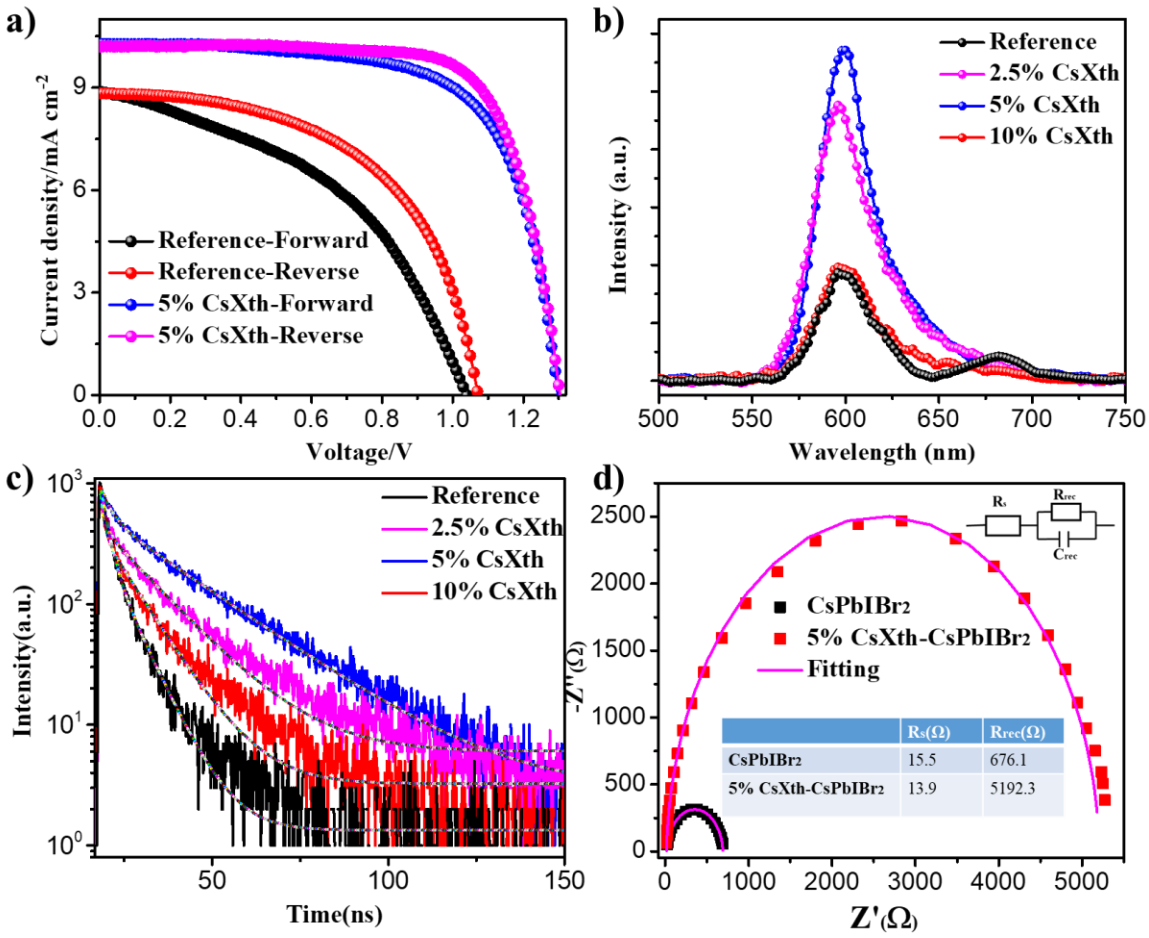

Figure 5.5 a) J-V characteristics of $CsPbIBr_2$ and 5% CsXth-$CsPbIBr_2$ PSCs measured by forward and reverse scan. b) Steady-state PL and c) time-resolved PL spectra for $CsPbIBr_2$ and a% CsXth-$CsPbIBr_2$ perovskite on glass. d) Nyquist plots of $CsPbIBr_2$ PSCs with fitting results under 0.6 V in dark condition, equivalent circuit diagram was inserted.

In this case, τ_2 was increased from 6.75 ns (around 600 nm) for reference perovskite to 13.87 ns, 21.63 ns and 9.39 ns for 2.5%, 5% and 10% CsXth respectively. Such dramatic prolonging τ_2 is ascribed to compositional traps resulted from the voids-free and compact morphology due to the existence of sulfur in perovskite film. Additionally, the electrochemical impedance spectroscopy (EIS) of $CsPbIBr_2$ and 5% CsXth-$CsPbIBr_2$ PSCs was measured at 0.6 V in dark condition (Figure 5.5 d), we extracted the recombination resistance (R_{rec}) and series resistance (R_s) from Nyquist

plots of PSCs based on equivalent circuit model. The value of Rs decreased from 15.5 Ω to 13.9 Ω upon 5% CsXth decomposition within film, R_{rec} increased significantly from 676.1 Ω for reference cell to 5192.3 Ω for 5% CsXth-$CsPbIBr_2$ device, this indicated that the charge recombination was suppressed effectively, leading to the enhanced charge extraction and reduced hysteresis of perovskite device, these benefits contributed to the improvement of photovoltaic parameters including V_{oc} and FF, which is consistent with previous works that have demonstrated reduction of total charge recombination could enhance electronic properties of perovskites, leading to the improved open-circuit voltage of PSCs.[34-35]

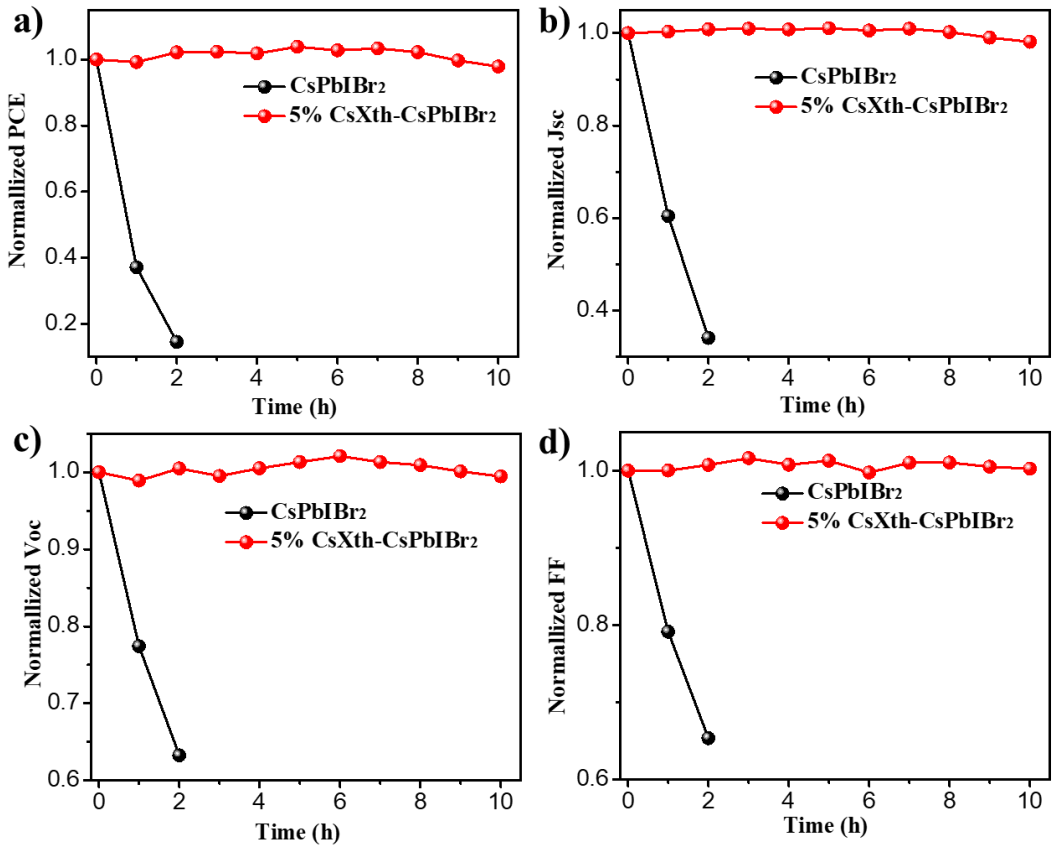

Figure 5.6. Stability tests for normalized a) PCE, b) J_{sc}, c) V_{oc} and d) FF of $CsPbIBr_2$ and 5% CsXth-$CsPbIBr_2$-based PSCs without encapsulation under ambient air with 65% RH.

We have found the greatly enhanced film stability upon the sulfur doping in $CsPbIBr_2$ perovskite. 5% CsXth-$CsPbIBr_2$ perovskite film exhibited improved stability over the reference one in ambient air with 65% RH. We also studied the stability of perovskite devices with or without sulfur doping under the ambient air with 65% RH, as shown in Figure 5.6, the efficiency of reference perovskite device degraded quickly under humid air in 2 h, this can be ascribed to the induced vacancies in $CsPbIBr_2$ perovskite by moisture, accelerating the perovskite phase transition under the lower free energy barrier.[21] However, the efficiency, J_{sc}, V_{oc} and FF of 5% CsXth-$CsPbIBr_2$-based perovskite device maintained almost same of initial values after 10 h exposure to humid air without encapsulation due to the sulfur interaction with perovskite, preventing water molecules penetrating perovskite lattice. These results demonstrated that sulfur in perovskite indeed improved the phase stability and prevent the degradation of PSCs.

5.4 Conclusions

In conclusion, we applied CsXth in all-inorganic perovskite to stabilize the cubic $CsPbIBr_2$ phase after the CsXth was decomposed at a relatively low temperature. Finally, the sulfur-doped $CsPbIBr_2$ perovskite film without voids was prepared successfully under humid air condition, leading to superior stability compared with the control perovskite under ambient air with 65% RH. Also, the value of perovskite bandgap could keep constant in 240 min under 100% RH condition, while the bandgap has been widened in 2 min. the efficiency of sulfur-doped $CsPbIBr_2$ PSCs was enhanced to 9.78% with 1.30 V, which was among the highest values in $CsPbIBr_2$-based PSCs so far. Sulfur in perovskite could effectively prevent phase segregation and suppress hysteresis behavior. Furthermore, parameters of PSCs kept almost the same value in 10 h stored in ambient air with 65% RH. This work provides an effective way to prepare superior stable and efficient inorganic halide perovskite devices.

References

[1] A. Kojima, K. Teshima, Y. Shirai, T. Miyasaka, *Journal of the American Chemical Society* **2009**, 131, 6050.

[2] N. J. Jeon, H. Na, E. H. Jung, T.-Y. Yang, Y. G. Lee, G. Kim, H.-W. Shin, S. I. Seok, J. Lee, J. Seo, *Nature Energy* **2018**, 3, 682.

[3] D. Luo, W. Yang, Z. Wang, A. Sadhanala, Q. Hu, R. Su, R. Shivanna, G. F. Trindade, J. F. Watts, Z. Xu, *Science* **2018**, 360, 1442.

[4] J. Liang, C. Wang, Y. Wang, Z. Xu, Z. Lu, Y. Ma, H. Zhu, Y. Hu, C. Xiao, X. Yi, *Journal of the American Chemical Society* **2016**, 138, 15829.

[5] A. Swarnkar, A. R. Marshall, E. M. Sanehira, B. D. Chernomordik, D. T. Moore, J. A. Christians, T. Chakrabarti, J. M. Luther, *Science* **2016**, 354, 92.

[6] T. Duong, H. K. Mulmudi, H. Shen, Y. Wu, C. Barugkin, Y. O. Mayon, H. T. Nguyen, D. Macdonald, J. Peng, M. Lockrey, *Nano Energy* **2016**, 30, 330.

[7] Q. Zeng, X. Zhang, X. Feng, S. Lu, Z. Chen, X. Yong, S. A. Redfern, H. Wei, H. Wang, H. Shen, *Advanced Materials* **2018**, 30, 1705393.

[8] C. Liu, W. Li, J. Chen, J. Fan, Y. Mai, R. E. Schropp, *Nano Energy* **2017**, 41, 75.

[9] W. Chen, H. Chen, G. Xu, R. Xue, S. Wang, Y. Li, Y. Li, *Joule* **2018**.

[10] P. Wang, X. Zhang, Y. Zhou, Q. Jiang, Q. Ye, Z. Chu, X. Li, X. Yang, Z. Yin, J. You, *Nature communications* **2018**, 9, 2225.

[11] Y. Wang, T. Zhang, M. Kan, Y. Zhao, *Journal of the American Chemical Society* **2018**.

[12] Y. Jiang, J. Yuan, Y. Ni, T. Jiu, M. Yuan, J. Chen.

[13] Q. Chen, N. De Marco, Y. M. Yang, T.-B. Song, C.-C. Chen, H. Zhao, Z. Hong, H. Zhou, Y. Yang, *Nano Today* **2015**, 10, 355.

[14] J. Gong, M. Yang, D. Rebollar, J. Rucinski, Z. Liveris, K. Zhu, T. Xu, *Advanced Materials* **2018**, 30, 1800973.

[15] Z. Wang, M. A. Kamarudin, N. C. Huey, F. Yang, M. Pandey, G. Kapil, T. Ma, S. Hayase, *ChemSusChem* **2018**.

[16] J. Patel, F. Mighri, A. Ajji, T. K. Chaudhuri, *Nano Energy* **2014**, 5, 36.

[17] Y. K. Jung, J. I. Kim, J.-K. Lee, *Journal of the American Chemical Society* **2009**, 132, 178.

[18] F. T. O'Mahony, U. B. Cappel, N. Tokmoldin, T. Lutz, R. Lindblad, H. Rensmo, S. A. Haque, *Angewandte Chemie International Edition* **2013**, 52, 12047.

[19] A. N. Cho, N. G. Park, *Chemsuschem* **2017**, 10, 3687.

[20] M. Sugiyama, T. Shimizu, D. Kawade, K. Ramya, K. Ramakrishna Reddy, *Journal of Applied Physics* **2014**, 115, 083508.

[21] J. Lin, M. Lai, L. Dou, C. S. Kley, H. Chen, F. Peng, J. Sun, D. Lu, S. A. Hawks, C. Xie, *Nature materials* **2018**, 17, 261.

[22] Z. Zeng, J. Zhang, X. Gan, H. Sun, M. Shang, D. Hou, C. Lu, R. Chen, Y. Zhu, L. Han, *Advanced Energy Materials* **2018**, 8, 1801050.

[23] S. Dastidar, D. A. Egger, L. Z. Tan, S. B. Cromer, A. D. Dillon, S. Liu, L. Kronik, A. M. Rappe, A. T. Fafarman, *Nano letters* **2016**, 16, 3563.

[24] A. Mattoni, A. Filippetti, C. Caddeo, *Journal of Physics: Condensed Matter* **2016**, 29, 043001.

[25] W. Zhu, T. Yu, F. Li, C. Bao, H. Gao, Y. Yi, J. Yang, G. Fu, X. Zhou, Z. Zou, *Nanoscale* **2015**, 7, 5427.

[26] R. E. Beal, D. J. Slotcavage, T. Leijtens, A. R. Bowring, R. A. Belisle, W. H. Nguyen, G. F. Burkhard, E. T. Hoke, M. D. McGehee, *The journal of physical chemistry letters* **2016**, 7, 746.

[27] X. Tang, Z. Hu, W. Chen, X. Xing, Z. Zang, W. Hu, J. Qiu, J. Du, Y. Leng, X. Jiang, *Nano Energy* **2016**, 28, 462.

[28] Y. Shao, Y. Fang, T. Li, Q. Wang, Q. Dong, Y. Deng, Y. Yuan, H. Wei, M. Wang, A. Gruverman, *Energy & Environmental Science* **2016**, 9, 1752.

[29] W. Li, M. U. Rothmann, A. Liu, Z. Wang, Y. Zhang, A. R. Pascoe, J. Lu, L. Jiang, Y. Chen, F. Huang, *Advanced Energy Materials* **2017**, 7, 1700946.

[30] C. Li, S. Tscheuschner, F. Paulus, P. E. Hopkinson, J. Kießling, A. Köhler, Y. Vaynzof, S. Huettner, *Advanced Materials* **2016**, 28, 2446.

[31] N. Li, Z. Zhu, J. Li, A. K. Y. Jen, L. Wang, *Advanced Energy Materials* **2018**, 1800525.

[32] W. Zhu, Q. Zhang, D. Chen, Z. Zhang, Z. Lin, J. Chang, J. Zhang, C. Zhang, Y. Hao, *Advanced Energy Materials* **2018**, 8, 1802080.

[33] G. Yin, H. Zhao, H. Jiang, S. Yuan, T. Niu, K. Zhao, Z. Liu, S. Liu, *Advanced Functional Materials* **2018**, 28, 1803269.

[34] N. D. Pham, V. T. Tiong, D. Yao, W. Martens, A. Guerrero, J. Bisquert, H. Wang, *Nano Energy* **2017**, 41, 476.

[35] N. D. Pham, C. Zhang, V. T. Tiong, S. Zhang, G. Will, A. Bou, J. Bisquert, P. E. Shaw, A. Du, G. J. Wilson, *Advanced Functional Materials* **2018**, 1806479.

Chapter 6. General conclusions

This thesis focused on the studies of Pb-based photovoltaic materials and their application in solar cells. The optoelectronic properties of Pb-based materials were improved significantly. In chapter 1, we briefly introduced the power conversion efficiency of solar energy based several light absorbing materials, which exhibited more advantages than conventional fossil fuels on earth. However, several drawbacks still existed although there has much improvement in these Pb-based materials. In order to overcome these drawbacks, we developed new method to optimize optoelectronic properties of QDs or perovskite materials to increase the mobility of PbS QDs and effectively passivate surface or grain boundaries of perovskite polycrystalline.

In chapter 2, we developed a new method to improve the mobility of PbS QDs and performance of QDs solar cells. The ligands of PbS QDs were exchanged by xanthate on surface, finally the decomposition of xanthate at room temperature provided driving force for the formation of sulfur-crosslinking QDs. This improved mobility and decreased QDs film roughness facilitated their use of a p-type light absorbing layer for QDs solar cells. Furthermore, the current density of QDs solar cells increased from 20 mA/cm^2 to 26 mA/cm^2. This method is promising in eventual device application through controlling stoichiometry and QDs surface morphology.

In chapter 3, facile interfacial sulfur functionalization between $MAPbI_3$ perovskite and SnO_2 ETL was demonstrated. Sulfur atoms at the interface can passivate perovskite surface, contributing to efficient charge transfer and decreased trap densities. The perovskite solar cells prepared using the modified SnO_2 showed improved efficiency significantly with suppressed hysteresis behavior. Considerable retardation of solar cell degradation was achieved by the interfacial sulfur functionalization, retaining almost 90% of its initial efficiency after 70d storage. We believe that facile sulfur functionalization at the interface provides an opportunity for

improving efficiency, stability of perovskite materials.

In chapter 4, squaraine molecules were synthesized to passivate perovskite grain boundaries, which can simultaneously passivate the under-coordinated Pb^{2+} and Pb-I antisite defects. Trap densities were reduced considerably due to the interaction between squaraine and perovskite structure along grain boundaries. Significant performance enhancement of perovskite devices and retardation of devices degradation were achieved although devices were prepared and stored at humid air with 65% RH.

In chapter 5, Cesium Xanthate was applied to realize the sulfur doped in $CsPbIBr_2$ all-inorganic perovskite at relatively low temperature. Phase stability of all-inorganic perovskite was enhanced significantly upon sulfur doping due to its strong interaction between sulfur and perovskite host lattice. The much enhanced performance of all-inorganic perovskite devices was achieved with effectively suppressed phase segregation. This work provides an effective way to prepare superior stable and efficient inorganic halide perovskite devices.

In summary, Pb-based photovoltaic materials exhibit excellent optoelectronic properties in application of solar cells. In the future we have to focus on the development of high quality PbS QDs or Pb-halide perovskite light absorbing layer during the commercialization including the architectures, encapsulation and recycling. Besides, we need to further improve the perovskite devices stability against oxygen and moisture in order to save costs of devices fabrication. Therefore, Understanding the degradation mechanism of light absorbing materials and external encapsulation technologies should realize a longer operation lifetime. Furthermore, we should continue to develop the higher power conversion efficiency with reproducible materials, making these Pb-based QDs and perovskite devices more economically viable.

Achievements

Publications

1. Zhen Wang, Ajay K. Baranwal , Muhammad Akmal Kamarudin, Ng Chi Huey, Manish Pandey, Tingli Ma, Shuzi Hayase*. Xanthate-induced sulfur doped all-inorganic perovskite with superior phase stability and enhanced performance. **Nano Energy**. 2019.

2. Zhen Wang, Muhammad Akmal Kamarudin, Ng Chi Huey, Fu Yang, Manish Pandey, Gaurav Kapil, Tingli Ma, Shuzi Hayase*. Interfacial sulfur functionalization anchoring SnO_2 and $CH_3NH_3PbI_3$ for enhanced stability and trap passivation in perovskite solar cells. **ChemSusChem**.2018.

3. Zhen Wang, Muhammad Akmal Kamarudin, Ng Chi Huey, Fu Yang, Manish Pandey, Gaurav Kapil, Tingli Ma, Shuzi Hayase*. Passivation of grain boundary by squaraine for defect passivation and efficient perovskite solar cells. **ACS Applied Materials & Interfaces**. 2019.

4. Zhen Wang , Muhammad Akmal Kamarudin, Gaurav Kapil, Atul Tripathi, Qing Shen, Kenji Yoshino , Sham S. Pandey, Shuzi Hayase*. Enhancement of charge transport in quantum dots solar cells by N-butylamine-assisted sulfur-crosslinking of PbS quantum dots. **Solar Energy**. 2018.

Conferences

1. Zhen Wang, Muhammad Akmal Kamarudin. N-Butylamine surface treatment to decompose ligands and 2D self-assembled controlled connected-nanocrystals arrays. **Conference.** Japan Society of Applied Physics (JSAP).The 79^{th} spring meeting (Tokyo).2018.

2. Zhen Wang, Ajay K. Baranwal. The role of sulfur on the performance and stability of perovskite devices. **Conference.** Asia-Pacific International Conference on Perovskite, Organic Photovoltaics and Optoelectronics (Kyoto).2019.

Acknowledgements

First, I am very grateful for my supervisor, Prof. Shuzi Hayase to continuous support of my PhD study. I am deeply indebted to Prof.Hayase who provide me his extensive professional guidance and valuable comments in my scientific research work.

Besides my superior, I would like to express my sincere gratitude to Prof. Tingli Ma and Dr. Sham S. Pandey for their warm encouragement and insightful comments during my 3 years research.

Third, I would like to thank all the members in our lab including Mr. Zhang, Mr. Yang, Dr. Akmal, Dr. Ajay, Dr. Chi, Dr. Kapil and Dr.Manish *et al*. they gave me support and help me to do some experiments and analysis of my research. I am also grateful to the Kyushu Institute of Technology and its International student office section.

Finally, I appreciate for my family to support and encouragement my PhD study in Japan, which inspires me to do research work and a better life in the future.